JLU
NEUE WEGE. SEIT 1607.

JUSTUS-LIEBIG-
UNIVERSITÄT
GIESSEN

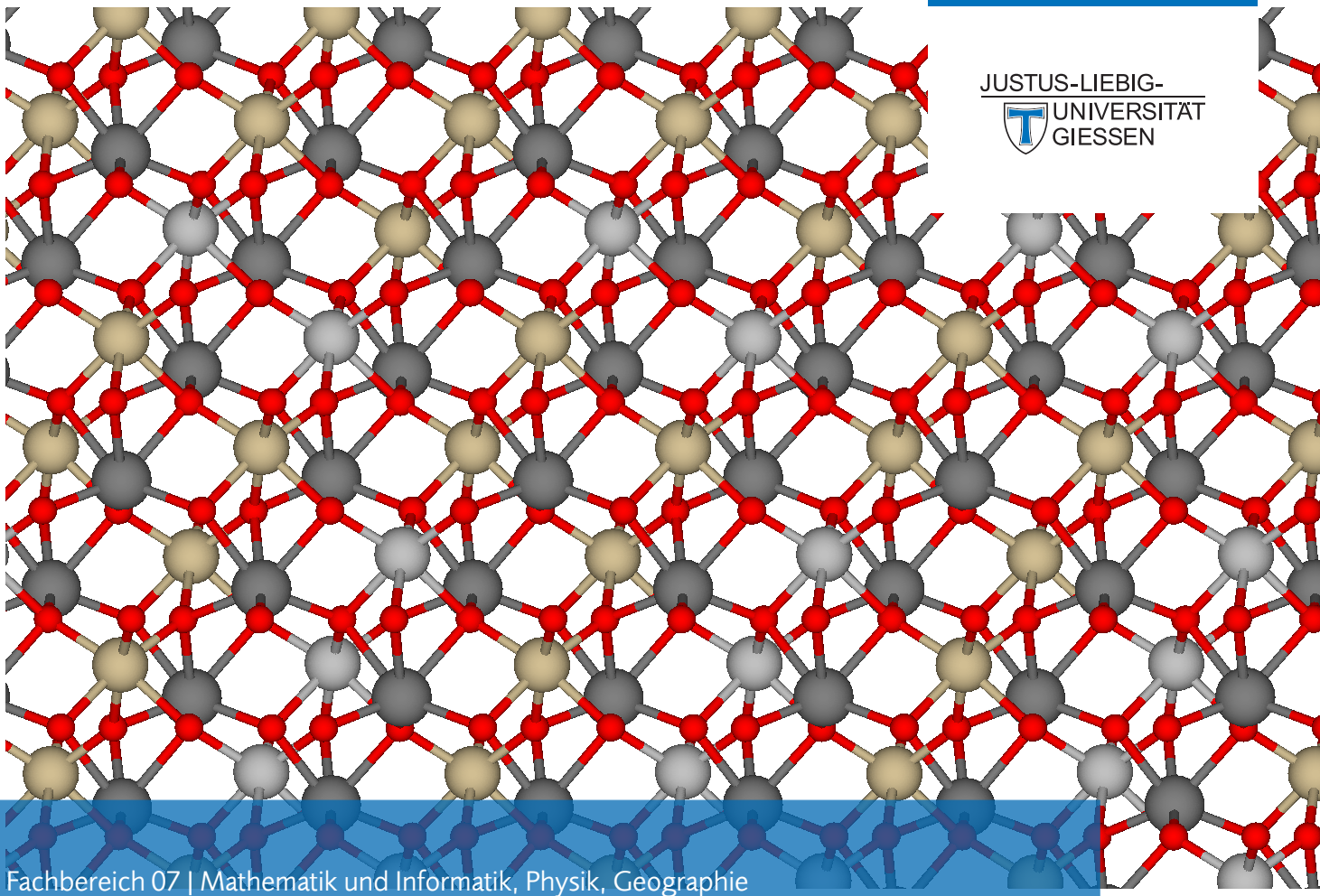

Fachbereich 07 | Mathematik und Informatik, Physik, Geographie
Insitut für theoretische Physik und Zentrum für Materialforschung

Composition and Temperature Dependent Properties of the Lithium Niobate Tantalate Crystal Family

Felix Bernhardt

ITP
Theoretical Physics

ZfM

FOR5044

JUSTUS-LIEBIG-
UNIVERSITÄT
GIESSEN

Institut für Theoretische Physik
Heinrich-Buff-Ring 16
35392 Gießen

Zusammensetzungs- und Temperaturabhängige Eigenschaften von Lithiumniobat-Tantalat Mischkristallen

Composition and Temperature Dependent Properties of the Lithium Niobate Tantalate Crystal Family

Dissertation

zur Erlangung des akademischen Grades
Doktor der Naturwissenschaften (Dr. rer. nat)

vorgelegt dem
Fachbereich 07
der
Justus-Liebig Universität Gießen

verfasst von *Felix Bernhardt*

Gießen im Dezember 2025

Gießen, den 5. März 2026
Dem Fachbereich 07 der Justus-Liebig-Universität Gießen als Dissertation vorgelegt.

Eingereicht am: 04.12.2025
Tag der Disputation: 25.02.2026

Promotionskommission

Vorsitzender: Prof. Dr. Andrè Schirmmeisen
Erstgutachter: Prof. Dr. Simone Sanna
Zweitgutachter: Prof. Dr. Holger Fritze
Prüfer: Prof. Dr. Peter J. Klar

Abstract

Ferroelectrics garner a lot of attention due to their inherent properties which allow for widespread usage, ranging from memory devices (utilizing ferroelectricity itself), over actuators and frequency filters (utilizing piezoelectricity), to sensors or potential energy harvesting applications (utilizing either piezo- or pyroelectricity or photoelectrical properties). In contemporary society, ferroelectrics are crucial for telecommunication technology and within ever-downscaled consumer electronics. Among ferroelectrics, lithium niobate ($LiNbO_3$) (LN) and its isomorphic counterpart lithium tantalate ($LiTaO_3$) (LT) feature a prominent role due to their large piezo- and pyroelectric coefficients, as well as their high photoelasticity and non-linear optical properties. Crucially, both materials exhibit a Curie temperature amongst the highest for all known ferroelectrics, motivating their usage at harsh temperature environments. By combining both materials to lithium niobate tantalate ($LiNb_{1-x}Ta_xO_3$) (LNT) solid solutions, their properties can be fine-tuned, allowing for a wider range of applications of the LN-LT material family.

In this work, LN, LT, and LNT are investigated using an ab initio theoretical framework based on density functional theory (DFT).

The thermal properties of LN and LT are simulated by first determining the thermal expansion coefficients within the quasi-harmonic approximation (QHA) for phonons. The ferro- to paraelectric transition is examined by employing a fully anharmonic phononic approach within the stochastic self-consistent harmonic approximation (SSCHA). Further temperature-dependent material properties, such as the elastic- and piezoelectric constants, are determined by a specifically trained machine-learned force field, which is based on DFT training data.

The LNT solid solutions are modeled using special quasi-random structures (SQS). Their structural, electronical, optical, and thermal properties are computed within DFT and compared with respect to their niobium (Nb)/tantalum (Ta) composition. For most of the extracted properties, deviations from Vegard's law can be observed. Raman and IR spectra are simulated and interpreted with respect to the selection rules of the end compounds LN and LT.

All results are carefully and extensively compared to measurements from experimental groups within the FOR5044 research unit, and the models used throughout this work are critically discussed.

Zusammenfassung

Ferroelektrika erregen großes Interesse wegen ihrer physikalischen Eigenschaften, welche ein breites Anwendungsspektrum finden: Von digitalen Speicher (unter Ausnutzung der Ferroelektrizität), über Aktuatoren oder Frequenzfilter (unter Ausnutzung der Piezoelektrizität), bis hin zu Sensoren oder Energy Harvesting Anwendungen (unter Ausnutzung von Piezo- oder Pyroelektrizität, oder Photoelektrischen Effekten). In der modernen Gesellschaft spielen Ferroelektrika eine entscheidende Rolle in Telekomunikationstechnologien oder in immer-kleiner werdender Haushaltselektronik. Unter den Ferroelektrika nehmen Lithiumniobat (LN) und sein isomorphes Gegenstück Lithiumtantalat (LT) einen besondere Platz wegen ihrer großen piezo- und pyroelektrischen Koeffizienten, sowie ihrer hohen Photoelastizität und nicht-linearen optischen Eigenschaften ein. Vor allem ihre im Vergleich zu anderen Ferroelektrika hohe Curie Temperatur motiviert zu Anwendungsgebieten unter erschwerten Temperaturbedingungen. Unter Kombination der beiden Materialen zu Lithiumniobat-Tantalat Mischkristallen (LNT) können die Materialeigenschaften optimiert werden, um weitere Anwendungsgebiete zu erschließen.

In dieser Arbeit werden LN, LT und LNT innerhalb der ab initio Dichtefunktionaltheorie (DFT) untersucht.

Die thermischen Eigenschaften von LN und LT werden simuliert, indem zuerst die thermale Ausdehnung innerhalb der quasi-harmonischen Näherung (QHA) für Phononen bestimmt wird. Der ferroelektrische Phasenübergang wird über die anharmonische Näherung für Phononen innerhalb der stochastischen, selbstkonsistenten harmonischen Näherung (SSCHA) betrachtet. Weitere temperaturabhängige Materialeigenschaften wie beispielsweise die elastischen- oder piezoelektrischen Koeffizienten werden über ein eigens trainiertes, machine-learned Force-Field bestimmt, welches auf DFT Daten beruht und eine exzellente Leistung zeigt.

Die LNT Mischkristalle werden über zuvor generierte special quasi-random structures modelliert. Ihre strukturellen-, elektronischen-, optischen-, und thermischen Eigenschaften werden im Rahmen der DFT berechnet, und im Bezug auf ihre Nb/Ta Zusammensetzung verglichen. Für die meisten Eigenschaften ergibt sich eine Abweichung vom Vegard Verhalten. Raman- und Infrarotspektren werden simuliert und hinsichtlich der Auswahlregeln der Endkomponenten LN und LT diskutiert.

Alle Ergebnisse werden ausführlich und sorgfältig mit experimentellen Daten aus der FOR5044 Forschungsgruppe verglichen, und die während dieser Arbeit verwendenten Modelle werden kritisch evaluiert.

Contents

Acronyms

DFT density functional theory

DFPT density functional perturbation theory

DOS density of states

GGA generalized-gradient approximation

GWA GW approximation

IPA independent particle approximation

IR infrared

Li lithium

LN lithium niobate ($LiNbO_3$)

LNT lithium niobate tantalate ($LiNb_{1-x}Ta_xO_3$)

LO longitudinal-optical

LST Lyddane-Sachs-Teller relation

LT lithium tantalate ($LiTaO_3$)

Nb niobium

O oxygen

QHA quasi-harmonic approximation

SQS special quasi-random structures

SSCHA stochastic self-consistent harmonic approximation

Ta tantalum

TO transversal-optical

VASP Vienna Ab Initio Simulation Package

List of Figures

List of Tables

1 Introduction

1.1 Objective

Modern technology increasingly relies upon advanced and high-performing materials. Especially the need for small-scale, resilient, and energy efficient devices drives scientific focus towards the development and improvement of highly functional materials. The class of ferroelectrics is of particular interest, for they cover a wide range of peculiar and useful properties. Ferroelectricity is named analogously to ferromagnetism: Whereas materials exhibiting ferromagnetism feature a permanent magnetic moment, ferroelectrics instead feature a permanent electric dipole moment, resulting in a permanent polarization (the so called spontaneous polarization[1]). The direction of this spontaneous polarization may be flipped by applying a counteracting electric field of sufficient strength. Despite the rather late discovery of this material class in 1920 by Valasek [2], ferroelectrics have been extensively studied and utilized over the last decades: Ferroelectric capacitors are used as data storage, e.g. in random-access memory, since their spontaneous polarization direction (corresponding to one binary state) can be switched by application of an external electric field [3, W3]. Periodically poled transducers could serve as high-frequency filters, as an alternative to commonly used surface- or bulk acoustic wave resonators [4]. Further usage of ferroelectrics is enabled not only by their eponymous property, but instead relies upon their multitude of different inherent effects:

All ferroelectric materials also show piezoelectric behavior: If a stress is applied to a piezoelectric material, charges are shifted within the crystal. Thus, a mechanical input can be converted to an electrical output. Similarily, all piezoelectric materials also exhibit the reverse effect, the so-called inverse piezoelectric effect, which enables to convert electrical signals to mechanical ones. Indeed, most piezoelectrics used in applications today are also ferroelectric [5, 6]. Historically, the piezoelectric effect was first utilized for acoustic applications, such as sonar, or the recording or playback of sound. Today, the need for nano-scale speakers and microphones is even more prominent in modern consumer devices, such as smartphones. Other applications include piezoelectric actuators: Here, the relatively small deformations occuring in a piezoelectric material due to an applied electrical field (or vice versa) allow for very accurate motions. Many high-precision instruments, such as the atomic force or scanning tunneling microscopes, rely on piezoelectric actuators [W5, W6].

All ferroelectric materials are also pyroelectric: This class of materials generates an electric voltage upon heating or cooling. An obvious use case for such materials are

[1] Strictly speaking, this non-zero polarization at vanishing electric fields should be called *remnant polarization*, in analogon to the hysteresis of magnetic materials. However, the remnant- and spontaneous polarization for ferroelectrics are almost identical, and the term spontaneous polarization has asserted itself in literature.

thermal sensors. Pyroelectricity will, however, not be focused in this work.
The applications for ferroelectrics mentioned above cover a wide range of different operating temperatures. Whereas scanning tunneling microscopes are often utilized in a near-zero Kelvin environment, many sensoring applications are employed at several hundred Kelvin higher temperatures. Further, almost all of these applications require explicit knowledge of the crystal properties at their respective operating temperatures, such as e.g. the strength of the piezoelectric effect. Since almost all material properties depend either directly on temperature, or indirectly via e.g. thermally induced stresses, the knowledge of temperature-dependent behavior of ferroelectrics is of utmost importance.
Even more prominently, all ferroelectrics undergo a phase transition towards a paraelectric phase at elevated temperatures. This paraelectric phase features an inversion center in its underlying crystal structure, and the material thus loses all pyro- and ferroelectric properties[2], potentially rendering the underlying device useless. Depending on the material, this ferroelectric phase transition does not occur instantaneously, but instead the spontaneous polarization continuously vanishes with an increase in temperature. Hence, a ferroelectric may behave different if operated near its transition temperature compared to low-temperature environments.
One of the most prominent ferroelectrics in use today is lithium niobate ($LiNbO_3$) (LN): Featuring unusually large piezoelectric, pyroelectric, photoelastic, and nonlinear optical properties [7] enables the usage of LN for a wide range of applications: The electro-optic effect of LN is prominently used in electro-optic modulators [W4, W7], which are commonly used to convert electric signals to optical ones. The piezoelectric properties of LN are for example used in surface acoustic wave devices, such as in high-frequency filters, which are needed for 5G, or even emerging potential 6G networks [8, 9]. In recent years, thin-film LN has become commercially available on a wafer scale, renewing the interest to use LN as a platform for integrated photonic circuits, analogously to silicon wafers for electronic circuits [10–12]. A comprehensive and more detailed overview of the various applications of LN is given in Ref. [13]. Notably, the Curie temperature (i.e. the temperature at which the transition from the ferro- to the paraelectric phase occurs) of LN of about 1400 K [14] is significantly higher than for most other ferroelectrics [15], motivating its application in extreme temperature regimes.
Despite these outstanding characteristics, LN is impractical to utilize at higher temperatures, since it tends to decompose [16]. The to LN isomorphic compound lithium tantalate ($LiTaO_3$) (LT) features instead a better thermal stability, but still cannot be utilized in high-temperature environments due to its much lower Curie temperature of around 874 K [17]. Even though LN and LT are chemically similar, some of their physical properties are not, which is best observed by the negative birefringence of LN compared to a positive one in LT [W17].
Since the 1970s, the application of lithium niobate tantalate ($LiNb_{1-x}Ta_xO_3$) (LNT) mixed crystals has been proposed to merge beneficial properties of the two materials [18]. These LNT alloys can be synthesized over the whole compositional range

[2] The material can also lose its piezoelectricity at its paraelectric phase [6].

between LN and LT [19], as the lattice parameters of both materials, as well as the atomic radii of (pentavalent) Nb and Ta are almost equivalent [W18]. By fine-tuning the composition within a mixed crystal, new or enhanced properties may be discovered which might enable usage in a wider range of applications. Despite the promising concept, research on the LNT mixed crystals remained sparse for decades.
In 2020, the dedicated research unit FOR5044 [W19] was founded to study LN, LT, and LNT solid solutions. One of its main focuses lies in the determination of high-temperature properties, including charge transport mechanisms, acoustic losses, and the ferroelectric to paraelectric phase transition dynamics. Further research includes the synthetization of high-quality crystals, their spectroscopic signatures, and their domain (wall) properties. The measurements performed within the research unit are complemented by numerical models, which aim to provide validation and explanation for the observed phenomena.
This numerical modeling is carried out ab initio, i.e. without empirical parameters, and only fundamental concepts of physics are employed. These concepts cover a wide range of modern physics, extending from mechanics to (semi-)classical electro- and thermodynamics, while also utilizing modern quantum mechanics and computational physics. The baseline for all calculations can be found in the quantum-mechanical description of the underlying electron ion many-body problem within density functional theory (DFT) [20, 21]. The parameter-free description in DFT enables an independent comparison to the experiments, which is crucial for scientific validation. Further, DFT provides accurate ground state properties, such as e.g. lattice constants, bonding lengths, formation energies, etc., with a moderate numerical cost. Note that depending on system size and required accuracy, such calculations still need to run on high-end computers. In addition, the DFT results can be post-processed to extract e.g. optical properties, or expanded to more sophisticated approximations to the many-body problem, such as, e.g., the GW approximation.
Temperature-related effects are incorporated on an atomistic scale: Within statistical physics, temperature itself is defined as the average energy of the ions within the material. Hence, rather than the electronic states[3], the ionic properties of the crystal must be calculated. Through the Hellman-Feynman theorem, DFT also provides access to the forces acting on the ions, and thus to the temperature-dependent properties of materials. The ionic motions are separated into their eigenmodes, the quantized quasiparticles called phonons, which are then activated according to the Bose-Einstein statistics to assess their impact at a fixed temperature. The calculation of ionic oscillations bears an additional numerical cost on top of the DFT calculations, making the simulation of temperature-related effects one of the computationally most demanding tasks in modern material physics. With the emergence of machine-learned force fields, these numerical costs could be drastically reduced, while still maintaining the ab initio character and the high accuracy of the forces trained upon DFT data. Since the underlying training algorithms only recently became publicly available, the quality and reproducibility of results is virtually unexplored. The numerical speedup

[3] If the electronic band gap is large compared to $k_B T$, the electronic contributions to thermal effects can be neglected. For metals, the electronic properties have a larger influence on the thermodynamics of the system.

of a factor of around 10^3 compared to pure DFT calculations enables the investigation of systems and properties that were previously unfeasible to model.
Another hurdle lies in the modeling of the LNT mixed crystals: The niobium (Nb) and tantalum (Ta) ions are assumed to be randomly distributed throughout the whole crystal. However, a truly random structure cannot be simulated, since all underlying DFT calculations implicitly apply periodic boundary conditions[4]. Hence, additional approximations have to be made in order to accurately describe a random alloy. Here, special quasi-random structures (SQS) are employed, which have been proven to reliably reproduce properties, and especially local site effects, within random alloys [22–24].
This work aims to tackle two distinct topics, namely the temperature- and composition dependence of different ground- and excited state material properties. Within the first topic, the temperature-dependence on the material properties such as the lattice-, elastic-, and piezoelectric constants of LN and LT is investigated. These data can be utilized to design, optimize, or enhance devices for usecases under extreme temperature conditions. Within the second topic, the LNT solid solutions are investigated with respect to their composition-dependent ground-state properties, such as the lattice constants and electronic band gaps, which provides the basis for all future research on the mixed crystals. Also, the Raman and infrared (IR) spectra as a function of the Nb/Ta composition are calculated, which provide a way to determine the Nb/Ta-ratio within a given LNT sample non-destructively within experiments, which again provides the ground work for further investigations.

1.2 The Structure of this Work

This work is separated into three chapters, that consecutively build on each other: First, the methodology is outlined in Sec. 2, providing the basis for the following calculations and results. Second, LN and LT are examined with respect to their different behaviors under temperature changes, including the thermal expansion (Secs. 3.2 and 3.5.1), Curie temperature (Sec. 3.3), and elastic properties (Sec.3.5.2). The latter calculations are carried out by training and applying machine-learned force fields. A closer look at the electronic properties and optical response of congruent LN in chapter 3.6 yields additional insights concerning the effects of lithium (Li) diffusion at elevated temperatures. Lastly, the LNT solid solutions are investigated, focussing on their structural (Sec.4.2), electronic (Sec.4.4), and optical (Sec.4.5) properties over the whole compositional range between LN and LT. The in Sec. 4.6 provided Raman and IR spectra are used to fingerprint the underlying composition, while also yielding phononic properties of the alloy system.
Previously authored or co-authored results that have already been published are indexed with a leading "P" in the citation labeling. The author's full publication list is provided in section C.2.

[4] The usage of periodic boundary conditions results from the plane wave ansatz applied throughout this work, and is in principle not inherent to DFT.

2 Methods

The concept that all matter consists of impartible particles was first proposed in ancient Greek [25]. At these times this idea was, however, motivated by philosophical considerations, and not a scientific concept. The first experimentally motivated atomistic theory was developed by Dalton at the beginning of the 19th century [W1]. Since the early 20th century it is assumed that these atoms posess an inner structure, consisting of ions surrounded by electrons. The ions are small compared to the atomic radius, and carry the same electric charge as all its surrounding electrons combined. This idea was first proposed by Rutherford in 1911 [26], and later refined by Bohr in 1913 [27]. Within a solid, the atoms bond together as their electronic charge densities overlap. With the emergence of quantum mechanics, these models were superseded by fully mathematical, abstract descriptions. Still, Bohr's model serves as a first step to formulate and interpret the quantum mechanical results.

2.1 Many-Body Hamiltonian

In order to quantum-mechanically describe the electron-ion system, the solution (wavefunction) to Schrödinger's equation needs to be calculated. Its corresponding Hamiltonian in Hartree units reads as:

$$\begin{aligned}\frac{\hat{H}}{E_h} = &\sum_{k=1}^{N_k}\left(-\frac{m}{2M_k}\nabla^2_{\tilde{\mathbf{R}}_k}\right) + \sum_{i=1}^{N_e}\left(-\frac{1}{2}\nabla^2_{\tilde{\mathbf{r}}_i}\right) \\ &+ \sum_{\substack{k,l=1\\k<l}}^{N_k}\frac{Z_l Z_k}{|\tilde{\mathbf{R}}_k - \tilde{\mathbf{R}}_l|} + \sum_{\substack{i,j=1\\i<j}}^{N_e}\frac{1}{|\tilde{\mathbf{r}}_i - \tilde{\mathbf{r}}_j|} - \sum_{k=1}^{N_k}\sum_{i=1}^{N_e}\frac{Z_k}{|\tilde{\mathbf{R}}_k - \tilde{\mathbf{r}}_i|}.\end{aligned} \tag{2.1}$$

The first and second summand formally denote the kinetic energies of the ions and electrons, respectively, whereas the other terms describe the Coulomb interaction between the ions, the electrons, and between the electrons and ions, in order of appereance. Here, the many-body system includes N_k ions and N_e electrons, at with the Bohr-radius a_0 scaled positions $\tilde{\mathbf{R}} = \frac{\mathbf{R}}{a_0}$ and $\tilde{\mathbf{r}} = \frac{\mathbf{r}}{a_0}$, respectively. M_k denotes the mass of the k-th ion, and Z_k its electric charge in units of the electronic charge e. The mass of an electron is labeled as m. The Hartree energy E_h is given as

$$E_h = \frac{me^4}{16\pi^2\varepsilon_0^2\hbar^2}, \tag{2.2}$$

with the vacuum permittivity ε_0 and the reduced Planck constant $\hbar$.
Already for moderate quantities of a given material (e.g. one mole, i.e. $\sim 10^{23}$ particles), the eigenfunctions (wavefunctions) of this Hamilton operator are unattainable,

due to the large number of particles involved. Thus, a number of approximations are needed to simplify the description of this many-particle system.

2.1.1 Born-Oppenheimer Approximation

The many-body wavefunction Ψ can be decompositioned into an electronic part ϕ, and an ionic part χ:

$$\Psi(\mathbf{R}, \mathbf{r}) = \chi(\mathbf{R}) \cdot \phi(\mathbf{R}, \mathbf{r}). \tag{2.3}$$

Using this Ansatz, Eq.(2.1) can be written as two separate equations for the electrons and ions:

$$\begin{aligned} \hat{H}_e \phi_a(\mathbf{R}, \mathbf{r}) &= \epsilon_a(\mathbf{R}) \phi_a(\mathbf{R}, \mathbf{r}) \\ \left(\hat{T}_K + \epsilon_\beta(\mathbf{R})_e\right) \chi_\beta(\mathbf{R}) + \sum_a A_{\beta a}(\mathbf{R}) \chi_a(\mathbf{R}) &= E \chi_\beta(\mathbf{R}). \end{aligned} \tag{2.4}$$

The system of equations (2.4) is equivalent to Eq.(2.1): $\hat{H}_e$ describes the electrons in a static background potential, given by the ions at their respective positions $\mathbf{R}$, whereas the second equation describes the full electron ion system, where the terms $\hat{T}_k$ and $A_{\beta a}$ are the kinetic energy of the ions, and the electron-ion coupling coefficients, respectively. Since the kinetic energy of the ions, i.e. the first summand of Eq.(2.1), is much smaller compared to the kinetic energy of the electrons, i.e. the second summand of Eq.(2.1), the electronic and ionic systems can be solved seperately in good approximation by neglecting the coupling coefficients $A_{\beta a}$. This approach is called adiabatic-, or Born-Oppenheimer approximation. In practice, only the electronic system is treated fully quantum-mechanically, and instead, the ionic system is commonly solved using classical mechanics.

2.1.2 Bloch's Theorem

Depending on how the ions are spatially aligned within a given solid, one can distinguish between three different types of arrangements:

- In **crystalline solids**, the ions are ordered throughout the whole crystal, i.e. the solid posesses long-range order and translational symmetry.
- **Aperiodic crystals** exhibit no periodic ordering of atoms, but still possess long-range order.
- If the ions are only ordered within a certain spatial region of the solid, i.e. exhibit only short-range order, one refers to a **polycrystalline solid**.
- **Amorphous solids** are defined by possesing neither long-, nor short-range order.

Only periodic, crystalline solids will be discussed in this work[5]. For periodic crystals, it suffices to limit their mathematical description to the smallest possible unit of repitition, the primitive unit cell. Surface effects are completely neglected in this approach, and periodic boundary conditions are assumed instead. This unit cell is spanned by three lattice vectors. The corresponding unit cell in reciprocal space is called first Brillouin zone. Equation (2.4) can then be further simplified by exploiting the periodicity of the ionic potential, leading to the Bloch-Ansatz for the electronic wave function ϕ:

$$\phi_{\mathbf{k}}(\mathbf{r}) = e^{i\mathbf{k}\mathbf{r}} \frac{1}{\sqrt{V_0}} \underbrace{\sum_{\mathbf{G}} c(\mathbf{k}+\mathbf{G}) e^{i\mathbf{G}\mathbf{r}}}_{=u_{\mathbf{k}}(\mathbf{r})}. \tag{2.5}$$

Here, $\mathbf{k}$ denotes a reciprocal vector, V_0 the volume of the unit cell in real space, and $u_{\mathbf{k}}(\mathbf{r})$ the periodic part of the Bloch function. The function $c(\mathbf{k})$ holds the periodicity with respect to a reciprocal lattice vector $\mathbf{G}$, such that

$$c(\mathbf{k}+\mathbf{G}) = e^{i(\mathbf{k}+\mathbf{G})\cdot\mathbf{R}} = e^{i\mathbf{k}\cdot\mathbf{R}} e^{i\mathbf{G}\cdot\mathbf{R}} = e^{i\mathbf{k}\cdot\mathbf{R}} \underbrace{e^{i2\pi l}}_{=1} = c(\mathbf{k}), \quad l \in \mathbb{N}, \tag{2.6}$$

with a lattice vector $\mathbf{R}$. Hence, the reciprocal vector $\mathbf{k}$ is limited to the first Brillouin zone[6]. In the thermodynamic limit, i.e. an infinite number of repeated unit cells, the $\mathbf{k}$-vectors form a continuous spectrum, leading to a band-like behaviour of the electronic energies.
In practice, the infinite sum in Eq.(2.5) is truncated for large $\mathbf{G}$-vectors by defining a cutoff energy

$$\frac{1}{2} |\mathbf{k}+\mathbf{G}|^2 < E_{\text{cut}}. \tag{2.7}$$

2.2 Density Functional Theory

Even with these drastic simplifications of Eq. (2.1), handling the electronic wave function of a single unit cell is numerically challenging. The idea of the DFT is to instead express the electronic Hamiltonian as a functional of the electronic density: The Hohenberg-Kohn theorems state that the mapping between a potential and its corresponding electronic ground state density is bijective. The many-body Hamiltonian of the electrons (2.4) can thus be expressed as a functional of the electronic ground

[5] This ansatz only holds as a first approximation for solid solutions, which will be discussed in detail in Sec. 4.1

[6] According to Noether's Theorem, translational invariance implies momentum conservation. Here, the ionic potential is invariant under discrete translations. Therefore, only the quasi-momentum $\mathbf{k}$ is conserved (i.e. the momentum modulo a $\mathbf{k}$ within the first Brillouin zone)

state density $n(\mathbf{r})$:

$$\begin{aligned} E[n] = E[\{\phi_a\}] &= E_{\text{kin}} + E_{\text{k-e}} + E_{\text{e-e}_{\text{stat.}}} + E_{\text{XC}} \\ &= \sum_{a=1}^{N_e} \int \frac{-\hbar^2}{2m} \phi_{ka}^*(\mathbf{r}) \nabla_{\mathbf{r}}^2 \phi_{ka}(\mathbf{r}) \mathrm{d}\mathbf{r} + \int n(\mathbf{r}) V(\mathbf{r}) \mathrm{d}\mathbf{r} \\ &\quad + \frac{1}{2} \int \int \frac{e^2 n(\mathbf{r}) n(\mathbf{r}')}{4\pi\epsilon_0 |\mathbf{r} - \mathbf{r}'|} \mathrm{d}\mathbf{r}\mathrm{d}\mathbf{r}' + E_{\text{XC}}[n(\mathbf{r})]. \end{aligned} \tag{2.8}$$

Here, the ionic background potential is labeled as V. The term E_{XC} is called exchange-correlation energy, and incorporates all many body effects that are not explicitly captured by the pure Coulomb interactions, e.g. terms regarding the Pauli exchange and screened Coulomb interactions. Several approximations of this energy term have been proposed (e.g. Refs. [20, 28, 29]), since its exact form cannot be given analytically [28].
Using Lagrange multipliers to determine the minimum (ground state) energy of $E[n]$ one arrives at the Kohn-Sham equations:

$$\left(-\frac{\hbar^2}{2m} \nabla_{\mathbf{r}}^2 + \underbrace{V(\mathbf{r}) + \int \frac{n(\mathbf{r}') e^2}{4\pi\epsilon_0 |\mathbf{r} - \mathbf{r}'|} \mathrm{d}\mathbf{r}' + \frac{\partial E_{\text{XC}}[n]}{\partial n}}_{:= V_{\text{eff}}} - \epsilon_a \right) \phi_a(\mathbf{r}) = 0. \tag{2.9}$$

Formally, the particles described by ϕ_a are not electrons, since they do not interact with each other, but instead move within the effective potential V_{eff}. For most descriptions, however, the Kohn-Sham particles are interpreted as electrons. Still, the electronic charge density is a superposition of all Kohn-Sham wavefunctions:

$$n(\mathbf{r}) = \sum_{a=1}^{N_e} |\phi_a(\mathbf{r})|^2. \tag{2.10}$$

Consequently, the Kohn-Sham equations (2.9) can be solved iteratively: Starting with an arbitrary charge distribution $n(\mathbf{r})$, the Kohn-Sham equations can be set up and solved to obtain the corresponding Kohn-Sham wavefunctions ϕ_a. Using these wavefunctions, a new charge density can be constructed using Eq. (2.10) which is then used to compile and solve the Kohn-Sham equations again. This cycle is stopped when the charge density (or, in most cases, the ground state energy) converges within a given threshold.
Even though the DFT is mathematically only valid for the electronic ground state, excited state properties can technically still be extracted. More sophisticated formulations that explicitly describe excited electronic states are numerically much more demanding, and thus, DFT is often the preferred choice.

2.2.1 Generalized-Gradient Approximation

Since the exchange-correlation energy E_{XC} appearing in eq. (2.9) is not known analytically, approximate desciptions need to be formulated. Within the generalized-gradient approximation (GGA), E_{XC} is not only a functional of the electronic ground

state density $n(\mathbf{r})$, but also of its spatial changes $\nabla n(\mathbf{r})$. In the formulation proposed by Perdew, Burke, and Ernzerhof [28], the exchange-correlation energy is explicitly evaluated as a separate exchange term E_X, and a correlation term E_C:

$$E_\mathsf{XC} = E_\mathsf{X} + E_\mathsf{C}, \tag{2.11}$$

$$E_\mathsf{X} = \int n(\mathbf{r})\epsilon_\mathsf{X}[n(\mathbf{r})]F_\mathsf{X}(s)\mathrm{d}\mathbf{r}, \quad F_\mathsf{X}(s) = 1 + k - \frac{k}{1+\frac{\mu s^2}{k}}, \tag{2.12}$$

$$E_\mathsf{C} = \int n(\mathbf{r})\left(\epsilon_\mathsf{C}[n(\mathbf{r})] + H_\mathsf{C}(r_s,\eta,t,\beta)\right)\mathrm{d}\mathbf{r}, \quad \mu = \beta\frac{\pi^2}{3}, \quad r_s = \left(\frac{3}{4\pi n}\right)^{\frac{1}{3}}. \tag{2.13}$$

Here, s and t denote the density gradients. The parameters μ and β are determined from boundary conditions. This formulation is named after their authors as PBE (Perdew-Burke-Ernzerhof). Later, the same authors refined these parameters in order to obtain more reliable lattice constants for solids and surfaces[7] [29]. Accordingly, this formulation is known as PBEsol.

2.2.2 DFT+U

Because the correlation energy E_C cannot be known analytically[8], uncertainties in the electronic energies are to be expected. In particular, it has been observed that the DFT tends to delocalize electrons. Hence, the DFT yields especially large errors for strongly correlated systems with localized electrons, which typically have strong d- or f-like characterstics. As a first approximation, the DFT energy can be corrected by adding a Hubbard energy term E_Hub that explicitly takes local interactions into account:

$$E_\mathsf{DFT+U} = E_\mathsf{DFT} + E_\mathsf{Hub} - E_\mathsf{dc}, \tag{2.14}$$

where the term E_dc denotes the energy contribution of local effects, which are already present in E_DFT and therefore must not be accounted for twice. Using the formulations outlined in Ref. [30], this corrected energy reads as

$$E_\mathsf{DFT+U} = E_\mathsf{DFT} + \frac{U}{2}\sum_{I\sigma}\left[\mathrm{tr}(n^{I\sigma}_{mm'}) - \mathrm{tr}([n^{I\sigma}_{mm'}]^2)\right], \tag{2.15}$$

$$n^{I\sigma}_{mm'} = \sum_a^{N_e} f_a^{I\sigma}\,\langle\phi_a^I|Y^\sigma_{lm}\rangle\,\langle Y^\sigma_{lm'}|\phi_a^I\rangle, \tag{2.16}$$

where $n^{I\sigma}_{mm'}$ denotes the density matrix of site σ with spin I and magnetic quantum number indices m, $f_a^{I\sigma}$ the occupation function, and Y^σ_{lm} spherical harmonics centered at site σ. The parameter U sets the overall magnitude of the correction term. In

[7] The functional parameters where optimized in order to reproduce lattice constants near room temperature, but completely neglect phononic effects.

[8] In contrast, the exact exchange energy E_X can formally be calculated using Hartree-Fock theory.

general, different values for U are chosen for different orbital momentum quantum numbers l, which are determined either by linear response theory [31], or simply by fitting the resulting electronic band gap to experimental results.

2.3 Hedin Equations

Another method to calculate the electronic many-body wavefunction of a material fully ab initio is given by the *Hedin equations*. One may start by expressing the (strongly) interacting particles by weakly-interacting quasi-particles. The connection between these quasi-particles and the real particles is given by the self-energy Σ, and its Schrödinger's equation reads as:

$$\left[-\frac{1}{2}\nabla^2 + V_{\text{ext}}(\mathbf{r}) + V_{\text{H}}(\mathbf{r})\right]\phi_a(\mathbf{r},\omega) + \int \Sigma(\mathbf{r},\mathbf{r}',\omega)\phi_a(\mathbf{r}',\omega)\mathrm{d}\mathbf{r}' = E_a(\omega)\phi_a(\mathbf{r},\omega). \tag{2.17}$$

The self-energy contains all many-body effects, mapping the single particle states ϕ_a onto the many-body wavefunction. Formally, the exchange-correlation functional serves a similar purpose within DFT, and by setting

$$\Sigma(\mathbf{r},\mathbf{r}',\omega) = V_{\text{XC}}[n(\mathbf{r})]\delta(\mathbf{r}-\mathbf{r}'), \tag{2.18}$$

one obtains the already established Kohn-Sham equations (2.9), i.e. the local, static exchange correlation energy is replaced by the non-local self-energy. Moreover, in contrast to DFT, equation (2.17) is not limited to the ground state. Thus, Eq. (2.17) can be utilized to more accurately describe excited state properties.

The abovementioned Schrödinger's equation can also be expressed via a single-particle Green's function G:

$$\left[i\frac{\partial}{\partial t_1} + \frac{1}{2}\nabla^2_{\mathbf{r}_1} - V_{\text{ext}}(\mathbf{1}) - V_{\text{H}}(\mathbf{1})\right]G(\mathbf{1},\mathbf{2}) + i\int \Sigma(\mathbf{1},\mathbf{3})G(\mathbf{3},\mathbf{2})\mathrm{d}\mathbf{3} = \delta(\mathbf{1},\mathbf{2}). \tag{2.19}$$

The shorthand notation of $\mathbf{i} = (\mathbf{r}_i, t_i)$ enables to write different space-time coordinates as a single integer. The propagator G describes the propagation probability of an electron from **2** to **1** (if $t_1 > t_2$), or of a hole (i.e an unoccupied valence band state, if $t_1 < t_2$). Note, that here the full time-dependent Schrödinger equation is assumed, in contrast to (2.17). The single-particle propagator is given as

$$G(\mathbf{1},\mathbf{2}) = -i\left\langle N\right|\mathcal{T}\left[\Phi(\mathbf{1})\Phi^\dagger(\mathbf{2})\right]\left|N\right\rangle, \tag{2.20}$$

where $\mathcal{T}$ denotes the time-ordered product of the two field operators Φ.

The self-energy Σ can be calculated self consistently via the Hedin equations:

$$
\begin{aligned}
G(\mathbf{1},\mathbf{2}) &= G_0(\mathbf{1},\mathbf{2}) + \int G_0(\mathbf{1},\mathbf{3})\Sigma(\mathbf{3},\mathbf{4})G(\mathbf{4},\mathbf{2})\mathrm{d}(\mathbf{34}),\\
W(\mathbf{1},\mathbf{2}) &= \nu(\mathbf{1},\mathbf{2}) + \int \nu(\mathbf{1},\mathbf{3})P(\mathbf{3},\mathbf{4})W(\mathbf{4},\mathbf{2})\mathrm{d}(\mathbf{34}),\\
\Sigma(\mathbf{1},\mathbf{2}) &= i\int G(\mathbf{1},\mathbf{3}^+)W(\mathbf{1},\mathbf{4})\Lambda(\mathbf{3},\mathbf{2},\mathbf{4})\mathrm{d}(\mathbf{34}),\\
P(\mathbf{1},\mathbf{2}) &= -i\int G(\mathbf{1},\mathbf{3})\Lambda(\mathbf{3},\mathbf{4},\mathbf{2})G(\mathbf{4},\mathbf{1}^+)\mathrm{d}(\mathbf{34}),\\
\Lambda(\mathbf{1},\mathbf{2},\mathbf{3}) &= \delta(\mathbf{1},\mathbf{2})\delta(\mathbf{1},\mathbf{3}) + \int \frac{\partial\Sigma(\mathbf{1},\mathbf{2})}{\partial G(\mathbf{4},\mathbf{5})}G(\mathbf{4},\mathbf{6})G(\mathbf{7},\mathbf{5})\Lambda(\mathbf{6},\mathbf{7},\mathbf{3})\mathrm{d}(\mathbf{4567}).
\end{aligned}
\tag{2.21}
$$

Here, W, ν, P, and Λ denote the screened Coloumb potential, the bare (unscreened) Coulomb potential, the polarizability, and the vertex function, respectively. The free propagator G_0 can be extracted by setting $\Sigma = 0$ in Eq. (2.19). The superscripted plus-sign indicates an infinitesimal temporal shift, which is needed to assure the convergence of the integrals. These equations are easy to interpret with the help of Feynman diagrams, which are depicted in Fig. 1.

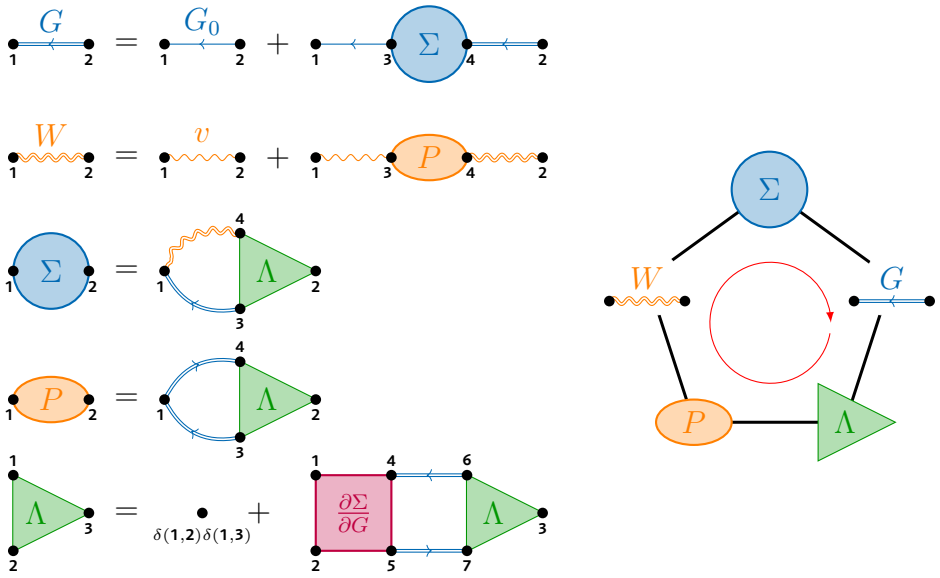

Figure 1: Schematic representation of the Hedin's equation using Feynman diagrams (left), and the self-consistent cycle (right).

The equations can in principle be solved iteratively, however, this would require a huge computational effort. Instead, one assumes the so called GW approximation

(GWA), where the integral in Λ is set to zero. Additionally, one may also include only a single iteration (typically starting with $\Sigma = 0$). This commonly used, non-self consistent ansatz is called G_0W_0. The latter typically benefits by from a cancellation of errors, compared to the fully self-consistent GWA.

2.4 Machine-learned Force Fields

For many practical simulations, the electronic wavefunction or charge density need not be explicitly known. Instead, if only certain physical properties are of importance (i.e. the resulting forces on the ions), one may bypass the numerically challenging many-body calculations by using an analytical, empirical formulation to directly compute the sought-after quantity. These formulations are, in contrast to the previously discussed DFT and GW approximations, not ab initio. Hence, their application to a wide variety of materials is not immediately obvious. Consequently, analytical force fields typically provide less accuracy than the previously described ab initio methods. These weaknesses can be overcome by fitting (training) the analytical model with explicitly calculated data (provided e.g. from DFT calculations).
The within the VASP package [32–34,W11] available description of a machine learned force field will be outlined in this chapter. Here, one assumes that all atoms in a given system (or rather their respective valence electrons) contribute additively to the total electronic ground state energy U, such that

$$U = \sum_k U_k(\mathbf{X}_k), \tag{2.22}$$

where $\mathbf{X}_k$ is multi-dimensional vector describing the local atomic environment of atom k. From a quantum-mechanical point of view, this approximation cannot be justified, since the total electronic energy cannot be separated into local contributions. However, the ansatz provides an easily expandable mathematical description. The local environment of atom k is characterized by the pair correlation function $\rho^{(2)}(r)$ (i.e. how many atoms are within a given distance r of atom k), and the angular correlation function $\rho^{(3)}(r, s, \Theta)$ (i.e how many atoms are within the distances r and s, if the angle between these directions is Θ).
The quantities can be expressed via spherical Bessel functions χ and Legendre-polynomials P:

$$\rho_k^{(2)}(r) = \frac{1}{\sqrt{4\pi}} \sum_n^{n_{\text{max}}^0} c_n^k \chi_{n0}(r), \tag{2.23}$$

$$\rho_k^{(3)}(r, s, \Theta) = \sum_l^{l_{\text{max}}} \sum_n^{n_{\text{max}}} \sum_v^{v_{\text{max}}} \sqrt{\frac{2l+1}{2}} p_{nvl}^k \chi_{nl}(r) \chi_{vl}(s) P_l(\cos(\Theta)). \tag{2.24}$$

The values for $\cdot_{\text{max}}$ serve as numerical cutoffs, determining the accuracy of the correlation functions. Additionally, the atom types must be differentiated in multicomponent systems. The descriptor vector $\mathbf{X}_k$ is then given via the expansion coefficients c^k and

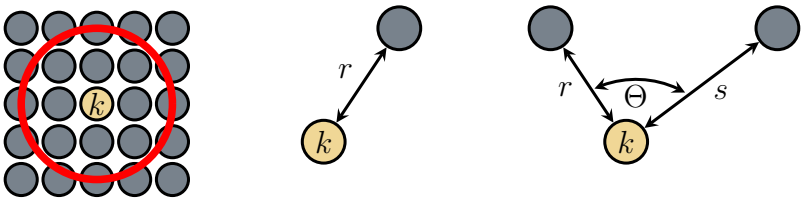

Figure 2: Construction of the atomic environment, The cutoff radius (left) determines up to which distance to reference atom k the correlation functions are determined. The pair correlation function (middle) measures how many neighboring atoms are at a given distance r. The angular correlation function (right) measures how many neighboring atoms lie at a distance s and angle Θ, if another atom is found at a distance r.

p^k:

$$\mathbf{X}_k = (\{c_n^k, p_{nvl}^k\}). \tag{2.25}$$

Since the correlation functions are invariant under rotations and translations, a given atomic structure maps uniquely to a descriptor vector.
Finally, a descriptor needs to be mapped onto its corresponding total electronic energy. Since the relation between these quantities is not explicitly known, a linear regression procedure is used by employing the kernel method: The kernel function K measures the similarity between the input descriptor $\mathbf{X}_k$, and some predetermined reference descriptors $\mathbf{X}_i$ whose contributions to the electronic energy are known from the training dataset:

$$U_k(\mathbf{X}_k) = \sum_i K(\mathbf{X}_k, \mathbf{X}_i)\omega_i. \tag{2.26}$$

The regression coefficients ω_i can thus be determined without explicit knowledge of the relationship between $\mathbf{X}_k$ and $U_k(\mathbf{X}_k)$. With a sufficiently large training set (i.e. a large number of reference descriptors $\mathbf{X}_i$), an accurate description of the electronic energy can be expected, as long as the investigatory system exhibits an atomic environment similar to the structures in the training dataset (i.e. as long as the kernel function is not close to zero for all reference configurations).

2.5 Thermodynamics

So far, only an atomistic, microscopic description of crystalline materials has been provided. A connection to macroscopic properties will be given in the next few chapters, starting with the description of thermodynamic properties. Most material properties depend on temperature. Indeed, all materials will liquify at some temperature, and even vaporize at higher temperatures. Additionally to these phase transitions, some materials exhibit different crystal phases (different ionic configurations) at different temperatures. These transitions typically correspond to changes in the materials characteristics, such as lattice constants, elastic constants, and optical properties.

These properties even vary within the same phase with respect to temperature. In order to simulate temperature effects, knowledge of the ionic motion is needed.

2.5.1 Hellman-Feynman Theorem

The ions move within the electrostatic potential given by the electrons and the ions themselves. The forces $\mathbf{F}_j$ acting on ion j at position $\mathbf{R}_j$ can be formally calculated as

$$\mathbf{F}_j = -\nabla_{\mathbf{R}_j} E = -\frac{\partial}{\partial \mathbf{R}_j} E, \tag{2.27}$$

where E is the total energy of the electron-ion system. According to Hellman-Feynman's theorem, the derivative only acts on the Hamiltonian[9]:

$$\mathbf{F}_j = -\frac{\partial}{\partial \mathbf{R}_j} \langle \phi | \hat{H} | \phi \rangle = -\langle \phi | \frac{\partial}{\partial \mathbf{R}_j} \hat{H} | \phi \rangle . \tag{2.28}$$

This derivative of the solid-state Hamiltonian (2.1) evaluates to electron-ion and ion-ion contributions, whereas all other summands vanish:

$$\frac{\partial}{\partial \mathbf{R}_j} \hat{H} = e^2 \sum_i^{N_e} Z_j \frac{\mathbf{r}_i - \mathbf{R}_j}{|\mathbf{r}_i - \mathbf{R}_j|^3} + e^2 \sum_{\substack{l \\ l \neq j}}^{N_K - 1} Z_j Z_l \frac{\mathbf{R}_l - \mathbf{R}_j}{|\mathbf{R}_l - \mathbf{R}_j|^3}. \tag{2.29}$$

After inserting equation (2.29) into (2.28), and expressing the wave functions in real space, one finally obtains:

$$\begin{aligned} \mathbf{F}_j &= \int \phi^*(\mathbf{r}) \phi(\mathbf{r}) e^2 \sum_i^{N_e} Z_j \frac{\mathbf{r}_i - \mathbf{R}_j}{|\mathbf{r}_i - \mathbf{R}_j|^3} \mathrm{d}\mathbf{r} \\ &\quad + \int \phi^*(\mathbf{r}) \phi(\mathbf{r}) e^2 \sum_{\substack{l \\ l \neq j}}^{N_K - 1} Z_j Z_l \frac{\mathbf{R}_l - \mathbf{R}_j}{|\mathbf{R}_l - \mathbf{R}_j|^3} \mathrm{d}\mathbf{r} \\ &= \int n(\mathbf{r}) e^2 \sum_i^{N_e} Z_j \frac{\mathbf{r}_i - \mathbf{R}_j}{|\mathbf{r}_i - \mathbf{R}_j|^3} \mathrm{d}\mathbf{r} + e^2 \sum_{\substack{l \\ l \neq j}}^{N_K - 1} Z_j Z_l \frac{\mathbf{R}_l - \mathbf{R}_j}{|\mathbf{R}_l - \mathbf{R}_j|^3}. \end{aligned} \tag{2.30}$$

The forces in formula (2.30) are known as Hellman-Feynman forces. All the quantities needed for their computation are readily available from DFT calculations, thus providing an easy access to the ionic forces.

[9] The Hellman-Feynman theorem more generally states, that if the wave functions are time-independent, the spatial derivative only acts on the corresponding Hamiltonian.

2.5.2 Born Effective Charges

When ions within the crystal lattice are displaced, they also displace part of the electronic charges with them. This change of the electronic charges can be calculated within e.g. DFT. Its effect has to be considered for an accurate description of the polarization of the crystal: The ionic nominal charges are thus replaced by effective charge tensors[10] containing the nominal charges and the displaced electronic charges. However, changes in the polarization **P** induced by a displacement of an ion cannot simply be given by the change of the dipole moment of (effectively) charged ions, because the unit cell is not uniquely defined. According to the modern theory of polarization, it holds that [35]

$$\mathbf{P}[\phi] = -\frac{2ie}{(2\pi)^3} \sum_n \int_{\mathrm{BZ}} \langle u_{n\mathbf{k}} | \nabla_{\mathbf{k}} | u_{n\mathbf{k}} \rangle \, \mathrm{d}\mathbf{k}, \tag{2.31}$$

where $u_{n\mathbf{k}}$ is the cell periodic part of the electronic wave function $\phi_{n\mathbf{k}}$ of band n at **k**-point **k**. If a vanishingly small electric field **E** is applied to the material, the Kohn-Sham Hamiltonian $\hat{H}_0$ is modified to

$$\hat{H} | \phi_{n\mathbf{k}} \rangle = \hat{H}_0 | \phi_{n\mathbf{k}} \rangle - V_0 \mathbf{E} \frac{\delta \mathbf{P}[\phi]}{\delta \langle \phi_{n\mathbf{k}} |}. \tag{2.32}$$

The variation of the polarization with respect to an electronic wave function is written as [36, W11]

$$\frac{\delta \mathbf{P}[\phi]}{\delta \langle \phi_{n\mathbf{k}} |} = -\frac{ie}{2\Delta k} \sum_j^{N_k} \sum_m^{N_{\mathrm{occ.}}} \left(|u_{m\mathbf{k}_{j+1}}\rangle \langle u_{m\mathbf{k}_j} | u_{n\mathbf{k}_{j+1}} \rangle^{-1} - |u_{m\mathbf{k}_{j-1}}\rangle \langle u_{m\mathbf{k}_j} | u_{n\mathbf{k}_{j-1}} \rangle^{-1} \right), \tag{2.33}$$

with $\mathbf{k}_j$ being the **k**-points used to sample the first Brillouin zone, and $\Delta\mathbf{k} = |\mathbf{k}_{j+1} - \mathbf{k}_j|$. Only occupied bands have to be considered.
The so called Born effective charge tensor Z^*_j of atom j can finally be calculated as

$$Z^*_{jab} = \frac{V_0}{e} \frac{\partial P_a}{\partial d_b} = \frac{1}{e} \frac{\partial F_{j,a}}{\partial E_b}, \quad a, b = x, y, z, \tag{2.34}$$

where **d** is a small displacement of ion j. This description re-enables to regard the ions as charged point-like particles within the crystal lattice in order to calculate changes of the polarization.

[10] These effective charges are tensors, since a displacement of an ion in x_a direction can change the electronic charge with respect to another direction x_b.

2.5.3 Phonons

In solids, the ions cannot move unrestrained, and instead vibrate around their equilibrium positions. The magnitude of these vibrations yields the temperature of the material. The collective vibrations of the ions are called phonons, which are commonly described as quasi-particles: The vibrations exhibit specific frequencies, and can propagate within the solid. Hence, phonons can be attributed with an eigenfrequency ω and a wave vector $\mathbf{q}$. In order to calculate the phonon eigenfrequency at a given $\mathbf{q}$-point, the force constants between all ions need to be calculated. The tensor containing the force constants is referred to as the dynamical matrix.

Harmonic Theory

The dynamical matrix can be computed by using the finite differences method: The force acting on atom j if atom j' is displaced from its equilibrium structure can be written as a 3×3 matrix $\phi^{(2)}$ with

$$\overset{(2)}{\phi}_{ab}(j,j') = \frac{\partial F_a(j)}{\partial R_b(j')} = \frac{\partial^2 U(\mathbf{R})}{\partial R_a(j)\partial R_b(j')}, \tag{2.35}$$

where a, b denote cartesian coordinates, $\mathbf{F}(j)$ the force on atom j and $\mathbf{R}(j)$ its position. These terms are readily available by manually displacing each atom j' in each cartesian direction and calculating the forces onto atom j (e.g. with the previously discussed Hellman-Feynman theorem in chapter 2.5.1), yielding the force constants between two atoms. Alternatively, the force constant matrix can be seen as the second derivative of the Born-Oppenheimer energy surface $U(\mathbf{R})$ with respect to the ionic positions. The dynamical matrix can be constructed as:

$$D_{jj'}(\mathbf{q}) = \sum_{N=1}^{\infty} \frac{\overset{(2)}{\phi}(j, j'_N)}{\sqrt{m_j m_{j'}}} e^{i\mathbf{q}[\mathbf{R}(j)-\mathbf{R}(j'_N)]}. \tag{2.36}$$

The index N labels the unit cell and is introduced, because the interaction between all atoms (i.e. not only within the primitive unit cell) has to be included for solids. In practice, this sum is truncated, as the forces decay with increasing distance between atoms[11].
After diagonalizing D and inserting it into Hook's Law[12] one arrives at

$$D(\mathbf{q})\mathbf{e}(\mathbf{q},\nu) = \omega^2(\mathbf{q},\nu)\mathbf{e}(\mathbf{q},\nu). \tag{2.37}$$

The vectors $\mathbf{e}$ describe eigenvectors of D and are collective displacements of ions, i.e. phonon modes. For n atoms in a unit cell, there are $\nu = 3n$ eigenmodes for

[11] If only phonons at $\mathbf{q} = 0$ are of interest, the description can again be limited to the unit cell, since these phonons can not propagate.

[12] Even though Hook's Law is itself a harmonic approximation, this is not the harmonic approximation referred to in this chapter. Indeed, Hook's Law is also being used to describe anharmonic phonons.

each **q**-point. The eigenmodes therefore contain three cartesian coordinates for all n atoms in the unit cell. Their corresponding eigenvalues are the frequencies of the mode squared.
For non-metallic systems, an additional electronic interaction has to be taken into account for phonons at $\mathbf{q} \to 0$: As the ions oscillate, a dipole moment can be induced due to a displacement of the effective charges of the ions. Thus, the acting Coulomb force yields an additional contribution to the force constant matrix D. This correction term reads as [37, 38]

$$D_{jj'}(\mathbf{q} \to 0) = D_{jj'}(\mathbf{q} = 0) + \frac{1}{\sqrt{m_j m_{j'}}} \frac{4\pi}{V_0} \frac{\left(\sum_c Z^*_{jca}\mathbf{q}_c\right)\left(\sum_c Z^*_{jcb}\mathbf{q}_c\right)}{\sum_{cc'} \mathbf{q}_c \varepsilon_{\infty,cc'} \mathbf{q}_{c'}}, \tag{2.38}$$

where a, b, c denote cartesian indices, V_0 the unit cell volume, and Z^*_j the effective charge tensor of ion j. ε_∞ is the clamped ion dielectric tensor. This correction only applies for displacements parallel to **q**, and as such, the transversal and longitudinal phonon branches split up near $\mathbf{q} \to 0$ with respect to their frequency. This split is referred to as longitudinal-optical (LO)-transversal-optical (TO) splitting.

Anharmonic Theory

In principle, equation (2.35) can be expanded to include higher order corrections.

$$\phi = \overset{(2)}{\phi} + \overset{(3)}{\phi} + \overset{(4)}{\phi} ..., \tag{2.39}$$

$$\overset{(3)}{\phi}_{abc}(j, j', j'') = \frac{\partial^3 U(\mathbf{R})}{\partial R_a(j) \partial R_b(j') \partial R_c(j'')}, \tag{2.40}$$

$$\overset{(4)}{\phi}_{abcd}(j, j', j'', j''') = \frac{\partial^4 U(\mathbf{R})}{\partial R_a(j) \partial R_b(j') \partial R_c(j'') \partial R_d(j''')}. \tag{2.41}$$

These terms include interactions between phonons, and are thus essential for many material properties, e.g. the lattice thermal conductivity. However, already the first of these terms (i.e. the force constant matrix of third order) formally requires $(3n)^3$ separate calculations. The fourth order force constants need $(3n)^6$ calculations. Although these numbers can be heavily truncated by exploiting symmetries and considering only the largest terms, a numerically more efficient ansatz can be utilized:
The stochastic self-consistent harmonic approximation (SSCHA) implements anharmonic effects via a simple idea: The force constant matrix ϕ can be calculated as [39]

$$\phi = \overset{(2)}{\phi} + \overset{(3)}{\phi} \Lambda(\overset{(2)}{\phi})[\mathbf{1} - \overset{(4)}{\phi} \Lambda(\overset{(2)}{\phi})]^{-1} \overset{(3)}{\phi}. \tag{2.42}$$

ϕ describes the forces constants of n-th order, where the approximation $\phi = \overset{(2)}{\phi}$ is equivalent to the harmonic approximation (2.35). The matrix Λ includes eigenvectors and eigenvalues calculated within the harmonic approximation of the energy surface. Similarly to section 2.5.3, this force constant can be used to construct a dynamical matrix which can be inserted into Hook's law to calculate phonon frequencies. However,

here the forces include higher-order contributions compared to Sec. 2.5.3 and can, therefore, be considered as anharmonic corrections.
The required $3n$-dimensional energy surface $U(\mathbf{R})$ is computationally challenging to calculate. The SSCHA approximates this hypersurface by calculating $U(\mathbf{R})$ for randomly chosen ionic positions in the vicinity of its (estimated) global minimum. With sufficiently dense sampling, one can thus calculate the derivatives, and the phonon frequencies which include contributions beyond the harmonic approximation.

2.5.4 State Functions from Phonons

In order to extract thermodynamic properties (i.e. state functions), first the (grand) partition function of all phonons $\mathcal{Z}$ is needed. Assuming again that phonons are harmonic oscillators, the energy of one phonon with eigenfrequency ω is given by:

$$E_n = \hbar\omega(\mathbf{q},\nu)\left(n+\frac{1}{2}\right), \tag{2.43}$$

with n enumerating the microstate (excitation). As previously noted, the frequency of the phonon is dependent on its mode ν (displacement pattern) and its wavevector $\mathbf{q}$. Inserting E_n into the definition of the partition function one arrives at a converging geometric series[13]:

$$Z(\mathbf{q},\nu) = \sum_{n=0}^{\infty} e^{-\beta(E_n-\mu)} = \sum_{n=0}^{\infty} e^{-\beta\hbar\omega(\mathbf{q},\nu)\left(n+\frac{1}{2}\right)} = \frac{e^{-\frac{\beta}{2}\hbar\omega(\mathbf{q},\nu)}}{1-e^{-\beta\hbar\omega(\mathbf{q},\nu)}}, \tag{2.44}$$

with $\beta = 1/k_\mathrm{B}T$. This $Z(\mathbf{q},\nu)$ only corresponds to the partition function of a single mode at a single $\mathbf{q}$-point. In order to calculate the total partition function for Bosons, one has to multiply over all particles, i.e. all modes and $\mathbf{q}$-points:

$$\mathcal{Z} = \prod_{\mathbf{q},\nu} \frac{e^{-\frac{\beta}{2}\hbar\omega(\mathbf{q},\nu)}}{1-e^{-\beta\hbar\omega(\mathbf{q},\nu)}}. \tag{2.45}$$

One can calculate all state variables from $\mathcal{Z}$, for example the phononic free energy F:

$$F = -k_\mathrm{B}T \ln \mathcal{Z} = \sum_{\mathbf{q},\nu}\left[\frac{1}{2}\hbar\omega(\mathbf{q},\nu) + k_\mathrm{B}T \ln\left(1-e^{-\frac{\hbar\omega(\mathbf{q},\nu)}{k_\mathrm{B}T}}\right)\right]. \tag{2.46}$$

The derivation for other state variables relevant for this work can be found in the Appendix A.1.

[13] The introduced chemical potential μ equals zero for phonons. A closer look reveals, that $\hbar\omega(\mathbf{q},\nu) \geq 0$ and $\beta > 0$, such that $|e^{-\beta\hbar\omega(\mathbf{q},\nu)/2}| \not< 1$. However, modes with zero frequency are translations of the whole crystal, and these modes therefore can not contribute to the thermal properties of the system.

2.5.5 Thermal Conductivity

The previous ideas regarding the thermodynamic properties can be expanded to study the time evolution of a statistical ensemble with probabillity distribution $f(\mathbf{r}, \mathbf{p}, t)$, i.e. the phononic occupation number. For this case, the *Boltzmann Transport Equation*

$$\frac{\mathrm{d}f}{\mathrm{d}t} = \frac{\partial f}{\partial t} + \mathbf{v}\nabla_r f + \mathbf{F}\nabla_p f = C[f] \tag{2.47}$$

is taken into consideration. Here, $\mathbf{v} = \frac{\mathrm{d}\mathbf{r}}{\mathrm{d}t}$ and $\mathbf{F} = \frac{\mathrm{d}\mathbf{p}}{\mathrm{d}t}$ denote the velocity and forces, respectively. $C[f]$ denotes the scattering of phonons, which will lead to a transfer of heat within the system. In order to solve this equation, a common assumption for $C[f]$ is the so called *Relaxation Time Approximation*:

$$C[f] = -\frac{\delta f}{\tau}. \tag{2.48}$$

Here, δf denotes a small perturbation to f, and τ the relaxation time of the system. The Boltzmann Transport Equation Eq. 2.47 thus simplifies to

$$\delta f = \left(\frac{\partial f}{\partial t} + \mathbf{v}\nabla_r f + \mathbf{F}\nabla_p f\right)\tau. \tag{2.49}$$

Near equilibrium, the probability distribution can be approximated by

$$f = f_0 + \delta f, \tag{2.50}$$

where f_0 is the equilibrium state density given by the Bose-Einstein statistics. The lattice thermal conductivity tensor κ can then be calculated via

$$\kappa = \frac{1}{V_0 N}\sum_{\mathbf{q},\nu} c_V(\mathbf{q},\nu)\mathbf{v}(\mathbf{q},\nu) \otimes \mathbf{v}(\mathbf{q},\nu)\tau(\mathbf{q},\nu), \tag{2.51}$$

where c_V is the specific heat capacity at constant volume (which can be calculated using the formulations from Secs. 2.5.4 and A.1), $\mathbf{v}(\mathbf{q},\nu)$ is the group velocity of mode ν at q-point $\mathbf{q}$, and N is the total number of modes. The relaxation time of a phonon is commonly assumed to be given by the lifetime of the phonon itself, which is calculated using

$$\begin{aligned}\tau(\mathbf{q},\nu) &= \frac{1}{2\Gamma(\mathbf{q},\nu)},\\ \Gamma(\mathbf{q},\nu) &= \frac{18\pi}{\hbar^2}\sum_{\mathbf{q},\nu',\nu''} |\phi_{-\nu\nu'\nu''}|^2 \left\{(n'+n''+1)\left[\delta(\omega-\omega'-\omega'') + \delta(\omega+\omega'+\omega'')\right]\right.\\ &\qquad \left.(n'-n'')\left[\delta(\omega+\omega'-\omega'') - \delta(\omega-\omega'+\omega'')\right]\right\},\end{aligned} \tag{2.52}$$

where $\phi_{-\nu\nu'\nu''}$ denotes the third order force constant tensor describing the scattering of mode ν at $\mathbf{q}$-point $-\mathbf{q}$ and modes ν' and ν'' at $\mathbf{q}$-point $\mathbf{q}$. $n = n(\mathbf{q}, \nu)$ is the phonon occupation number of mode ν at $\mathbf{q}$-point $\mathbf{q}$.
The group velocity of a specific phonon mode can be extracted from Eq. 2.37:

$$\mathbf{v}(\mathbf{q}, \nu) = \sum_a \frac{\partial \omega(\mathbf{q}, \nu)}{\partial q_a} \hat{e}_a = \frac{1}{2\omega(\mathbf{q}, \nu)} \sum_{jj', abc} e_b(j, \mathbf{q}, \nu) \frac{\partial D_{ab}(jj', \mathbf{q})}{\partial q_a} e_c(j', \mathbf{q}, \nu) \hat{e}_a \tag{2.53}$$

2.6 Mechanical Properties

With knowledge of the full electron-ion system one can study macroscopic properties of the crystal lattice. It is assumed that all crystals are in mechanical equilibirum with the vacuum, i.e. the internal pressure of the crystal (and hence of all unit cells) has to equal zero.

2.6.1 Murnaghan Equation of State

The bulk modulus K is defined as the change in internal pressure p with respect to a change in volume V. Expanding K in a Taylor series up to first order yields the differential equation:

$$K = -V \frac{\mathrm{d}p}{\mathrm{d}V} = K_0 + pK_0' + \mathcal{O}(p^2). \tag{2.54}$$

Assuming $p(V_0) = 0$ (i.e. no internal pressure at the equilibrium volume V_0), the solution to 2.54 is given by:

$$p(V) = \frac{K_0}{K_0'} \left[\left(\frac{V_0}{V} \right)^{K_0'} - 1 \right]. \tag{2.55}$$

Inserting equation 2.55 into the first law of thermodynamics

$$\mathrm{d}F = -p\mathrm{d}V - S\mathrm{d}T = -p\mathrm{d}V, \tag{2.56}$$

yields an expression for the free energy F of the system:

$$F(V) = -\int_{V_0}^{V} p(V)\mathrm{d}V = \frac{K_0 V}{K_0'} \left[\left(\frac{V_0}{V} \right)^{K_0'} \frac{1}{K_0' - 1} + 1 \right]. \tag{2.57}$$

Here, a constant temperature T is assumed, such that $\mathrm{d}T = 0$.
For a system in equilibrium, the free energy has to be minimal. Therefore, with knowledge of $F(V)$, one can extract the equilibrium volume V_0. Note that according to Eq. (2.46) the free energy also depends on temperature. The volumetric thermal expansion can be obtained by solving the Murnaghan equation of state (2.57) for different, fixed temperatures. Since harmonic phonon frequencies calculated at a

fixed volume enter Eq. (2.57), the resulting thermal expansion $V(T)$ will in turn effect the phonon frequencies at each temperature. Therefore, the phonon frequencies can be revised beyond the harmonic approximation, by including the thermal expansion of the lattice. This approximation is referred to as quasi-harmonic approximation (QHA).

2.6.2 Elasticity

In general, materials are anisotropic, i.e. their properties depend on the materials orientation within a given experimental setup. For example, the bulk modulus K defines how a material reacts under hydrostatic bulk compression, but cannot describe its behaviour under uniaxial strain. In order to generalize such properties, a tensor is needed that describes the effect of directional strain applied to the material. A strained lattice vector $\mathbf{R}'$ can be described as $\mathbf{R}' = (\mathbf{1} + \eta)\,\mathbf{R}$, with $\mathbf{R}$ denoting the unstrained lattice vector, and η being the strain tensor. Exemplary strain tensors and their effect on a 2D lattice are showcased in Figure 3.

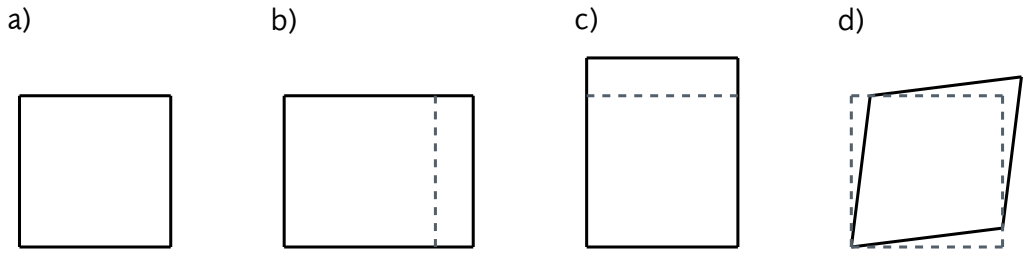

Figure 3: Different strains on a 2D crystal: (a) defines the unstrained cell, (b) describes a normal strain in x-direction, (c) a normal strain in y-direction, and (d) a shear strain in xy-direction. The corresponding strain tensors are: $\eta^{(a)} = 0$, $\eta^{(b)} = \begin{pmatrix} \eta & 0 \\ 0 & 0 \end{pmatrix}$, $\eta^{(c)} = \begin{pmatrix} 0 & 0 \\ 0 & \eta \end{pmatrix}$, and $\eta^{(d)} = \frac{1}{2}\begin{pmatrix} 0 & \eta \\ \eta & 0 \end{pmatrix}$.

Expanding the free energy F in a Taylor series around the equilibrium structure at $\eta = 0$, i.e. the structure with no strain yields:

$$F(\eta, V, T) = F(0, V_0, T) + \left(\frac{\partial F(\eta, V, T)}{\partial \eta}\right)\eta + \frac{1}{2}\left(\frac{\partial^2 F(\eta, V, T)}{\partial \eta^2}\right)\eta^2 + \mathcal{O}(\eta^3), \quad (2.58)$$

where V_0 describes the volume at the equilibrium. As η is a symmetric 3×3 matrix, the above equation is meant figuratively, i.e. the change of F with respect to an applied strain η is being tracked. According to the thermodynamic equilibrium condition, the free energy has to be minimal for a system in equilibrium, and hence first order derivatives will vanish. One defines the (second order) isothermal elastic constants C as:

$$C_{ijkl} = \frac{1}{V_0}\left(\frac{\partial F(\eta, V, T)}{\partial \eta_{ij}}\right)\left(\frac{\partial F(\eta, V, T)}{\partial \eta_{kl}}\right). \quad (2.59)$$

It is convenient to divide equation (2.58) by the equilibrium volume V_0, and only track the changes in energy, which are induced by the applied strain. Then (2.58) reads in tensor component form:

$$\frac{1}{V_0}\left[F(\eta,V,T)-F(0,V_0,T)\right]=\frac{1}{2}\sum_{ijkl}C_{ijkl}\eta_{ij}\eta_{kl}+\mathcal{O}(\eta^3). \tag{2.60}$$

Note, that the strain tensor η is a symmetric 3×3 matrix and, therefore, has only six independent entries. Consequently, the elasticity tensor C only has 21 independent entries[14]. Typically, physicists use the so called Voigt contracted notation to simplify the labeling:

ij	11	22	33	23/32	13/31	12/21
a	1	2	3	4	5	6

The elasticity tensor C has complete Voigt symmetry such that $C_{ijkl}=C_{klij}=C_{jikl}=...$, or in Voigt notation simply $C_{ab}=C_{ba}$.
An upper bound for the bulk modulus K (introduced in equation (2.54)) can be readily calculated in the Voigt average of the elastic constants:

$$9K=\left(C_{11}+C_{22}+C_{33}\right)+2\left(C_{12}+C_{13}+C_{23}\right). \tag{2.61}$$

Similar to the bulk modulus, a directionless shear modulus G describing the materials behaviour under shear stresses can be calculated as:

$$15G=\left(C_{11}+C_{22}+C_{33}\right)-\left(C_{12}+C_{23}+C_{13}\right)+3\left(C_{44}+C_{55}+C_{66}\right). \tag{2.62}$$

2.6.3 Piezoelectricity

Piezoelectricity refers to a change of a crystal's polarization with respect to an applied strain, which can be formulated as

$$e_{ia}=\left(\frac{\partial D_i}{\partial \eta_a}\right)_{\mathbf{E}}, \tag{2.63}$$

where **D** denotes the electric displacement field, **E** the (constant) electric field, and e the direct piezoelectric tensor. The tensor components are given in Voigt notation, if applicable. Similarly, the inverse piezoelectric effect describes the accumulation of internal stress under an applied electric field. All crystal classes without inversion symmetry show this effect[15]. Analogously, the converse piezoelectric tensor can be defined as

$$d_{ia}=\left(\frac{\partial D_i}{\partial \sigma_a}\right)_{\mathbf{E}}, \tag{2.64}$$

[14] The maximum number of independent entries of the elasticity tensor is 21, but this case only occurs for triclinic unit cells. Additional symmetries of the unit cell will further reduce the number of independent entries.

[15] The cubic point group 432 (international notation) is the only exception to this rule.

where σ denotes the stress tensor, which is linked to the strain tensor via Hook's Law:

$$\sigma_a = \sum_b C_{ab}\eta_b. \tag{2.65}$$

Consequently, the direct and converse piezoelectric tensors can be converted into each other, e.g. [40]

$$d_{ia} = \sum_b C_{ba}^{-1} e_{ib}. \tag{2.66}$$

Using Maxwell's relations and the formulation outlined in Sec. 2.5.2, the direct piezoelectric tensor can be calculated by [W11]

$$e_{ia} = \left(\frac{\partial D_i}{\partial \eta_a}\right)_{\mathbf{E}} = -\left(\frac{\partial \sigma_a}{\partial E_i}\right)_{\eta}. \tag{2.67}$$

Since the piezoelectric tensors link between mechanical deformations and subsequent creation of a dipole moment (or vice versa), no isotropic piezoelectric materials can exist. Hence, piezoelectricity is an exclusive property of non-centrosymmetric crystals.

2.7 Optical Properties

The optical properties of a material are governed by its response to an external electrical field (i.e. photons). This includes for example the absorption, reflection, and transmittance of light. On a macroscopic scale, these interactions are given by material constants. But in order to calculate these constants, a microscopic description is needed that takes into account the interaction between photons and electrons or phonons. The excitations of these (quasi-) particles can then be used to determine the macroscopic material constants.
The interaction between photons and a material mainly depends on the mobility of charge carriers within the material itself. In this work, only crystalline semiconductors are considered, where the charges cannot move freely within the crystal. Thus, electric fields cannot be screened, and the crystal will become polarized. Depending on the frequency of the electric field, the charges are too sluggish to react, such that no polarization can be built up. Hence, the frequency of an external electrical field massively influences the response of a material.

2.7.1 Classical Description

The polarization **P** of a material is defined as

$$\mathbf{P}(\omega) = \chi(\omega)\mathbf{E}(\omega) + \chi_2(\omega)\mathbf{E}(\omega)\mathbf{E}(\omega) + ...,$$

where **E** is an external electric field and χ_n is called dielectric susceptibility of order n. Typically, χ and **P** are dependent on the frequency ω of the external electric field.

Here, only the linear component χ will be discussed. Also, instead of χ the dielectric function ε will be used:

$$\varepsilon(\omega) = 1 + \chi(\omega). \tag{2.68}$$

ε is a complex quantity that obeys the Kramers Kronig relation:

$$\begin{aligned} \varepsilon_r(\omega) &= 1 + \frac{2}{\pi}\wp\int_0^\infty \frac{\omega'\varepsilon_i(\omega')}{\omega'^2 - \omega^2}d\omega', \\ \varepsilon_i(\omega) &= 1 - \frac{2\omega}{\pi}\wp\int_0^\infty \frac{\varepsilon_r(\omega')}{\omega'^2 - \omega^2}d\omega', \end{aligned} \tag{2.69}$$

where $\wp$ denotes the Cauchy principal value of the integral.
More common optical quantities can be extracted by a further evaluation: According to Maxwell's equations, light can be expressed as an electromagnetic wave:

$$\nabla^2\mathbf{E} = \frac{\mu\varepsilon}{c^2}\frac{\partial^2\mathbf{E}}{\partial t^2} \tag{2.70}$$

where μ is the magnetic susceptibility. In the following, only non-magnetic materials are discussed, such that $\mu = 1$. The solution to this wave equation is then given as

$$\mathbf{E} = \mathbf{E}_0 e^{i(\mathbf{qr}-\omega t)}, \qquad |\mathbf{q}|^2 = \frac{\omega^2}{c^2}\varepsilon, \tag{2.71}$$

with $\mathbf{E}_0$ and $\mathbf{q}$ the amplitude and wave vector, respectively. The wave vector $\mathbf{q}$ is a complex quantity: Its real part describes the propagation of the wave, while its imaginary part describes the attenuation of the wave in matter[16]. In experiments, one typically does not measure ε, but the related quantities

$$N = \sqrt{\varepsilon} = n + i\kappa, \qquad R = \left|\frac{N-1}{N+1}\right|^2, \qquad T = 1 - R. \tag{2.72}$$

N is called complex refractive index, n is the refractive index and κ the optical extinction coefficient. R and T are the reflectance and transmittance, respectively. These three quantities can be directly calculated from the dielectric function:

$$\kappa = \frac{1}{\sqrt{2}}\sqrt{\sqrt{\varepsilon_r^2 + \varepsilon_i^2} - \varepsilon_r}, \qquad n = \frac{1}{\sqrt{2}}\sqrt{\sqrt{\varepsilon_r^2 + \varepsilon_i^2} + \varepsilon_r}. \tag{2.73}$$

The general characteristics of the dielectric response ε of a para-or ferroelectric crystal as a function of the frequency of the external electric field ω is given in Fig. 4: For small frequencies, the internal dipole moments (resulting from electrons and ions)

[16] In vacuum it holds that $\varepsilon = 1$ and no decaying of the wave is observed

are realigned (orientation polarization). As the frequency increases, these permanent dipoles cannot follow, and thus yield no contribution to the dielectric response for higher frequencies. Their frequency-dependent behaviour is governed by the Debye formula [41] (blue section). This effect will not be discussed in further chapters (see e.g. Ref. [41] for a detailed overview). The frequencies where orientation polarization plays a major role for the dielectric response are typically much smaller compared to phonon frequencies ($\approx 10^{13} - 10^{14}$ Hz, red section), which in turn are much smaller than frequencies needed for electronic excitations ($\approx 10^{16}$ Hz, green section). Within the infrared region, the dielectric function will exhibit a peak corresponding to each active TO phonon frequency. For higher excitation energies, no phonons can be activated, and the dielectric spectrum is instead governed by electronic resonances. For even higher frequencies, the material cannot react to the external field, and the dielectric function remains at the constant value of one, i.e. no polarization is built up. All these effects add up to the total dielectric function at each excitation frequency: The static contributions are labelled in accordance with prevalent literature as $\varepsilon_{\text{orient.}}$, $\varepsilon_{\text{st.}}$, and ε_{∞}, corresponding to the low-frequency limit of the orientation, ionic, and electronic dielectric function, respectively. Both, the electronic and phononic couplings to an external electric field will be discussed in the next sections.

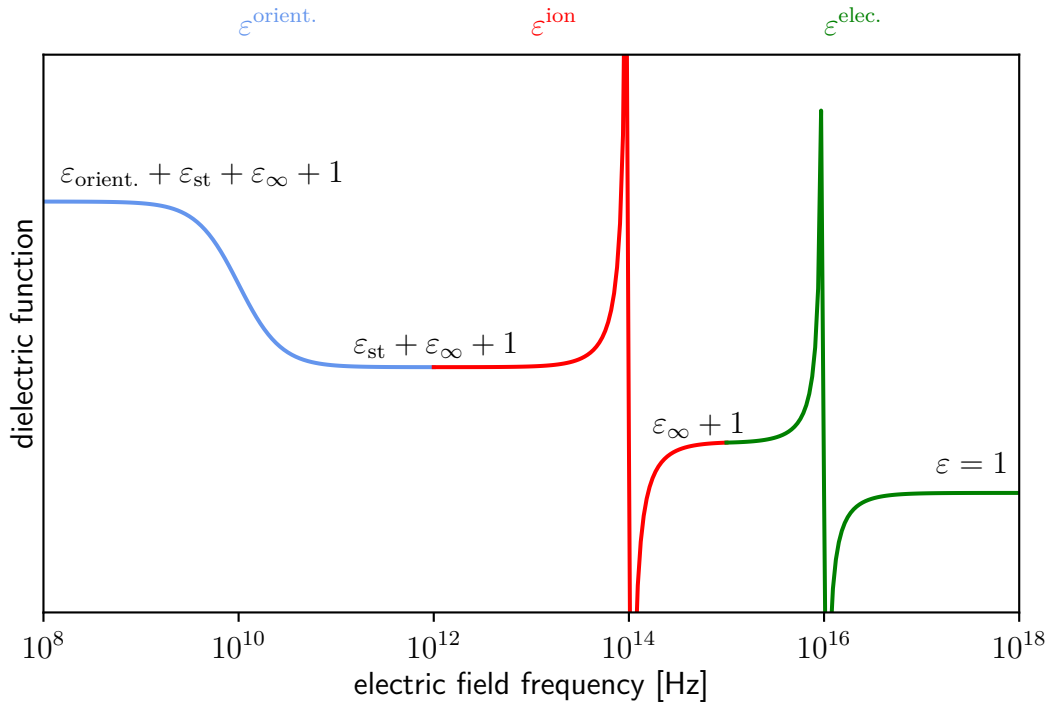

Figure 4: Schematic progresssion of the dielectric function of a paraelectric crystal for different electric field frequencies.

2.7.2 Quantum Mechanical Description

Generally, a quantummechanical treatment will be necessary to describe the differences in the optical response of different materials. Therefore, a practical way to calculate ε microscopically within quantum mechanics is needed.
In this chapter, only the electrons may interact with the electric field (the phononic interactions will be covered in chapter 2.8). If the energy of the electric field is sufficiently large, it may excite an electron from its initial state. According to Fermi's golden rule, the corresponding absorption rate R is given by

$$R = \frac{2\pi}{\hbar} \left| \langle i | \hat{H} | f \rangle \right|^2, \tag{2.74}$$

where i and f label the electrons initial and final state, respectively. The frequency of the external electric field is ω, and $\hat{H}$ is the Hamilton operator of the electron interacting with this field. This absorption rate corresponds to a loss of energy of the electric field, given by $\Delta E = R\hbar\omega$. This energy loss can be directly related to the imaginary part of the dielectric function:

$$\begin{aligned} I(t) &= \frac{n^2}{8\pi} |\mathbf{E}(\omega)|^2 = \frac{n^2}{8\pi} \left| \mathbf{E}_0 e^{i\omega(xN/c - t)} \right|^2 = \frac{N^2}{8\pi} \mathbf{E}_0 e^{-2\omega\kappa x/c}, \\ -\frac{\partial I}{\partial t} &= -\frac{\partial I}{\partial x}\frac{\partial x}{\partial t} = \frac{2\omega\kappa}{c} I \frac{c}{n} = \frac{\varepsilon_i \omega}{n^2} I = R\hbar\omega, \\ \Rightarrow \varepsilon_i &= \frac{\hbar n^2}{I} R = \frac{16\pi^2}{|\mathbf{E}(\omega)|^2} \left| \langle i | \hat{H} | f \rangle \right|^2, \end{aligned} \tag{2.75}$$

where I is the intensity of the incoming wave. With knowlegde of the imaginary part of the dielectric function over the whole frequency range, one can calculate its real part via Kramers Kronig relations. Hence, in order to yield all macroscopic optical quantities, the Hamiltonian in (2.74) and its effect on the electronic states have to be determined.

2.7.3 Independent Particle Approximation

Assuming the Coulomb gauge[17] one may write the electric field in terms of its vector potential $\mathbf{A}$:

$$\mathbf{E}(\mathbf{r}, t) = -\frac{\partial \mathbf{A}(\mathbf{r}, t)}{\partial t}. \tag{2.76}$$

The Hamilton operator for one electron now reads as:

$$\hat{H} = \frac{1}{2m} \left[\hat{p} + e\mathbf{A}(\mathbf{r}, t) \right]^2 + V(\mathbf{r}). \tag{2.77}$$

In the Coulomb gauge, the operators $\hat{p}$ and $\mathbf{A}$ commute, such that:

$$\begin{aligned} \hat{H} &= \frac{\hat{p}^2}{2m} + V(\mathbf{r}) + \frac{e}{m}\mathbf{A}\hat{p} + \mathcal{O}(\mathbf{A}^2) \\ &= \hat{H}_0 + \hat{H}_{\mathsf{ES}}. \end{aligned} \tag{2.78}$$

[17] The electric scalar potential $\phi(\mathbf{r}, t) = 0$ (i.e. no external charges), and $\nabla \mathbf{A}(\mathbf{r}, t) = 0$

The first two terms yield the motion of the electron in a potential V, whereas only the last two terms describe its interaction with an external electric field.
In a first approximation, one can treat $\hat{H}_{\mathrm{ES}}$ as a small perturbation to $\hat{H}_0$. For simplicity, $V(\mathbf{r})$ shall be constant with respect to time. For a crystalline system, the eigenstates of $\hat{H}_0$ may be given by Bloch functions. The task is then to calculate the transition elements[18]

$$\langle v|\, \hat{H}_{\mathrm{ES}}\, |c\rangle = \frac{e}{m} \langle v|\, \mathbf{A}\hat{p}\, |c\rangle\,, \tag{2.79}$$

with v and c labelling valence and conduction band states, respectively.
Transitions from all valence bands to all conduction bands at all **k**-points have to be considered. In total, the imaginary part of the dielectric function reads as:

$$\begin{aligned}\varepsilon_i(\omega) &= \sum_{c,v,\mathbf{k}} \frac{16\pi^2}{|\mathbf{E}(\omega)|^2} \left|\langle v|\, \hat{H}_{\mathrm{ES}}\, |c\rangle\right|^2 \\ &= \lim_{q\to 0} \frac{4e^2\hbar^4}{q^2m^2} \sum_{c,v,\mathbf{k}} \delta(E_c - E_v - \hbar\omega) \left| \int u_v^*(\mathbf{k}) e^{i\mathbf{k}\mathbf{r}'} \nabla u_c(\mathbf{k}) \mathrm{d}\mathbf{k} \right|^2 . \end{aligned} \tag{2.80}$$

Essentially, the number of possible transitions between valence and conduction bands are counted for each energy, and weighted according to their orbital overlap. The eigenfunctions and energies are typically obtained within DFT or GWA. The interactions between an excited electron and its corresponding hole in the valence band are neglected in this approach. Furthermore, the DFT is only valid for ground states, i.e. the conduction band states cannot be assumed to be correct. In most cases however, the independent particle approximation (IPA) is qualitatively still in good agreement to experimental measurements, while keeping the computational effort relatively small [42, P2].

2.8 Vibrational Spectroscopy

Photons cannot only couple to electrons, but also to phonons. Vibrational spectroscopy can be used to determine phonon frequencies, and serves to "fingerprint" a given material or functional group. The spectra are sensitive to the crystal's orientation and stoichiometry, making vibrational spectroscopy an integral part for assessing the quality of a given sample. Not all phonons can interact with photons: Only those whose ionic displacement pattern changes either the ionic dipole moment, or the crystal's electric susceptibility, may be probed by vibrational spectroscopy. The former case corresponds to IR spectroscopy, and the latter to Raman spectroscopy. The optically inactive modes are referred to as "silent" modes.

[18] Equation (2.79) describes the only possible transitions in semiconductors and insulators. For metals, transitions within the same state (called intraband transitions) are possible, and the initial and final states do not need to be valence- and conduction-band states. The term $\langle v|\, \hat{H}_0\, |c\rangle$ equals zero, since v and c label orthogonal eigenstates of $\hat{H}_0$.

2.8.1 Infrared Spectroscopy

A photon can be absorbed if its frequency matches an IR-active phonon mode, by activating (creating) that specific mode. The frequencies at which such absorptions take place can be measured via e.g. transmission spectroscopy. The correpsonding oscillator strength (the rate of absorption) is given by the change of the ionic dipole moment induced by the phononic eigenvector. The dipole moment $\mathbf{p}$ of the crystal can formally be defined as

$$\mathbf{p} = \sum_b p_b \hat{e}_b = \sum_b \left(\sum_{i,a} Z^*_{iab} \mathbf{r}_i \hat{e}_a \right) \hat{e}_b, \tag{2.81}$$

where $\mathbf{r}_i$ is the position of ion i and Z^*_{iab} is its effective charge tensor (e.g., the Born charge). The vectors $\hat{e}_{a,b}$ label the cartesian unit vectors and the indices a, b the cartesian coordinates. The change of $\mathbf{p}$ with respect to a phonon with eigenmode Q can be approximated with a symmetric difference quotient:

$$\frac{\partial \mathbf{p}}{\partial Q} \sim \mathbf{p}(\mathbf{R}_+) - \mathbf{p}(\mathbf{R}_-) = \sum_b \left(\sum_{i,a} Z^*_{iab} \mathbf{Q}_i \hat{e}_a \right) \hat{e}_b, \tag{2.82}$$

where $\mathbf{p}(\mathbf{R}_\pm)$ denotes the dipole moment for the ionic positions at displacements Q in either direction, $\mathbf{Q}_i$ denotes the movement of ion i. The derivative with respect to the vector Q is meant figuratively, as the change of $\mathbf{p}$ with respect to the collective displacement Q. The imaginary part of the ionic contribution to the dielectric function can then be calculated as [38]:

$$\begin{aligned} \Im\left(\varepsilon^{\text{ion}}_{ab}(\omega_m)\right) &\sim \left(\frac{\partial p_a}{\partial Q}\right) \left(\frac{\partial p_b}{\partial Q}\right)^* \\ &= \left(\sum_{i,a'} Z^*_{ia'a} \mathbf{Q}_i \hat{e}_{a'} \right) \left(\sum_{i,a'} Z^*_{ia'b} \mathbf{Q}_i \hat{e}_{a'} \right)^*, \end{aligned} \tag{2.83}$$

with ω_m being the frequency of mode m with displacement pattern Q. The contribution of all phonon modes to the IR spectra is obtained by calculating the sum over all modes m. In the harmonic approximation for phonons, these contributions will only contain delta peaks at the phonon frequencies ω_m. The real part of the ionic contribution to the dielectric function can be obtained via Kramers Kronig relations as shown in Ref. [38]:

$$\Re\left(\varepsilon^{\text{ion}}_{ab}(\omega)\right) = \frac{4\pi}{V_0} \sum_m \frac{\Im\left(\varepsilon^{\text{ion}}_{ab}(\omega)\right)}{\omega_m^2 - \omega^2}. \tag{2.84}$$

2.8.2 Raman Spectroscopy

In Raman spectroscopy, photons interact via the electric susceptibility with phonons by exciting an electron to a virtual state, which is typically at much higher energies

than the phononic vibrations. A large portion of the absorbed light is elastically scattered as the electron relaxes back to its ground state (Rayleigh scattering), but part of it can inelastically scatter by creating or annihilating phonons. The scattered light thus has a different energy than the incident light used for the electronic excitation, called Raman shift. The latter processes are referred to as Stokes- and anti-Stokes Raman scattering, respectively. All three effects are schematically summarized in Fig. 5.

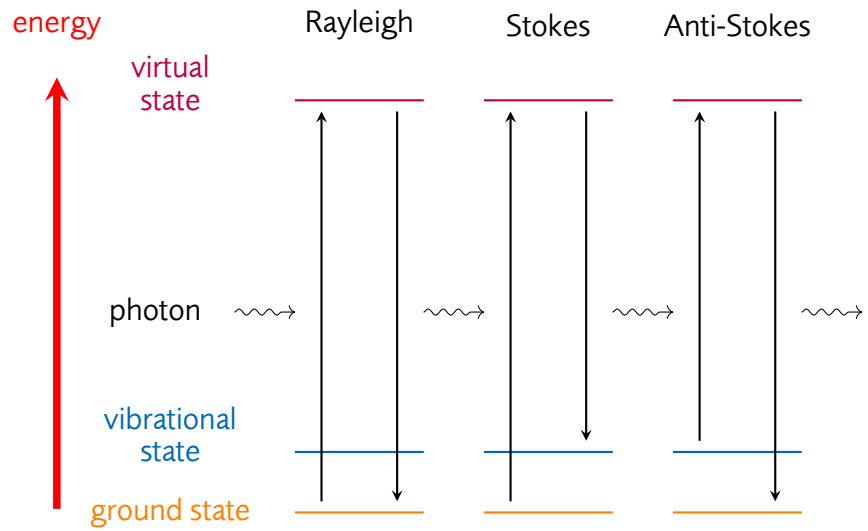

Figure 5: Energetic diagram of the Raman effect.

The scattering intensities are given by the Raman tensor α, which is defined as the change of the polarizability with respect to a phononic eigenmode Q. Similarly to the previous section, a symmetric difference quotient can be used to calculate α:

$$\alpha_{m,ab}(\omega) = \frac{\partial \chi^{\text{el}}_{ab}(\omega)}{\partial Q} = \frac{\partial \varepsilon^{\text{el}}_{ab}(\omega)}{\partial Q} \sim \varepsilon^{\text{el}}_{\mathbf{R}_+,ab}(\omega) - \varepsilon^{\text{el}}_{\mathbf{R}_-,ab}(\omega), \tag{2.85}$$

with $\varepsilon^{\text{el}}(\omega)$ being the electronic contribution to the dielectric function (e.g. Eq.(2.80)) and ω the frequency of the incident laser light. The electronic contribution to the dielectric function is typically calculated within the IPA. The Stokes Raman intensity of a transversal phonon can finally be calculated as:

$$I_m(\omega)[s(ab)i] \sim |\hat{e}_s \alpha_{m,ab}(\omega) \hat{e}_i|^2 \frac{(\omega - \omega_m)^4}{\omega_m}(n+1), \tag{2.86}$$

where $\hat{e}_i$ and $\hat{e}_s$ denote the polarization of the incident and scattered light respectively, and n is the Bose-Einstein distribution. Instead, for the anti-Stokes case, the phonon and photon frequencies are added up and the thermal population correction is only given by the Bose-Einstein distribution. Equation (2.86) is only valid for transversal phonons. For longitudinal phonons, an additional term including the second order polarizability χ_2 has to be considered, since LO modes couple with the electric field that they themself induce [43].

2.9 Landau Theory

Of particular interest in ferroelectrics is the phase transition towards the paraelectric configuration. Since the stable state minimizes the free energy of the system, a critical temperature T_C called the Curie temperature[19] exists that determines which phase below or above this temperature is stable.
Accoring to Landau theory, the free energy of the high-temperature phase can be expanded in vincinity of the transition temperature with respect to an order parameter in a Taylor series. In ferroelectrics, this order parameter is given by the spontaneous polarization P_S. Since the free energy should be symmetric under a flip of the sign of P_S, i.e. $F(P_S) = F(-P_S)$, only even powers contribute to the expansion, such that

$$F(T, P_S) = F_0(T) + a(T)P_S^2 + bP_S^4 + cP_S^6 + \mathcal{O}(P_S^8), \tag{2.87}$$

where F_0 is the energy of the high-symmetry phase with vanishing polarization. The corresponding free energy landscapes are schematically shown in Fig. 6.

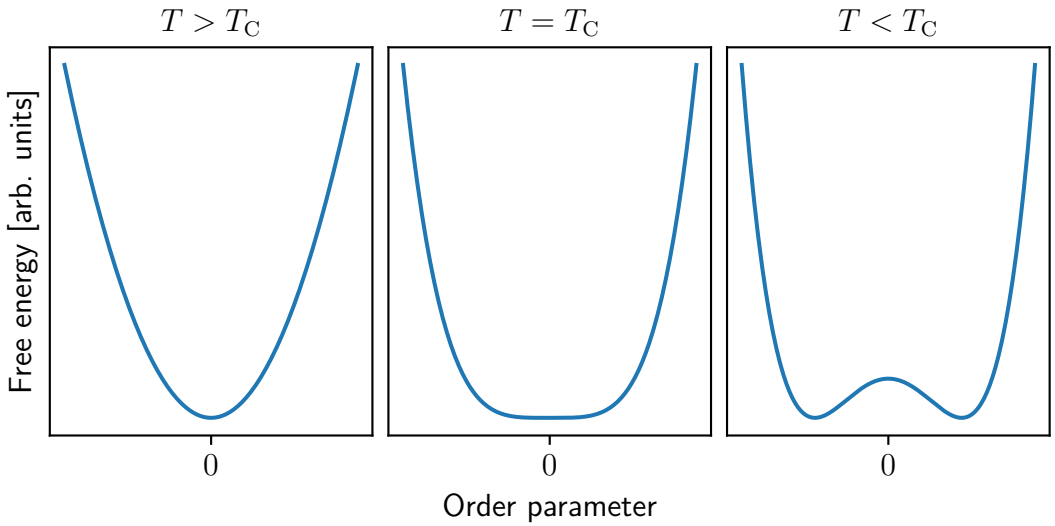

Figure 6: Schematic free energy surface above the critical temperature (left), at the critical temperature (middle), and below the critical temperature (right). The minima denote the respective equilibrium positions of the system.

Depending on the sign of the expansion coefficient b, two distinct types of phase transitions can be identified: If $b < 0 \quad \forall T$, then both a and c must be positive, ensuring that F remains positive for high values of the order parameter P_S. The parameter a is expressed via $a(T) = a_0(T - T_0)$, since a needs to change its sign near the transition temperature. To enforce a local minimum of the free energy at the transition

[19] In general, there are several intensive state variables that can control phase transitions. For example, the application of high temperature and pressure can induce a phase transition from graphite to diamond.

temperature T_*, the conditions

$$\begin{aligned} 0 &= a(T_*)P_S^2 + bP_S^4 + cP_S^6, \\ 0 &= 2a(T_*)P_S + 4bP_S^3 + 6cP_S^5, \end{aligned} \tag{2.88}$$

have to be fulfilled. It follows that $P_S^2(T_*) = b/2c \neq 0$, and $a(T) = a_0(T - T_0) = b^2/2c$. In total, the order parameter then reads as

$$P_S = \begin{cases} \frac{b}{2c}\left(1 + \sqrt{1 - \frac{4a(T)c}{b^2}}\right) & , T < T_\mathrm{C} \\ 0 & , T \geq T_\mathrm{C} \end{cases}, \tag{2.89}$$

For a phase transition of second order, it is assumed that $b(T) > 0 \quad \forall T$. All terms of higher order in P_S can be ignored. Again, a has to switch sign at the critical temperature and is rewritten as $a(T) = a_0(T - T_\mathrm{C})$. After minimizing the free energy, one obtains

$$F(T) = \begin{cases} F_0 - \frac{a_0^2}{2b_0}(T - T_\mathrm{C})^2 & , T < T_\mathrm{C} \\ F_0 & , T \geq T_\mathrm{C} \end{cases}. \tag{2.90}$$

Near the critical temperature, the order parameter then behaves like

$$P_S = \begin{cases} \sqrt{-\frac{a_0}{2b}(T - T_\mathrm{C})} & , T < T_\mathrm{C} \\ 0 & , T \geq T_\mathrm{C} \end{cases}, \tag{2.91}$$

and the so called critical exponent of the system is $\nu = 1/2$.
Thus, the different types of transition can be distinguished by the behavior of the order parameter near the critical temperature: If the order parameter has a discontinuity at the transition temperature, the corresponding phase transition is of first order. If it instead continuously vanishes at the Curie temperature, the transition is of second order. The discontinuity in the order parameter in first order transitions also implies a discontinuity of the entropy, which in turn implies a latent heat during the phase transition. The behavior of the order paramter for both first- and second order phase transitions is schematically shown in Fig. 7.
The phase transition is further classified by the atomic movements involved: In a *displacive* phase transition, the atomic positions shift only slightly (smaller than the interatomic bond lengths). This type of transition might also involve distortions of the underlying lattice. If a transition is instead of *order-disorder* type, the atomic configuration changes from an ordered state to a disordered one after the phase transition. The most prominent example of such transitions is the Ising model [44].

2.10 Computational Details

Throughout this work, the quantum-mechanical computations are performed within DFT as implemented in the Vienna Ab Initio Simulation Package (VASP) code. Instead of plane waves as described in Eq. (2.5), projector augmented waves (PAWs)

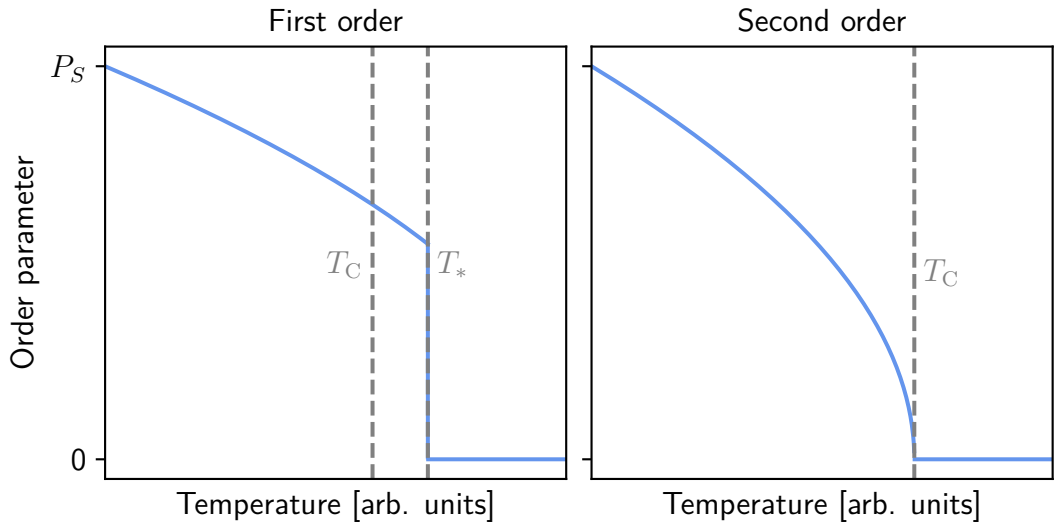

Figure 7: Evolution of the order parameter as a function of temperature, for phase transitions of first order (left), and second order (right).

are used for the expansion series of the electronic wave function: Since all electronic wave functions have to be orthorgonal to each other, the valence electrons feature rapid oscillations near the ionic cores, where the strongly bound core electrons are localized. Hence, a large number of plane wave coefficients would need to be considered in the expansion series. The PAW ansatz projects the Kohn-Sham wave function to a pseudo wave function via a projection operator $\mathcal{T}$:

$$|\Phi_a\rangle = \mathcal{T}\,|\tilde{\Phi}_a\rangle = |\tilde{\Phi}_a\rangle + \sum_i \left(|\phi_i\rangle - |\tilde{\phi}_i\rangle\right) \langle p_i|\tilde{\Phi}_a\rangle\,, \tag{2.92}$$

where Φ_a denotes a one-electron Kohn-Sham wavefunction, and $\tilde{\Phi}_a$ the projected, fictious wave function. Both these functions are expanded in a series of partial waves ϕ_i and $\tilde{\phi}_i$, respectively. $\tilde{\phi}_i$ is only defined within a pre-defined radius around the ionic core. The corresponding expansion coefficients in this core region are expressed via a projector function p_i, i.e. $\langle\tilde{\phi}_i|p_j\rangle = \delta_{ij}$. Consequently, the operator $\mathcal{T}$ only affects the electronic wave function within the core region. The electronic wave function is thus decomposed into two regions: The plane wave ansatz is used far away from the ionic cores, whereas the wave function continously transitions to a projected part within a cutoff radius. This leads to a significantly reduced number of expansion coefficients for an accurate description of the electronic wave function, compared to a purely plane wave based ansatz.

The potentials used for the exchange-correlation part of the Kohn-Sham equations are provided within VASP in the PBEsol formulation, and electronic configurations $1s^2 2s^1$, $4p^6 4d^3 5s^2$, $5s^2 5p^6 5d^3 6s^2$ and $2s^2 2p^4$ are employed for Li, Nb, Ta, and oxygen (O), respectively. All other electrons are presumed to be physically inert due to their large binding energies, and are thus *frozen* within the ionic cores.

The cutoff energy and k-point meshes used are 450 eV and 6×6×6 per rhombohedral unit cell, respectively. A Gaussian smearing with width 0.02 eV is applied to the

occupancies of the electronic states for numerical stability. A convergence within 1 meV of the electronic energy per atom is thus achieved. For all calculations, the ionic positions are optimized such that the acting Hellmann-Feynman forces in each direction are lower than 0.005 eV $Å^{-1}$ per ion. Additional numerical parameters or changes thereof are discussed at the beginning of each chapter.
All calculations are performed on the justHPC Cluster of the Justus-Liebig-Universität Gießen, the Lichtenberg II Cluster of the Technische Universität Darmstadt, and at the Höchstleistungsrechenzentrum Stuttgart (HLRS).

3 Lithium Niobate and Lithium Tantalate

3.1 Crystal Structure & Symmetries

Both, ferroelectric LN and LT crystallize within the space group R3c and thus belong to the trigonal crystal family. The crystals are isomorphic, and undergo a phase transition towards a paraelectric phase (space group R3$\bar{c}$) at higher temperatures. The primitive unit cell is given by a rhombohedral lattice, containing two formula units. The conventions established in Ref. [7] are used throughout this work, such that the polar crystal axis lies parallel to the cartesian z-axis (extraordinary axis), and the basal plane is defined parallel to the xy-plane (parallel to the ordinary axes). Commonly, instead of referring to the primitive rhombohedral unit cell, a hexagonal unit cell is used for defining e.g. the lattice constants. Alternatively, an orthorhombic unit cell can be constructed. All these three unit cells are shown in Fig. 8. The respective lattice constants can be converted using simple geometrical considerations, which are summarized in the appendix B.1.

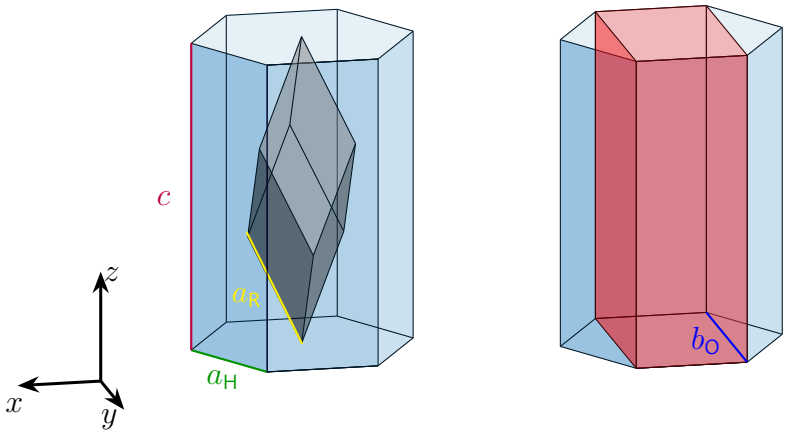

Figure 8: Schematic representation of the different portrayals of the trigonal unit cell: primitive rhombohedral (black), hexagonal (blue), and orthorhombic (red). The lattice constants a_H, a_R, b_O, and c are labeled in green, yellow, blue, and purple, respectively.

Within the crystal, the oxygen ions form octahedral cages around the lithium and niobium/tantalum ions. These oxygen cages are stacked on top of each other along the z-axis. Within the cages, a chain of periodically aligned lithium- and niobium/tantalum ions is formed, such that each octahedron holds either a lithium ion, a niobium/tantalum ion, or no ion. This chain is centered with respect to the xy plane of the octahedra. Within the paraelectric configuration, each lithium ion lies directly within an oxygen plane and each niobium/tantalum ion is centered between two oxy-

gen planes[20]. This high symmetry arrangement is broken in the ferroelectric phase, where both the lithium and niobium/tantalum ions are displaced along the z-direction, leading to a spontaneous polarization along the same direction. The ionic structure for both phases is schematically shown in Fig. 9.

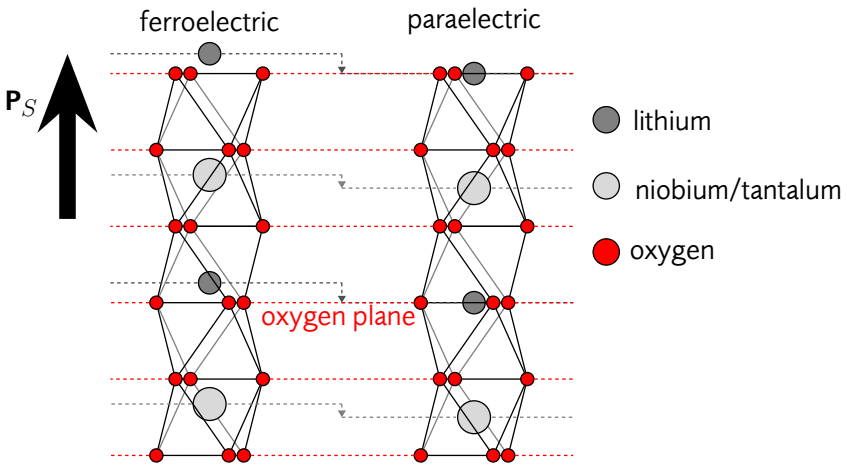

Figure 9: Schematic representation of the ferroelectric (lhs) and paraelectric (rhs) phase of LN and LT

In total, the structure exhibits three mirror planes, which are all parallel to the z-direction. Additionally, the paraelectric phase features an inversion center. All symmetries need to be considered in order to correctly interpret results. Further, each symmetry corresponds to a significant numerical simplification.

3.2 Thermal Expansion

A devices functionality highly depends on accurate maintenance of the physical properties of the underlying constituent materials. This is especially crucial when considering the operation temperature of the device: Most materials expand in size when heated up, which affects almost all of its properties. A change of the lattice constants implies changes in atomic bonding length and strength, which has a direct impact on the elastic properties of the material. The implied structural changes also influence the electronic properties by modifying the ionic background potential. Different materials show different magnitudes of thermal expansion, possibly inducing strain within a composite device, and consequently limiting its application. Thus, accurate knowledge of the thermal expansion is a crucial first step in order to determine temperature-dependent properties of a material.
In DFT simulations, it is important to fix the geometry of the unit cell in order to minimize numerical noise. Else, an additional error called *Pulay stress* is introduced, since the plane-wave basis set changes with respect to the lattice vectors, resulting not only in erroneous stresses, but also leading to errors in the calculated energies [45].

[20]The high-symmetry arrangement might only describe a temporal average over the whole crystal, as implicated by molecular dynamics calculations [P6].

For accurate simulations of temperature effects it is thus necessary to determine the lattice expansion of the crystal as a function of temperature. For consecutive calculations, every temperature corresponds to a different set of fixed lattice vectors. In practice, not all lattice vectors are determined independently, since the resulting computational demand is quite large[21]. Instead, the unit cell volume is kept fixed as a first approximation which reduces the degrees of freedom to a manageable amount. Further, the *Pulay stress* behaves almost uniformly in all directions [W11], justifying this isotropic approach.
To obtain the unit cell volume as a function of temperature, the QHA as implemented in phonopy [46, 47] is employed and the procedure outlined in Ref. [48] is followed: Harmonic phonon frequencies are calculated using the finite differences method with $3\times3\times3$ supercells at different volumina. Using the Parlinski-Li-Kawazoe method to interpolate the phonon frequencies to arbitrary **q**-points [49], the harmonic phonon frequencies are obtained on a $20\times20\times20$ mesh. From this phononic density of states (DOS), the phononic free energy can be extracted using Eq. (2.46). This yields phononic free energies converged within 1 meV with respect to a twice as dense **q**-point mesh. These frequencies and volumina are then used to calculate the Gibbs energy at different temperatures (assuming no internal pressure):

$$G(T) = \min_V \left[U_{\text{el}}(V) + F_{\text{phon}}(T;V)\right]. \tag{3.1}$$

Fitting the Gibbs energy via the Murnaghan equation of state, the equilibrium volumina as a function of temperature can be extracted. This is shown for exemplary temperatures in figure 10.
The outlined procedure is utilized up to rather high temperatures. It is therefore not reasonable to assume the validity of the harmonic approximation. Furthermore, the harmonic phonon frequency spectrum of the paraelectric phases contain imaginary modes [50, 51]. For LT, these imaginary frequencies are ignored in the calculations of the phononic DOS. For LN, the same procedure does not yield reliable data, since the phase transition to the ferroelectric phase occurs at a far higher temperature than for LT ($T_C \approx 880$ K for LT and $T_C \approx 1400$ K for LT), such that anharmonic effects play a dominant role in the paraelectric phase of LN. However, an approach beyond the harmonic estimate of the phonon frequencies is computationally not feasible here, and thus the paraelectric phase of LN is not considered within this section.
The calculated volumetric data (red lines in Fig. 10) are in good agreement with the measured thermal expansion of LN and LT [14, 18]. The calculated volumes slightly overestimate the measured values in both materials by around 2 %, as known from GGA based exchange-correlation functionals. The deviations might also be related to the stoichiometry of the measured samples or by anharmonic contributions disregarded in the QHA. A closer look at the individual lattice constants is given in Sec. 3.5.1.
From the calculated phononic DOS at different volumina, the specific heat capacity at constant pressure can be calculated using the formulation given in the Appendix A.1. The resulting curves are shown in Fig. 11.

[21] The full thermal lattice expansion is performed using force fields in Sec. 3.5.1.

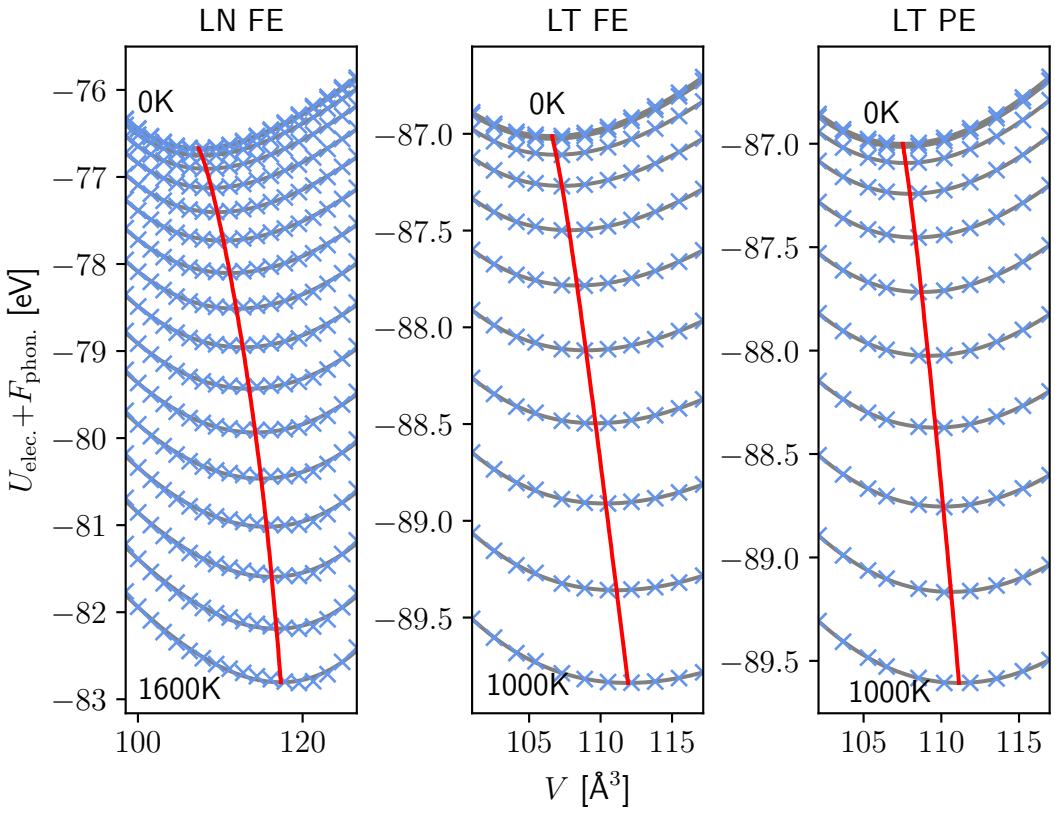

Figure 10: Gibbs free energy vs. unit cell volume. For each temperature, the data points are fitted via the murnaghan equation of state (grey). The minima (red line) denote the equilibrium volumina. The fits are performed for the ferroelectric phases of LN (left) and LT (middle), and for the paraelectric phase of LT (right).

An overall good agreement to experimental measurements can be found for the ferroelectric phases for both, LN and LT, with an error of only about 5 % [52–56, P9]. These deviations might be a consequence of the overestimation of the lattice volume, but could again be attributed to further anharmonic phonon corrections or the stoichiometry of the measured samples. For the paraelectric phase of LT, the experimental values are not well reproduced, and cannot describe the measured increase of c_p at high temperatures. Here, it is obvious that the harmonic phonon approximation fails, since the paraelectric configuration does not describe a ground state of the system. Still, the observed drop of the c_p value after the phase transition is well reproduced [P9], even though the Curie temperature itself cannot be extracted from the calculations here. Its determination will be discussed in the following section.

3.3 Ferroelectric Phase Transition

The Curie temperature can be calculated by comparing the free energies (or rather, Gibbs energies, but the internal pressure is assumed to be vanishingly small) of both, the ferro- and paraelectric phases. The contributing terms are the electronic and

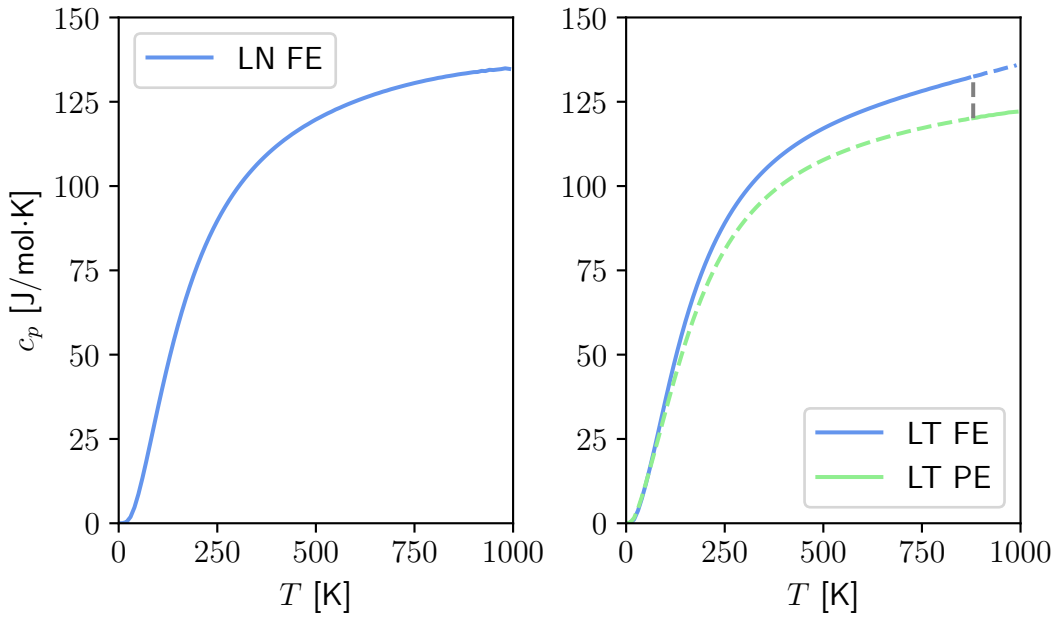

Figure 11: Specific heat capacity at constant pressure calculated for LN (left) and LT (right). The grey line indicates the experimentally determined Curie temperature at 880 K [P9]. The colored dashed lines denote unstable regions for the ferro-and paraelectric phases.

phononic energies. The latter are typically calculated within the harmonic approximation. However, the presence of imaginary modes in the paraelectric structures does not allow for accurate energies, resulting in imprecise values for the Curie temperature [50]. As a first correction, the volumetric expansion with increasing temperature can be taken into account, which has been calculated in the previous section. Not only does this assumption lead to more precise electronic energies (since they depend on the ionic background and therefore on the cell volume), but it also includes corrections for the phononic energies. Yet, the extracted Curie temperatures do not well describe experimental findings (1413-1475 K for LN [57, 58], and 874-958 K for LT [14, 17]). Thus, an approach beyond the quasi-harmonic approximation is necessary.

Within the SSCHA, the crystal geometry relaxation is perfomed on the free energy landscape, by optimizing the free energy with respect to all degrees of freedom of the crystal structure [59]. Thus, the full Born-Oppenheimer energy surface, as well as its derivatives with respect to the ionic positions (accounting for interatomic forces) and cell parameters (yielding the stress tensor) need to be calculated on a quantum-mechanical level. To minimize the computational effort needed, a stochastic algorithm as implented in *python-sscha* [39, 59–62] is utilized. The underlying formalism is described in detail in Ref. [59], and the nomenclature established therein is used here.

First, the free energy landscape is sampled by creating a set of random ionic displacements in a within the QHA optimized supercell, using a Gaussian probability distribu-

tion[22]. For each of these structures, the electronic energies, forces, and stresses need to be calculated with high accuracy. Hence, the chosen supercell size is downscaled to $2\times2\times2$ to save computational costs. All considered temperatures are treated separately, using the volumina provided by the QHA calculations from the previous section. For the paraelectric phase of LN, the same lattice volume as for its ferroelectric phase is assumed.
In total, up to 400 structures per ensemble need to be created to accurately sample the free energy surface for the paraelectric phases. For the ferroelectric phases, the reduced number of symmetries requires a larger sample size. Up to 2000 structures are considered for these phases. For each such created ensemble, the free energy minimum of the currently sampled part of the whole free energy surface is determined, and, if the gradients at this determined minimum are not vanishingly small, another ensemble based on the currently minimal energy position is created. For each step of the minimization algorithm, the current effective sample size (i.e. how many sampled datapoints are in vincinity to the current minimum) is calculated. If this effective sample size, given by the so called Kong-Liu ratio, is below 80 % of the total sample size, the minimization is stopped and the next ensemble is created. An exemplary plot of the most important parameters during the runtime of the algorithm is shown in Fig. 12. On average, four ensembles are needed in order to find the free energy minimum. Lastly, another ensemble is created to calculate the anhamornic phonon frequencies. Since the derivatives of the free energy surface are needed for this calculation, this last ensemble includes up to 10000 structures, which enables to calculate the phonon frequencies with a precision of around 5 cm^{-1}, compared to a twice as large ensemble size. The so called *bubble-approximation* (i.e. neglecting $\overset{(4)}{\phi}$ in Eq. (2.42) see Ref. [59]) is assumed, since its first order correction (referred to as *v4*, the full equation (2.42)) does not effect the phonon frequencies within the determined accuracy. The phonon frequencies are again interpolated onto a $20\times20\times20$ mesh. Exemplarily, the harmonic and anharmonic phonon dispersions of paraelectric LT at 1000 K are shown in Fig. 13. Clearly, the within the harmonic approximation present imaginary frequencies are now correctly described, and the phase is stable (or at least metastable) at this temperature.
From these calculations, the total energy of the structure can be determined: The electronic energy is taken as the stochastic average over the last ensemble, by weighting the electronic energy of each structure according to the set temperature and the dynamical matrix. The resulting stochastic uncertainty is below 1 meV. The phononic free energies are again calculated from the (anharmonic) phononic DOS using
Eq. (2.46), i.e. the phonons are assumed to behave harmonically in this final calculation.
All the above steps are carried out for the ferro-and paraelectric phases of LN and LT for selected temperatures near their respective experimentally observed transition temperature. The results are shown in Fig. 14. The Curie temperature can be extracted as the intersection between the total free energies of the ferro- and para-

[22] This is different from an atomisitic data set collected during a molecular dynamics run, since energetically unfavorable configurations are equally included here.

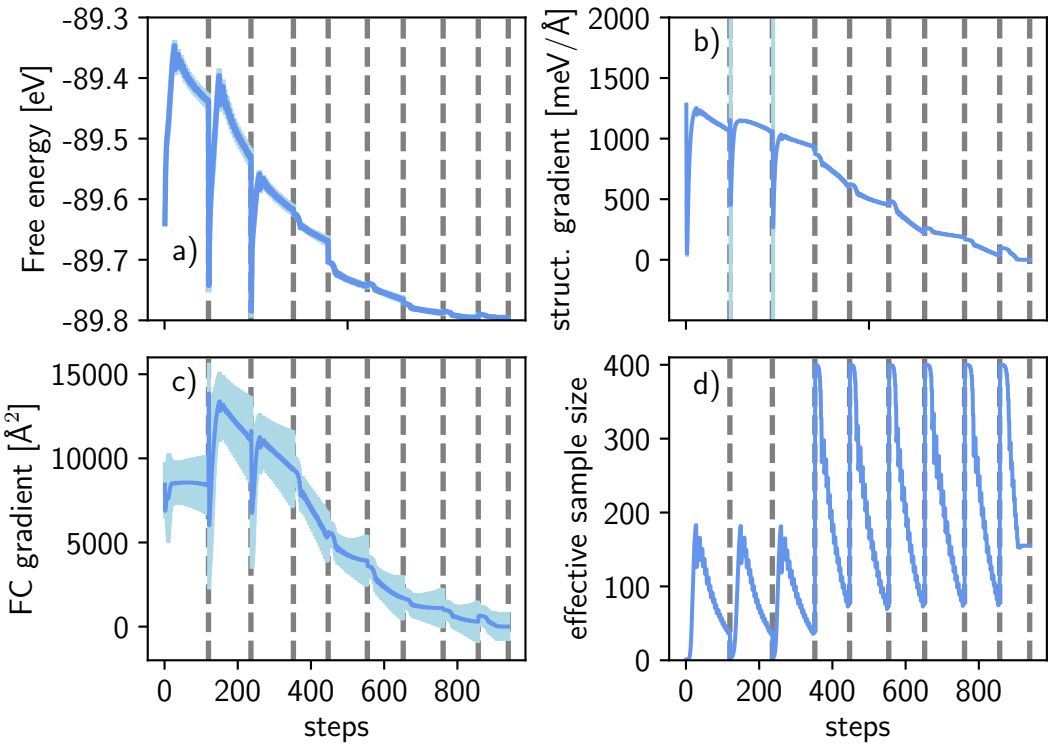

Figure 12: Parameters of the SSCHA run during the minimization algorithm: For each step taken along the free energy surface, the effective sample size (Kong-Liu ratio, lower right panel) decreases. If this value falls below a threshold of 20 % of the initial number of configurations, a new ensemble is created (dashed vertical lines), and the effective sample size increases to the number of configurations used. The minimization is stopped if the gradients of the free energy, i.e. the forces (upper right panel) and stresses (lower left panel), reach zero, while the effective sample size is larger than 50 %. The total free energy per unit cell (upper left panel) converges to its minimal value. The stochastic error at each step is denoted in turquoise.

electric phases. These intersections occur at 1408 K for LN and 808 K for LT. Contrary to previous calculations, these values are in good agreement to the experimental findings of around 1413 K and 874 K for LN and LT, respectively [14, 17, 57], which demonstrates the importance of anharmonic effects.

Since the SSCHA also provides the ionic equilibirum positions at each temperature, the nature of the phase transition can be observed. Here, both the Li- and Nb/Ta ions continuously move towards their high-symmetry, paraelectric positions with increasing temperature, implying a displacive type transition for both ion types. This is seemingly in contrast to findings from molecular dynamics runs, where the Li ions are stochastically distributed both parallel and anti-parallel with respect to the spontaneous polarization direction at each time step [P6]. However, a similar effect would result from the ionic oscillations around their equilibirum positions, such that no clear answer regarding the nature of the phase transition can be given here. The Nb and Ta ions are much heavier compared to the Li ions, and therefore show smaller oscil-

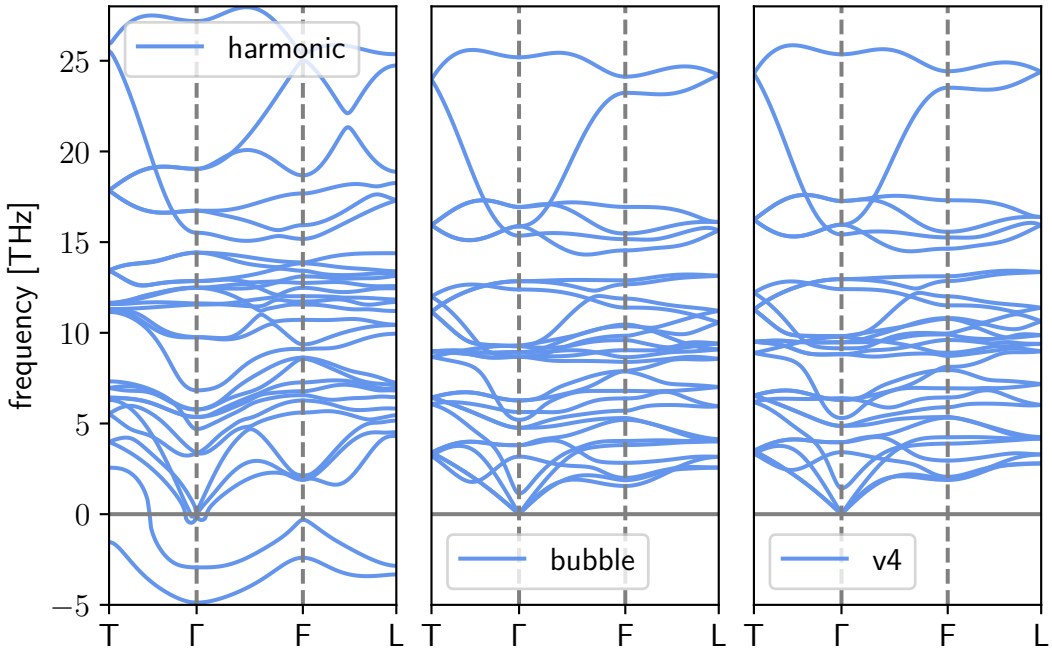

Figure 13: Phonon dispersion of paraelectric LT at 1000 K, calculated using the harmonic approximation (left), the anharmonic bubble approximation (middle), and its first correction term (v4, right). Imaginary phonon frequencies are plotted as negative values.

lations in the molecular dynamics calculations. Thus, they are localized around their paraelectric equilibirum position within the center of the O cages, which is confirmed by the SSCHA calculations.

3.4 Thermal Transport

Knowledge of the thermal conductivity is crucial for a number of applications. For example, a low thermal conductivity enables to efficiently transfer heat to electricity in energy conversion materials [63]. On the other hand, a high thermal conductivity is desired for high-power laser applications, to transfer excess heat and supress overheating of the device [64].

Simulating thermal transport fully quantum-mechanically is numerically challenging, since the interaction between phonons needs to be considered (e.g. by calculating the third-order force constants). Since the SSCHA routine provides all necessary quantities needed to calculate the lattice thermal conductivity using the Boltzmann Transport Equation in the Relaxation Time Approximation Eq. (2.51), it is comparatively straightforward to compute at each temperature considered in the SSCHA calculations. Consequently, volumetric expansion is implicitly taken into account here (since it is present within the SSCHA simulations). A scattering grid of $20\times20\times20$ $\mathbf{q}$-points is needed in order to achieve a convergence of the lattice thermal conductivity

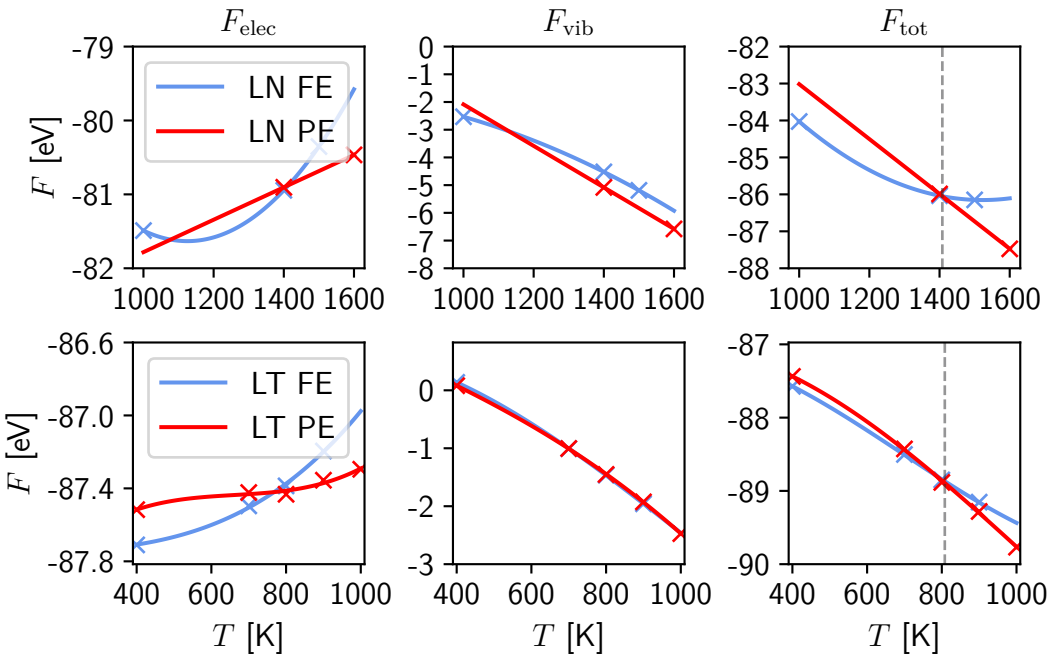

Figure 14: Free energy per unit cell of LN (upper panel) and LT (lower panel). The contributions of the electronic term (left), phononic term (middle), and the total free energy (right) are shown. The engeries of the ferro- and paraelectric phases are denoted as blue and red, respectively. The Curie temperature can be extracted as the intersection of both curves in the total free energy (dashed vertical line).

within 7 mW m^{-1} K^{-1}. The datapoints are fitted analogously to Refs. [65, 66] using

$$\kappa(T) = a + \frac{b}{T} + \frac{c}{T^2}. \tag{3.2}$$

The results are presented in Fig. 15. For both, LN and LT, the lattice thermal conductivity is anisotropic, and larger along the polar crystal axis. With an increase in temperature, the lattice thermal conductivity decreases. The paraelectric phases feature a larger lattice thermal conductivity, which is thus expected to rise when heating up to the Curie temperature. Lithium tantalate has an overall larger lattice thermal conductivity than lithium niobate. The origins of the latter behavior has been discussed in detail by Fu *et al.* [64], and is traced back to the different Grüneisen parameters of the two materials.
In experimental studies, the here predicted increase at the Curie temperature could be observed in LT, alas, only as a single peak and not as a step-like increase [65]. Compared to previous simulation of the lattice thermal conductivity where thermal expansion effects were not considered, the calculated values for LT are much larger within the simulated temperature region [64]. These values were underestimated compared to experimental studies [65, W17]. Hence it can be concluded that the inclusion of thermal expansion effects overcorrects the results. This emphasizes the importance of physical effects not considered in the calculations, e.g. electron-phonon

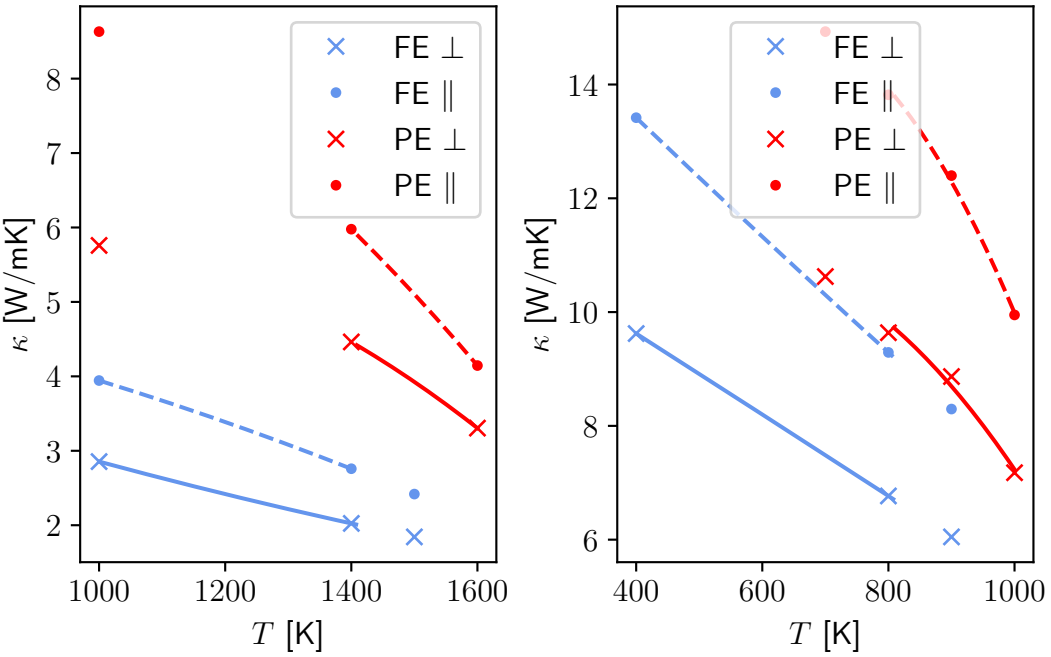

Figure 15: Lattice thermal conductivity as a function of temperature for LN (left) and LT (right). The ferro- and paraelectric phases are denoted in blue and red, respectively. The crosses (dots) denote datapoints for the conductivity perpendicular (parallel) to the polarization axis. The fits are obtained using equation (3.2).

coupling. Again, the stoichiometry of the measured samples might significantly influence the results as well. For LN, no high temperature values are available to compare within literature, but an overall overestimation of the thermal conductivity is again expected from extrapolating the simulated values from Fu *et al.* [64], and comparing with available experimental values [65, W17].

This discrepancy compared to previous simulations can be further analyzed by looking at the phonon lifetimes: Only those phonons with long lifetimes (i.e. $\tau > 5$ ps) and a large group velocity can contribute significantly to the lattice thermal conductivity (see Eq. (2.51)). The lifetimes of the phonons are shown in Fig. 16 for different temperatures.

Clearly, low frequency phonons exhibit long lifetimes, for both LN and LT. As expected, the lifetime decreases with an increase in temperature. However, some notable exceptions can clearly be distinguished, showing high-frequency phonon modes with rather long lifetimes (e.g. at around 10 THz for ferroelectric LN). Since these modes cannot be observed in Ref. [64], it can be assumed that they yield a huge contribution to the overall larger thermal conductivity compared to this reference. However, it can not be determined whether these modes have such a long lifetime because of physical effects (such as thermal expansion), or if the simulation constraints yield numerical noise (e.g. regarding the approximated hydrostatic expansion considered in the SSCHA).

Some notable differences in phonon lifetimes can be observed between the ferro-

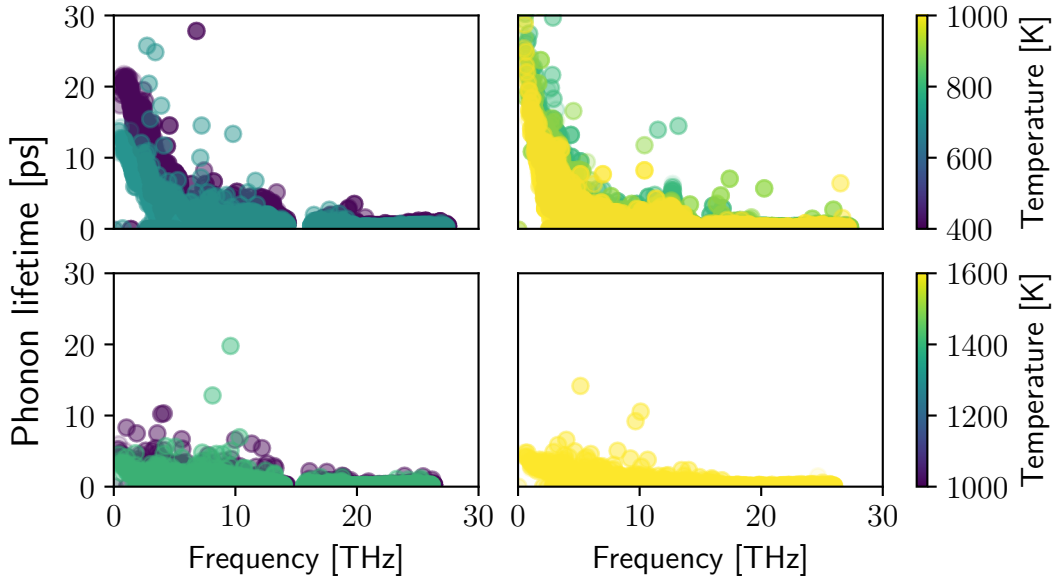

Figure 16: Phonon lifetimes as a function of frequency for LT (upper panel) and LN (lower panel). Both the ferroelectric (left) and paraelectric (right) phases are considered. The temperature is overlayed as a color code.

and paraelectric phases: Despite the increased temperature, the paraelectric phases feature overall similar phonon lifetimes as the ferroelectric phases. For LT, the lifetimes even increase, especially for the low- and some high-frequency modes. This increase in phonon lifetimes contributes the most to the increase in heat conductivity of the paraelectric phase, since both the specific heat capacity at constant volume, as well as the group velocities (shwon in Fig. 17) only show minor deviations between the two phases[23].
Regarding the group velocities, the phonon branches with the largest group velocity (i.e. dispersion, compare e.g. with Fig. 13) can clearly be identified as the low frequency acoustic branches, as well as the two highest frequency branches (along the ordinary and extraordinary axes each). The increase in temperature (which is only included as the increase in cell volume) yields an overall shift of the phonon frequencies to lower values. A more detailed analysis of these frequency shifts can be found in Ref. [67], as well as in chapter 3.5.1.

3.5 Application of Machine-Learned Force Fields

Even though the previous sections feature an impressive agreement to experimental data by using the DFT as a base formalism, they also highlight the substantial numerical costs needed in order to obtain results. Hence, the usage of DFT significantly limits the range of within a reasonable timeframe feasable simulations. Instead, the application of force fields provides a computationally much more efficient scheme. However,

[23] The specific heat capacity at constant pressure features a clear decrease at the phase transition, as has been shown in Fig. 11

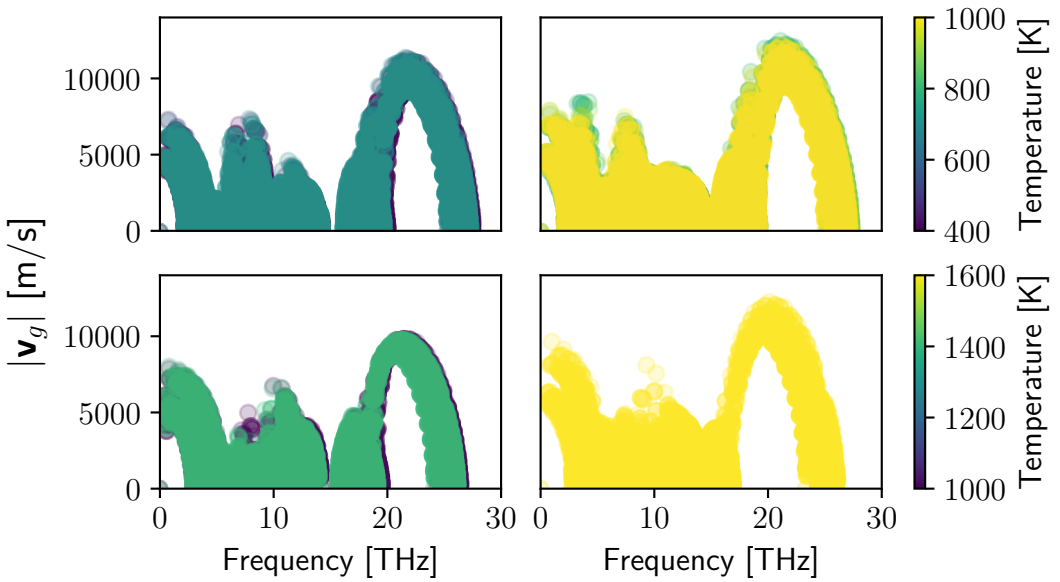

Figure 17: Phonon group velocities (absolute values) as a function of frequency for LT (upper panel) and LN (lower panel). Both the ferroelectric (left) and paraelectric (right) phases are considered. The temperature is overlayed as a color code.

most common force fields are only valid within certain chemical environments (i.e. a force fields that well describes lithium oxide Li_2O and niobium oxide Nb_2O_5 might not be reliable for lithium niobate), limiting the accuracy of the results. The idea of using machine-learned force fields circumvents both constraints: First, the chemical environments of interest can explicitly be used as part of the training dataset. The machine-learned force fields are thus not limited to specific atomistic configurations, but can ideally cover all structures provided during the training. Second, the accuracy of such a machine-learned force field is mainly given by the accuracy of the training data themselves, as well as of the overall coverage of the production calculations by the training dataset. An accuracy of almost DFT level can (in principle) be achieved by providing a within DFT calculated training dataset spanning the entire range of configurations used during the production run.

The previously utilized SSCHA calculations provide such a training dataset for calculating phononic properties at different temperatures (i.e. different bonding lengths) for both, LN and LT: Only the force constants and electronic energies at different bonding lengths (which not only provide the thermal expansion effect at different temperatures, but can also be used to simulate strain) need to be computable by the force field. The random displacements of the ions from their respective equilibrium positions within the SSCHA provide an excellent environment for fitting the force constants for different atomic distances.

The training dataset for both, LN and LT, consist of 8.000 structures each. These structures are extracted from the last SSCHA ensemble at four different temperatures each, such that 2.000 structures for each temperature (i.e. lattice volume) are being considered. Since these last ensembles consist of in total 10.000 structures each,

the 2.000 training set structures are randomly chosen, while the remaining structures form a validation dataset. Only the ferroelectric phases are considered. The training, and all subsequent calculations, are performed using the algorithms provided within VASP. The numerical values of the cutoff radii needed for the correlation functions are determined to be $r_{\text{max}} = 9$ Å and $s_{\text{max}} = 6$ Å (see Sec. B.2.3 in the Appendix). The accuracy of the extracted force fields are finally examined by providing three different errors: The training set error yields the average error of quantities calculated from the force field compared to the "exact" values provided by the respective training set structure. The validation set error is similarily defined, but the average errors are calculated from the structures within the validation dataset. Since these structures were not explicitly used during the training, the validation set error provides an extrapolation of the training data, and is thus typically slightly larger compared to the training set error. Finally, a test set needs to be created in order to determine the to be expected production run error. Here, this test set is chosen to be a relatively small set of 600 structures that are explicitly needed for subsequent simulations. In detail, the test set consists of 30 phonon calculations using the finite difference method in 3×3×3 supercells at different lattice vector lengths[24]. Hence, the test set error provides the best estimate on how well the trained force fields perform for the subsequent tasks, compared to DFT calculations. All errors are shown for both, LN and LT in Tab. 1.

		elec. energy [eV/atom]	forces [eV/Å]
LN	Training	7.37e-4	6.71e-2
	Validation	7.40e-4	6.78e-2
	Test	7.08e-3	2.12e-1
LT	Training	5.71e-7	5.18e-2
	Validation	5.53e-06	5.24e-2
	Test	1.24e-2	1.16e-1

Table 1: Predicted accuracy of the machine learned force fields.

The average error of the electronic energy is well within the numerical accuracy of the DFT calculations, which has been determined to be at around 1 meV per atom. The error of the averaged forces (root mean square error) is also reasonably small, considering that different potentials yield differences of up to 0.1 eV Å^{-1}. Overall, the predicted errors compared to DFT calculations are sufficiently small to allow for an application of these force fields.

3.5.1 Anisotropic Thermal Expansion

Utilizing the machine-learned force fields instead of DFT, the same procedure as in Sec. 3.2 is used to calculate the thermal expansion within the QHA. However, due to the numerical simplification, both lattice constants can now be varied separately,

[24] The QHA calculations in sec. 3.2 are perfomed by varying the volume, and not explicitly both lattice constants separately. Hence, the previous results do not form an adequate test set.

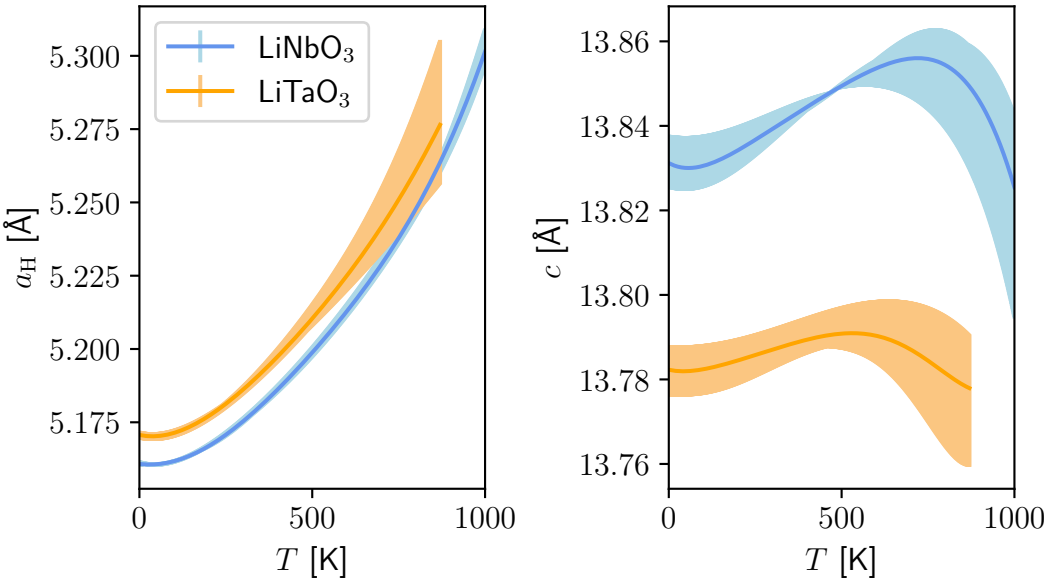

Figure 18: Lattice constants as a function of temperature as calculated within the QHA using machine-learned force fields. The error bars denote the maximal deviations when using different force fields. The average values are plotted as a solid line.

instead of a volumetric, hydrostatic approximation. The free energy is thus not calculated as a function of volume (and temperature), but explicitly as a function of both lattice constants, a_H and c. In place of the Murnaghan equation of state, which only holds for hydrostatic variation of the lattice, a polynomial of third order is used for the fit. Thus, the lattice constants as well as their corresponding thermal expansion coefficients can be extracted as a function of temperature.

Since the previously estimated errors of the force fields do not contain explicit errors of the resulting lattice constants, two additional force fields are trained for LT, and one additional for LN: Instead of generating an entirely new training set, the previously used training and validation set data are shuffled, and randomly assigned as the new training structures. All other fitting parameters remain unchanged. As a result, the estimated average errors of the ionic forces and electronic energies remain almost unchanged. Still, these additional steps provide a further verification of the following results by partially taking stochastic errors into account.

The simulation grid is chosen to be in the range of 5.1-5.35 Å (5.1-5.4 Å) for the in-plane, hexagonal lattice constant, and 13.75-13.95 Å (13.6-13.85 Å) for the height of the hexagonal unit cell for LN (LT). The temperature is sampled in steps of 10 K, starting from 0 K up to 1000 K and 800 K for LN and LT, respectively. The obtained equilibrium lattice constants (at the free energy minima) are then fitted using a high order polynomial. The resulting lattice constants as a function of temperature are shown in Fig. 18.

The in-plane lattice constants of LN and LT, and their thermal behavior, are very similar, and a slight deviation from linearity can be observed. These similarities can be traced back to the almost identical atomic radii of Nb and Ta, with almost identical onto

the basal plane projected bonding lengths. Compared to experimental data [18], the lattice constants are slightly larger, which is to be expected for the force field, since it has been trained on DFT data that used the PBEsol functional. The (linear) thermal expansion coefficient itself is, however, in good agreement, with an average simulated value of 0.107 mÅ K^{-1} compared to the measured value of 0.11 mÅ K^{-1} [18].
The lattice constant c shows a distinctly different behavior: For one, the lattice constant for LN is larger compared to LT over the whole temperature range. Looking at the bonding lengths projected onto the z-axis, a shorter Ta-O bond compared to Nb-O can explain this difference (see Sec. 4.2 for a closer look). Qualitatively, the different lengths of the lattice constants in LN and LT have been observed in experiments [18], however, with a larger magnitude than in the simulations. The lattice constant first increases with an increase in temperature, with a much larger expansion for LN compared to LT. But at 830 K (600 K), the lattice constant suddenly shows a sharp decrease for LN (LT). Again, this compliments the measured trend from Ref. [18], where the lattice constant for LT finally increases again after passing the Curie temperature.
This unusual behavior can be qualitatively explained by looking at the phononic frequencies with respect to the lattice constants: In most cases, the phonon frequencies will decrease with an increase in lattice constants, since bonds are elongated and therefore weakened. This can be nicely observed by plotting the derivative of the phonon frequencies at the Γ point with respect to a change in the lattice constant a_{H}, which is exemplarily shown for LN on the right-hand side of figure 19. Contrary, some exceptions can be observed if instead the variation of the lattice constant c is chosen, which is demonstrated on the left-hand side of figure 19: Here, some phononic modes increase in frequency with respect to an increasing lattice constant c. This increase is especially large for the A_1-TO_4 symmetry mode, whereas the low-frequency A_1-TO_1 and E-TO_2 modes (refer to Sec. 4.6 for the naming convention) show a much weaker dependence of the hexagonal height c. Hence, these three modes energetically favor a thermal contraction, rather than an expansion. The same considerations also hold for LT. This behavior is confirmed in Ref. [67], where the phonon frequencies were tracked as a function of applied strains, within both, experiment and DFT simulations. The contribution of these modes to the thermal expansion can be estimated by their respective Grüneisen parameters [68, 69]:

$$\gamma_{ij}^{m} = -\frac{1}{\omega_m}\frac{\partial \omega_m}{\eta_{ij}}, \tag{3.3}$$

where η_{ij} denotes a component of the strain tensor acting on the unit cell, and ω_m the frequency of mode m. Since the E-TO_2 modes frequency features a much smaller derivative with respect to the lattice constant c (i.e. a strain in z-direction) compared to the two A_1-TO modes (by an order of magnitude), it will be omitted in the following discussion. Both these A_1-TO modes yield similar Grüneisen parameters, as their difference in absolute frequency values almost cancels their different dependence on the lattice constant. Since the A_1-TO_4 mode represents one of the highest frequency modes within LN and LT, its thermal activation can only take place at elevated temperatures. Hence, its contracting effect on the lattice along the z-direction can only

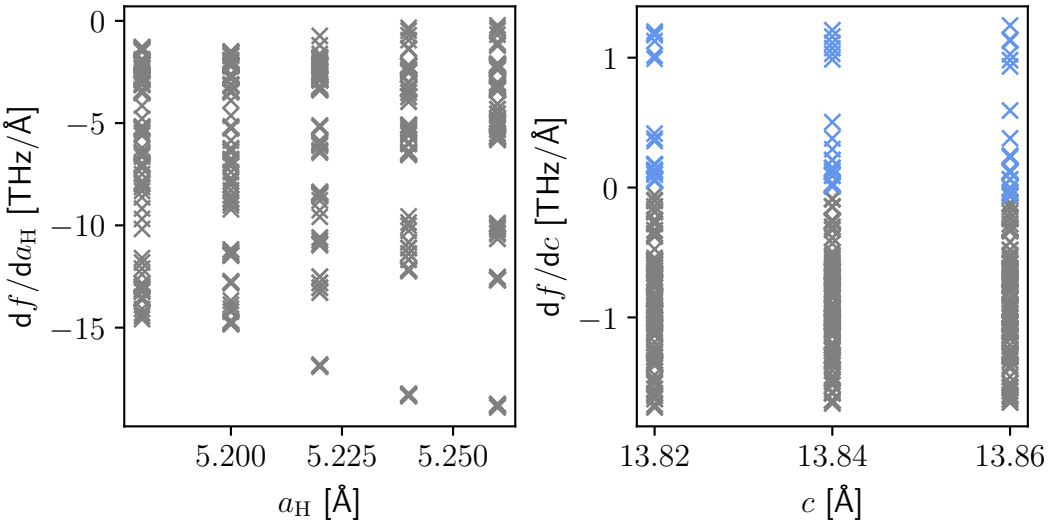

Figure 19: Change of the phonon frequencies of LN at Γ with respect to the lattice constants: The derivative with respect to the basal lattice constant a_H (right), and c (left), are shown as a function of the same lattice constant. All 30 phonons are considered, within a grid spanned by both lattice constants. Only the projection along the derived lattice constant is shown. Blue points denote phonons that energetically favor a contraction along the respective lattice constant (i.e. the derivative is larger than zero at some value of the investigated lattice constant), whereas grey points favor an expansion.

occur at such higher temperatures, whereas in the lower temperature regime where the A_1-TO_4 mode is not yet activated, the lattice expands instead. Since the phononic frequencies of all of the modes leading to this contraction is higher in LN than in LT (see e.g. Figs. 51 and 52 in the appendix), their thermal activation takes place for higher temperatures in LN. Consequently, the bowing of the lattice constant c can already be observed at lower tempratures in LT, and only at higher temperatures in LN.

Qualitatively, the phonon frequencies change more drastically with respect to an expansion along the basal plane, which aligns with the overall much larger thermal expansion along this direction compared to the height of the hexagonal cell.

Finally, comparing the simulations here to the hydrostatic approximation made in chapter 3.2 reveals some distinct shortcomings of the latter: First, the anisotropy of the material can obviously not be taken into account by the hydrostatic approach. This is especially striking for highly anisotropic materials, as LN and LT, with very distinct thermal behaviors of the different lattice constants. Further, the Murnaghan equation of state overestimates the unit cell volume by as much as 4 %, compared to the anisotropic approximation, which in turn still overestimates the volume compared to experimental measurements. The latter can be traced back to the inherent overestimation of lattice volumina by the PBEsol functional. The former, however, is a distinct result of the assumption of isotropy.

3.5.2 Elastic Moduli

The elastic moduli of a material define its mechanical stiffness with respect to deformations. For anisotropic materials such as LN and LT, the elasticity is given via a tensor. Knowledge of this elastic tensor is especially crucial for piezoelectric materials, because the interplay between the elastic- and piezoelectric tensors determines the magnitude of the piezoelectric effect. Since the lattice constants change non-linearily with temperature, a complex temperature behavior of the elastic tensor is to be expected, as mainly the atomic bond lengths determine a material's stiffness. Thus, the elastic tensor as a function of temperature will yield valuable insights, specifically for high-temperature applications. The machine-learned force fields provide a unique opportunity here: Since they were explicitly trained for different interatomic bond lengths, the elastic constants are readily available within a high accuracy. Indeed, the following simulations would not have been numerically feasible using purely DFT. In this section, all independent components of the elastic tensor are calculated, including thermal expansion and harmonic phonon effects.

Unfortunately, the unit cell orientation convention outlined in Ref. [7] does not uniquely define the elastic tensor: A rotation of 180° around the polarization axis switches the sign of the components C_{14} and C_{24} (and C_{41} and C_{42}, accordingly) [67,70], while still satisfying the established convention. Here, the unit cell is rotated such that one rhombohedral lattice vector a'_{R} lies perpendicular to the x-axis, and $\langle y|a'_{\mathrm{R}}\rangle > 0$. The elasticity tensor of LN and LT is written as

$$C_{ab} = \begin{pmatrix} C_{11} & C_{12} & C_{13} & C_{14} & 0 & 0 \\ C_{12} & C_{11} & C_{13} & -C_{14} & 0 & 0 \\ C_{13} & C_{13} & C_{33} & 0 & 0 & 0 \\ C_{14} & -C_{14} & 0 & C_{44} & 0 & 0 \\ 0 & 0 & 0 & 0 & C_{44} & C_{14} \\ 0 & 0 & 0 & 0 & C_{14} & \frac{1}{2}(C_{11} - C_{12}) \end{pmatrix}.$$

In total, six independent entries need to be calculated. By applying different strains on the optimized unit cell at a given temperature, all components can be calculated. The applied strain tensors in Voigt notation read explicitly as

$$\eta_1 = \begin{pmatrix} \eta \\ \eta \\ 0 \\ 0 \\ 0 \\ 0 \end{pmatrix}, \eta_2 = \begin{pmatrix} 0 \\ 0 \\ \eta \\ 0 \\ 0 \\ 0 \end{pmatrix}, \eta_3 = \begin{pmatrix} \eta \\ \eta \\ \eta \\ 0 \\ 0 \\ 0 \end{pmatrix}, \eta_4 = \begin{pmatrix} 0 \\ \eta \\ 0 \\ 0 \\ 0 \\ 0 \end{pmatrix}, \eta_5 = \begin{pmatrix} \eta \\ \eta \\ 0 \\ 0 \\ -\eta \\ \eta \end{pmatrix}, \eta_6 = \begin{pmatrix} \eta \\ \eta \\ 0 \\ -\eta \\ -\eta \\ 0 \end{pmatrix}.$$

According to the energy-strain relation given in Eq. 2.60, the free energy calculated for the strained structures relates to the elastic components as:

$$
\begin{aligned}
\frac{F_1}{V_0} &= \frac{1}{2}\left(2C_{11}+2C_{12}\right)\eta^2, & C_{11} &= \frac{2}{V_0\eta^2}F_4\\
\frac{F_2}{V_0} &= \frac{1}{2}C_{33}\eta^2, & C_{12} &= \frac{1}{V_0\eta^2}\left(F_1-2F_4\right)\\
\frac{F_3}{V_0} &= \frac{1}{2}\left(2C_{11}+2C_{12}+C_{33}+4C_{13}\right)\eta^2, & C_{33} &= \frac{2}{V_0\eta^2}F_2\\
\frac{F_4}{V_0} &= \frac{1}{2}C_{11}\eta^2, & C_{13} &= \frac{1}{2V_0\eta^2}\left(F_3-F_1-F_2\right)\\
\frac{F_5}{V_0} &= \frac{1}{2}\left(\frac{5}{2}C_{11}+\frac{3}{2}C_{12}+C_{44}-2C_{14}\right)\eta^2, & C_{44} &= \frac{1}{V_0\eta^2}\left(F_6-F_1\right)\\
\frac{F_6}{V_0} &= \frac{1}{2}\left(2C_{11}+2C_{12}+2C_{44}\right)\eta^2, & C_{14} &= \frac{1}{V_0\eta^2}\left(\frac{1}{4}F_1+F_4+\frac{1}{2}F_6-F_5\right)
\end{aligned}
$$

The energies F_1, F_2, and F_3 can be extracted from the calculations of the previous section: At each constant temperature, the energy surface as a function of the lattice constants c and a_H has been explicitly calculated. Following specific paths intersecting the minimum (i.e. the equilibrium cell) is equivalent to applying a specific strain tensor on the equilibirum cell. For example, the path parallel to the c-axis intersecting the minimum is equivalent to straining the unit cell in cartesian z-direction. The three paths corresponding to the strain tensors η_1, η_2, and η_3 are exemplarily shown in Fig. 47 in the Appendix. The strain tensor η_4, and the (partial) shear strains η_5 and η_6 need to be explicitly calculated: For each temperature (i.e. lattice constants), the strain tensor is applied using different strains η, ranging from –1 % to 1 %. The free energies are again calculated using the electronic and phononic energies, in the same manner as in the previous section, and finally fitted with a polynomial of the form

$$F(T,\eta) = a\eta^2 + b\eta^3, \tag{3.4}$$

such that the coefficient a relates to the components of the elasticity tensor. Exemplarily, the energy strain curve for η_5 at 300 K for LT is shown in Fig. 20.
From these temperature-dependent energies, the elastic tensor components can be extracted by solving the system of equations. The results are plotted in Figs. 21 and 22.
As expected, the elastic constants generally decrease with an increase in temperature, since the thermal expansion leads to longer, weaker bonds between the ions. This decrease is exceptionally large for the C_{11} component of LN, whose value drops by around 50 % in the range up to 1000 K. This relates to the large thermal expansion within the basal plane. The in-plane elastic constants (i.e. C_{11} and C_{12}) of LN and LT behave comparibly, with similar values and slopes (note the different temperature scales of the plots): At 0 K, the values for C_{11} and C_{12} are 201 GPa and 70 GPa (225 GPa and 63 GPa), respectively, for LN (LT), which drop to 135 GPa and 30 GPa (189 GPa and 6 GPa) at 800 K. These similarities can be traced back to the almost identical lattice constant a_H and corresponding thermal expansion coefficient. At high

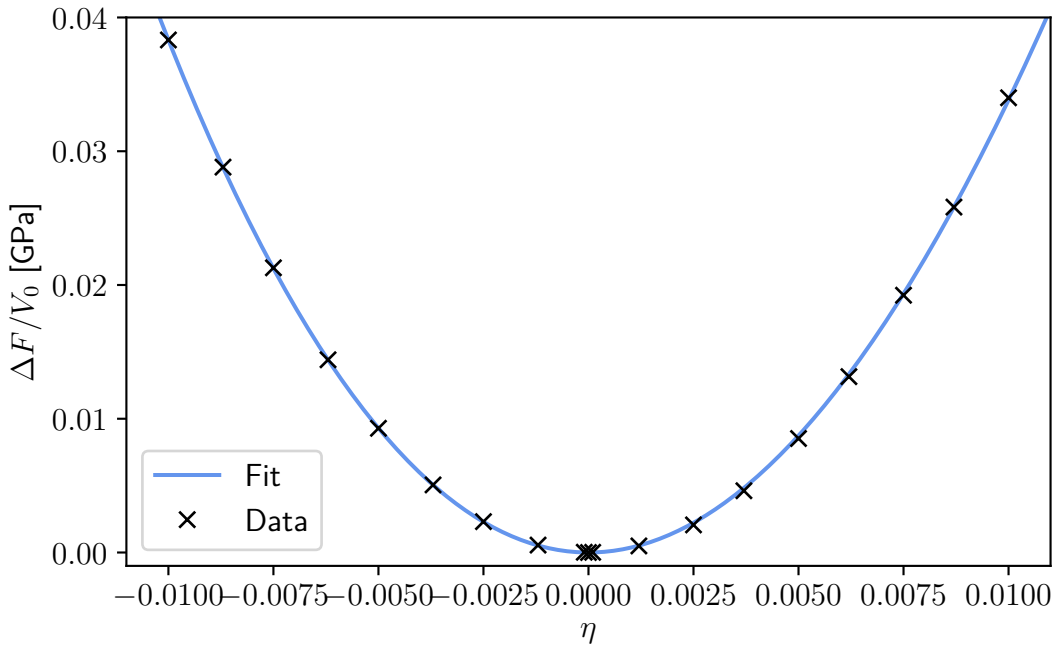

Figure 20: Change of the free energy of LT with respect to an applied strain η according to the strain tensor η_5 at 300 K. The datapoints are fitted using the polynomial (3.4).

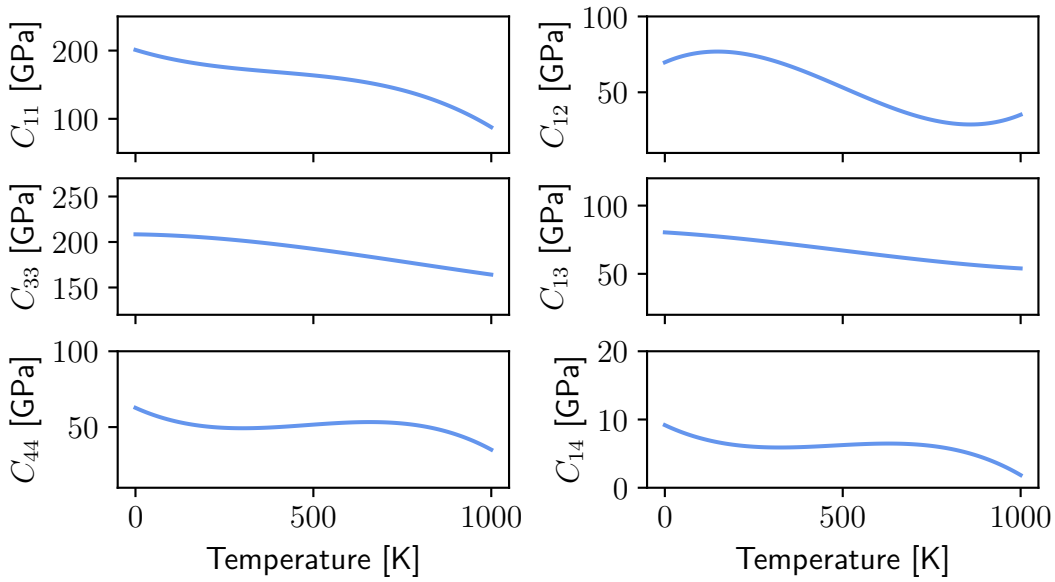

Figure 21: Elastic constants as a function of temperature of LN.

temperatures over 900 K, an upwards slope can be observed for the C_{12} component of LN. However, since the in-plane lattice constants steadily increase with temperature, this behavior might relate to the known failure of the harmonic approximation for phonons at high temperatures. More drastic differences between the two materi-

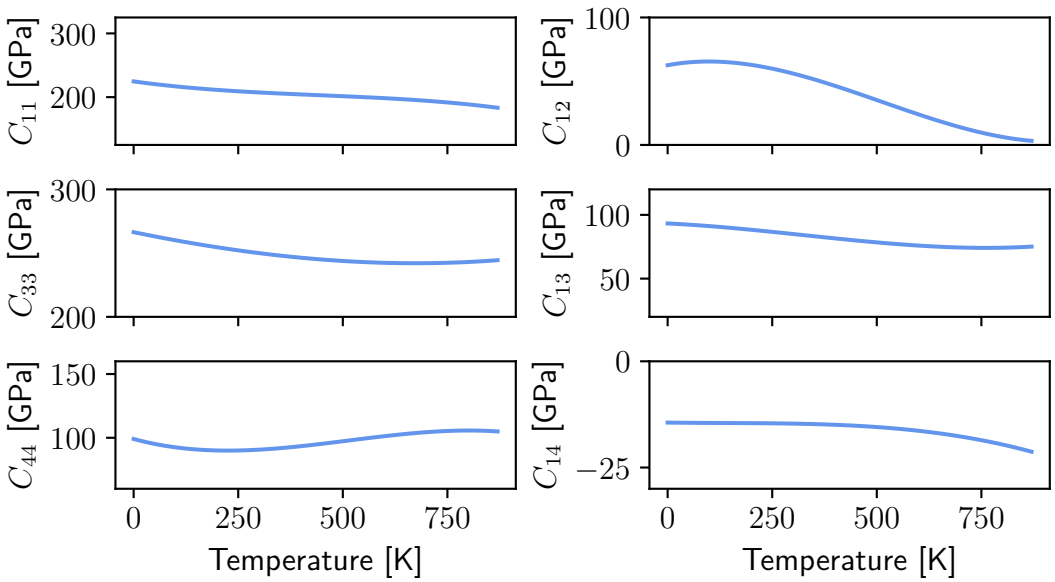

Figure 22: Elastic constants as a function of temperature of LT.

als can be observed for the other elastic constants: All of these involve a component parallel to the polarization axis, either through axial or shear strain. For these components, LT features overall larger values, and is thus more robust against deformations parallel to the polarization axis than LN. This effect might be explained by the different bonding lengths of Ta-O and Nb-O: The shorter Ta-O bonding length implies a stronger chemical bond, and thus a more rigid system compared to LN. Curiously, the elastic constant C_{14} has a different sign in both systems, meaning that LN can be more easily sheared along the xy-plane while simultaneously stretched along the y-axis, as compared to a simultaneous stretch along the x-axis. For LT, the opposite statement holds true.

The results are in good agreement to experimental measurements, especially for the diagonal components of the elastic tensor: In a comprehensive study by Bouchy *et al.* [71], the elastic constants of LN over a wide temperature range have been determined and compared to available literature values. Even though the here calculated values do well agree with the measurements, some caution is required when comparing the results: First, the experimental values assume a linear thermal expansion of both lattice constants, in order to extract material parameters. Clearly, this assumption does not hold for the extraordinary crystal axis, as has been shown in Ref. [18] and was confirmed by the simulations in chapter 3.5.1. Further, the measured samples and the experimental setup itself have a significant influence on the extracted properties, resulting in differences of the elastic constants of up to 50 %, and even contrary behavior with increasing temperature (compare e.g. Refs. [71] and [72]). Lastly, the simulations do not consider additional thermal effects, e.g. diffussion or phonon-phonon interactions, which could significantly alter the extracted values for the elastic constants. For LT, similar considerations have to be made: Here, the error for the diagonal components is again significantly smaller compared to the off-

diagonal components [73–75]. However, both are within the to be expected experimental uncertainty. Since the ambiguity in the conventional definition of the elastic tensor leads to a change of the sign of the elastic constant C_{14}, it is not clear to which entry of the elastic tenor (i.e. which sign) the experimental measurements refer to. The here attributed entries and signs are, however, in agreement to all available measurements [71–75].

3.5.3 Piezoelectric Coefficients

The piezoelectric tensors link mechanical deformations to changes in the polarization within a crystal. Only non-centrosymmetric crystals may show this property.
Using the same convention as established for the elastic tensors regarding the unit cell orientation, the direct piezoelectric tensor e of LN and LT reads as

$$e_{ijk} = \begin{pmatrix} 0 & 0 & 0 & 0 & e_{15} & -2e_{22} \\ -e_{22} & e_{22} & 0 & e_{15} & 0 & 0 \\ e_{31} & e_{31} & e_{33} & 0 & 0 & 0 \end{pmatrix},$$

such that four independent entries appear. Analogously, the converse piezoelectric tensor d shows the same symmetries as the direct piezoelectric tensor e. All entries can be readily extracted using Eqs. (2.67) and (2.66), since the elastic tensor (and thus its inverse) are known from the previous section. Only the lattice's thermal expansion is considered for taking temperature effects into account. All four direct piezoelectric coefficients are shown in Fig. 23 for LN, and Fig. 24 for LT.

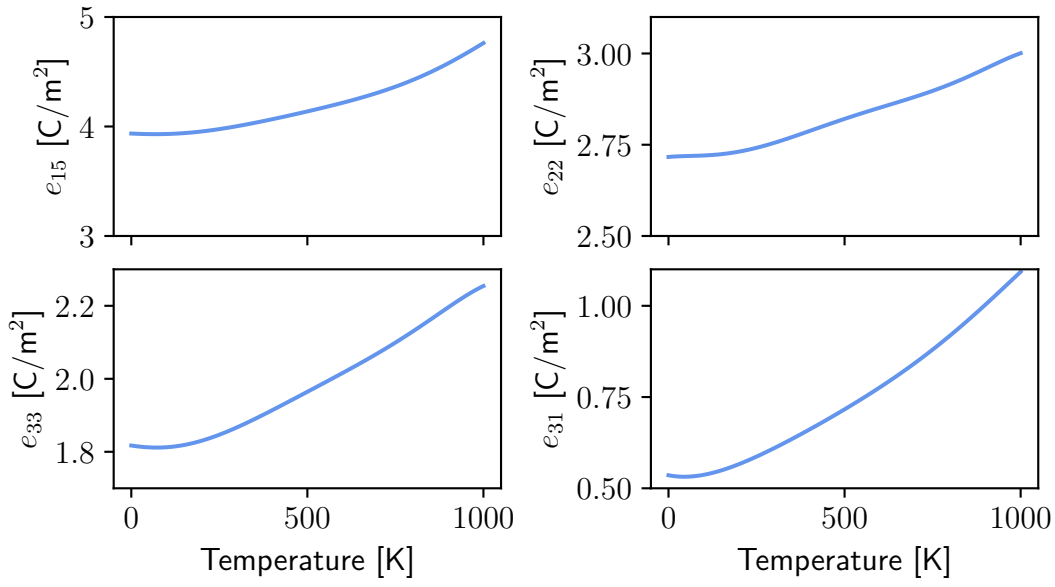

Figure 23: Direct piezoelectric coefficients for ferroelectric LN as a function of temperature.

All components show an increase with respect to temperature for both, LN and LT. The component e_{31} is smallest, since it links strains in the unpolar basal plane to

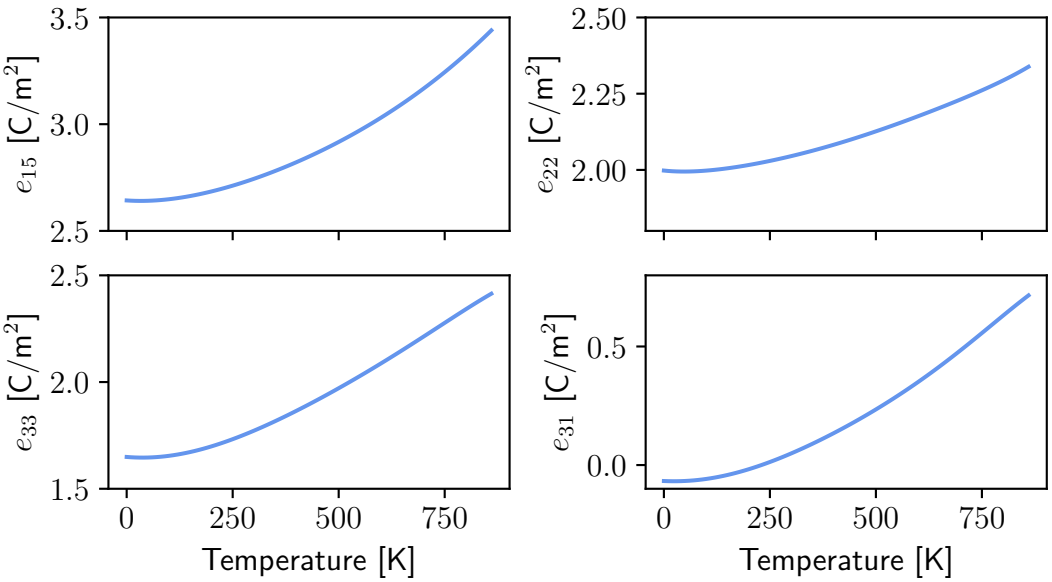

Figure 24: Direct piezoelectric coefficients for ferroelectric LT as a function of temperature.

changes of the polarization parallel to the spontaneous polarization direction. Curiously, its sign changes from negative to positive in LT, whereas all other components are strictly positive.

The results for temperatures near the Curie temperature have to be interpreted with caution: No phase transition effects (such as the change of equilibrium positions of the ions) are included. Indeed, the piezoelectric coefficients should continously vanish at the transition temperature, as the crystal becomes centrosymmetric. Still, the here presented data should give reasonable results for temperatures far below the respective Curie temperature.

A better comparison to experimental data can be obtained by calculating the converse dielectric tensors, which are shown in Figs. 25 and 26. Here, a more complex temperature-dependent behavior can be observed, since the converse piezoelectric tensor is coupled to the elastic tensor. Whereas d_{33} and d_{31} monotonously increase with increasing temperature, d_{15} and d_{22} show a plateau or even slight decreases around room temperature. The observed values around this temperature are all in good agreement to observations [72, 76], even though the calculations systematically overestimate the experimental values. This overestimation can easily be explained, since the calculations presented here are not incorporating the temperature-dependent ionic positions, which are known to continuously shift towards the paraelectric phase for increasing temperatures [P6]. This leads to a decrease in the spontaneous polarization at higher temperatures, which in turn lowers the piezoelectric coefficients. Thus, analogously to the direct piezoelectric tensors, the calculated results for the converse piezoelectric tensors are not expected to hold at elevated temperatures near the transition temperature.

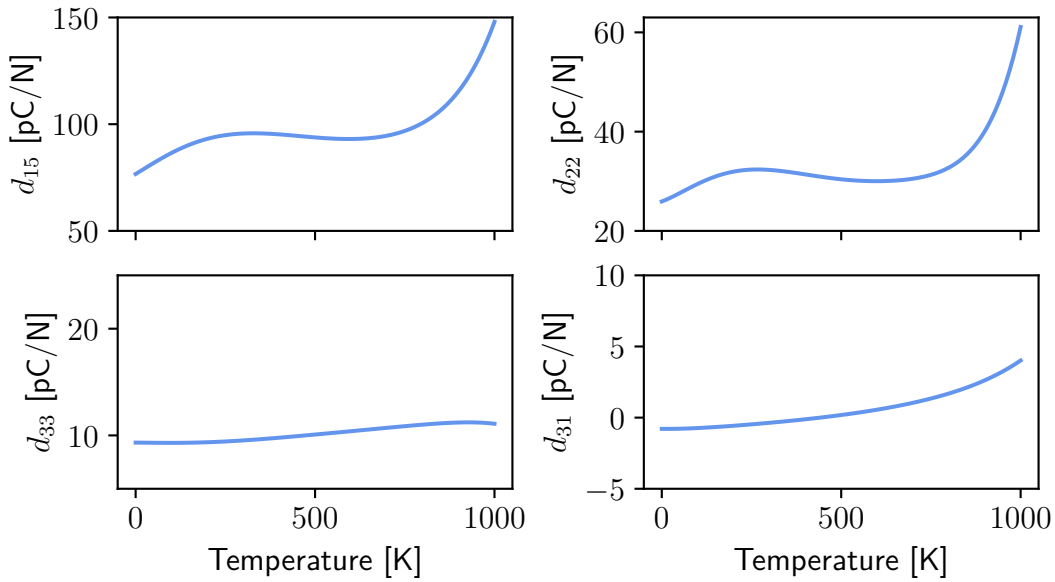

Figure 25: Converse piezoelectric coefficients for ferroelectric LN as a function of temperature.

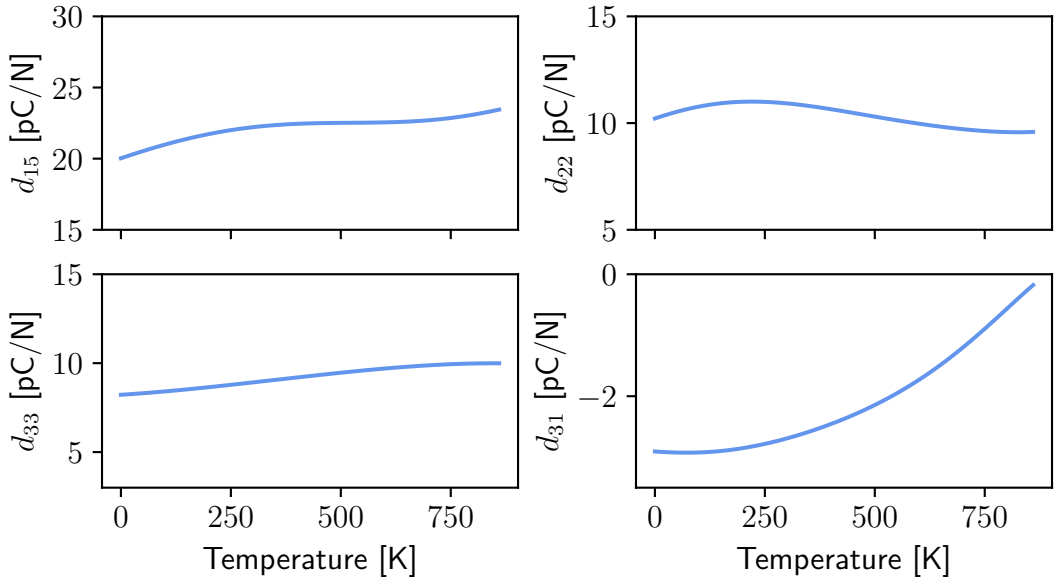

Figure 26: Converse piezoelectric coefficients for ferroelectric LT as a function of temperature.

3.5.4 Acoustic Properties

Sound can be described as an elastic wave that propagates through a medium. Thus, with knowledge of the elastic tensor, the anisotropic sound velocities within a material can be determined. Indeed, the elastic constants are commonly extracted by measuring the sound velocities (e.g. Ref. [76]). The Christoffel equation connects

these two quantities:

$$\sum_{ij} \left(M_{ij} - \rho\omega^2 \delta_{ij} \right) s_j = 0, \tag{3.5}$$

where $\hat{s}$ denotes the polarization of a monochromatic wave with frequency ω and wave vector **q**. The material's mass density is given by ρ. The Christoffel matrix M is directly related to the elastic tensor C by

$$M_{ij} = \sum_{mn} q_m C_{imnj} q_n. \tag{3.6}$$

Clearly, the phase velocity of mode i $v_i^p = \omega_i(\mathbf{q})/q$ depends on the direction of its wavevector **q**, but not on its magnitude. The eigenvalue problem Eq. (3.5) is solved using the *Christoffel* python module [77], whereby three phase velocities (one longitudinal and two transverse which are referred to as primary and secondary, respectively) can be extracted for each combination of **q**-directions. The polarization directions of the waves are given by their respective eigenvectors.
Typically, sound waves are not purely monochromatic. Hence, instead of the phase velocity, the group velocity is considered, which can be calculated from the phase velocity by taking its gradient in reciprocal space, i.e. $v_i^g = \nabla_{\mathbf{q}} w_i(q)$. The onto a sphere projected group velocities are shown in Fig. 27. Note, that the group velocity is generally not parallel to the phase velocity.

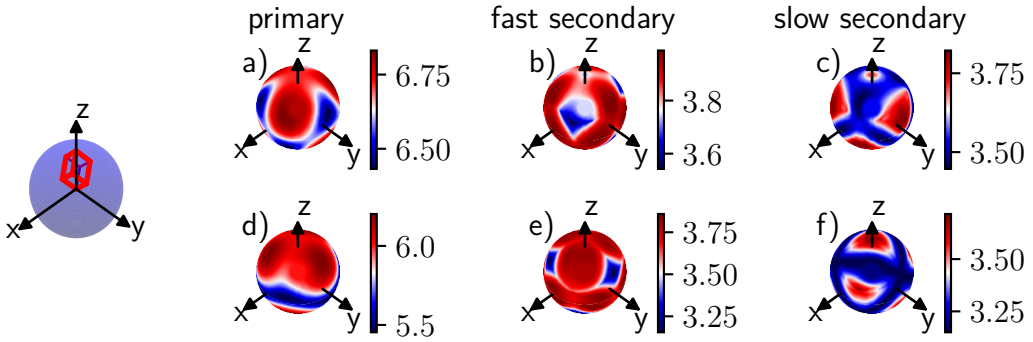

Figure 27: Group velocities of LN (top row) and LT (bottom row) at 0 K projected onto a sphere. The primary (longitudinal, a) and d)), and the secondary (transversal, fast [b) and e)] and slow [c) and f)]) velocities are shown. The schematic orientation of the rhombohedral unit cell within the projected sphere is shown on the far left side. The velocities are color coded in units of km/s.

For LN, the longitudinal waves are fastest perpendicular along the rhombohedral face intersection, and slowest at the face centers. The only exceptions are the two corners along the z-axis, where the sound velocity is only slightly lower compared to the face intersections. Compared to LN, the behavioral pattern for the primary branches of LT is rotated by 30° around the z-axis, i.e. the acoustic waves are fastest at the rhombohedral plane centers. This, and all other equivalent rotations of the velocity patterns,

can be traced back to the different signs of the elastic component C_{14} between LN and LT.
The faster transversal waves (b) and e)) in Fig. 27) show a similar pattern as the longitudinal branches (a) and d)), but with an additional rotation of 30° around the z-axis. The pattern is again rotated by 30° around the z-axis between LN and LT. The rhombohedral face intersection along the z-axis now shows a clear local minimum for LN. The slower transversal branch patterns of LN and LT are reversed with respect to the fastest and slowest regions, compared to their corresponding longitudinal pattern. Here, a clear maximum can be observed along the z-axis.
Compared to experimental data for LN, the velocities of the longitudinal branches are slightly underestimated, whereas the transversal branches are in good agreement to the measured values [78]. For LT, the reverse statement holds [76]. Still, the dependence on propagation and polarization directions is well reproduced for both materials. The group velocities for specific high-symmetry combinations of propagation and polarization directions are given in Tabs. 4 and 5 in the Appendix.
As the temperature increases (see Sec. B.2.4 in the Appendix), the acoustic velocities are lowered. The general spatial trends do, however, not change.

3.6 Li-deficient Lithium Niobate

Even though LN is being used in a vast range of applications, knowledge of its electronic band gap is limited: As has been pointed out in previous works, experimentalists typically measure the optical absorption edge that is later interpreted as the electronic band gap [79, 80]. Comparing the mesured optical band gap with the within DFT calculated electronic band gap yields generally a good agreement [81], which can only be achieved by a fortunate cancellation of errors: The measured absorption edge values contain excitonic effects that are not considered within DFT, which lead to an absorption edge at lower energies compared to the electronic band gap. On the computational side, quasi-particle effects, such as e.g. electron-phonon couplings, are ignored. The within DFT assumed delocalization of the 4d electrons present in Nb introduces another error, which can be corrected by a Hubbard parameter as introduced in Sec. 2.2.2. Further, the absorption edge is affected by the stoichiometry of the crystal, and often congruent LN samples are being used in experiments. In fact, the stoichiometry of a sample can be determined by measuring its absorption edge [1, 82].
In order to explain this behavior, a closer look at the electronic structure is necessary. Different formation defects within LN have been proposed [83–86], of which the so-called Li-vacancy model is widely accepted as being energetically favored [87–89], whereas oxygen vacancies can only play a minor role [89, 90]. Here, a congruent LN crystal is simulated by successively removing Li^+ ions from the stoichiometric lattice. Different supercell sizes are used, up to a $4\times4\times4$ supercell. The vacancies are positioned such that their distance is maximized, in order to minimize the Coulomb interaction between the sites. Within this model, the charges are, as a first approximation, not compensated. The Li-vacancy model is created by removing five Li^+ from a $4\times4\times4$ supercell of stoichiometric LN, and setting a Nb^{4+} ion at a randomly chosen

vacant lithium site that compensates the electronic charges of the Li^+ vacancies [25]. Again, the Li^+ vacancies are placed to have a maximal distance. Since it is assumed that oxygen vacancies do not occur within congruent lithium niobate, and instead niobium ions compensate for Li-deficiencies, its composition is generally given in units of the lithium oxide content within the crystal [1, 92], i.e.:

$$LiNbO_3 = 0.5 \cdot Li_2O + 0.5 \cdot Nb_2O_5. \tag{3.7}$$

For better comparability to existing works, the oxygen contents in the above formulation are ignored in order to characterize the within this work simulated congruent crystals. If not explicitly written out, the niobium pentoxide content is assumed to be 50 mol% if no additional niobium ions are added or removed compared to a stoichiometric cell. The Li-vacancy model used in this work is written as

$$Li_{124}Nb_{129}O_{384} = 0.480 \cdot Li_2O + 0.504 \cdot Nb_2O_5. \tag{3.8}$$

Finally, an energy correction according to Eq. (2.15) with a Hubbard parameter of $U = 4\,\text{eV}$ is set for the niobium 4d shell, which has been determined in previous works [93, 94].
The electronic band structures are calculated for the different models which are exemplarily shown in Fig. 28. For a better visual comparison, the bands are all unfolded onto the first Brillouin zone of the primitive unit cell, and weighted according to their spectral weight P via

$$P_{m\mathbf{K}}(\mathbf{k}) = \sum_n \left|\langle \psi^{\text{SC}}_{m\mathbf{K}} | \psi^{\text{PC}}_{n\mathbf{k}} \rangle\right|^2 = \sum_{\mathbf{g}} \left|u_{m\mathbf{K}}(\mathbf{g} + \mathbf{k} - \mathbf{K})\right|^2, \tag{3.9}$$

where **K** and **k** denote **k**-vectors in the supercell (SC) and primitive cell (PC), respectively. It holds that $\mathbf{K} = M\mathbf{k}$, with M being the matrix used to transform the primitve cell to the super cell. Band indizes are labelled with m and n, **g** denotes a reciprocal lattice vector. Only information about the Bloch factors $u_{m\mathbf{K}}$ of the super cell are needed to calculate the weights. The unfolding algorithm is used as implemented in the *VASPKIT* package [95].
Adding Li^+ vacancies does not drastically change the electronic band structure near the Fermi level compared to the stoichiometric unit cell, since mainly two core electrons (corresponding to the 1s electrons of the removed Li ion) are removed. The absence of some Li ions forces the ions surrounding these vacancies to slightly change their relative positions, thus breaking symmetries of the crystal and degeneracies of the electronic bands.
This effect becomes more pronounced as more Li^+ vacancies are added. Overall, the change of the ionic background potential, which is induced by these slight structural changes, leads to a minor reduction of the electronic band gap. The same reasoning can be applied to discuss the band structure of the Li-vacancy model. However,

[25] In Ref. [91] it has been proposed that this niobium ion may be able to move to a neighboring, empty oxygen octahedron.

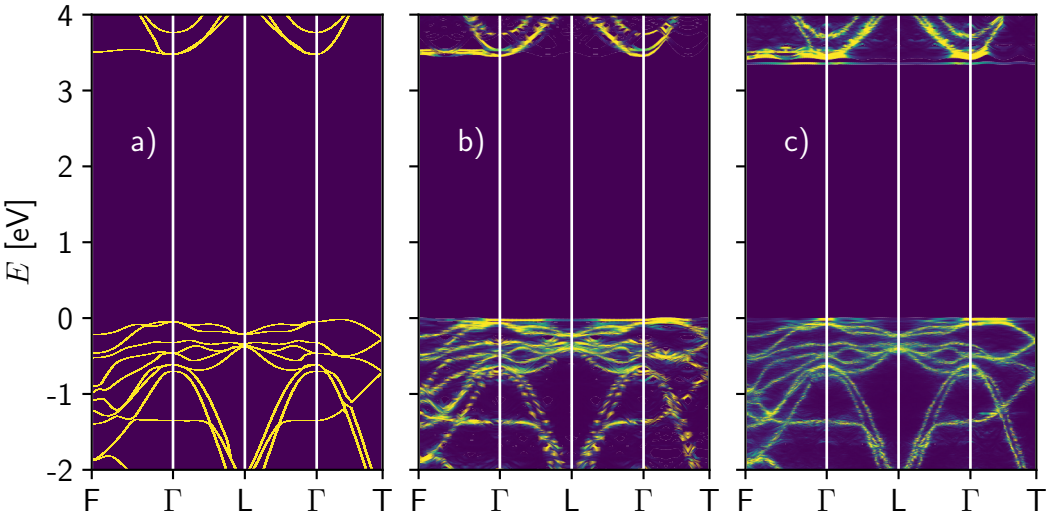

Figure 28: Effective electronic band structure of LN: (a) stoichiometric, (b) 49.1 mol% Li_2O, (c) 48.4 mol% Li_2O and 50.4 mol% Nb_2O_5. The bands are unfolded to the first Brillouin zone of the primitive unit cell.

a pronounced localized defect state just below the conduction band minimum can additionally be observed here, which has been reported previously [96]. This defect state has a strong d-like characteristic and is centered around the Nb_{Li} position. Thus, the electronic band gap is closed further compared to the structures which only include Li^+ vacancies.

In order to determine the experimentally accessible optical absorption edge, the dielectric function is calculated from the electronic structure within the IPA: The number of considered conduction bands per formula unit is increased to 23, such that the dielectric function is converged up to excitation energies of 10 eV. The results are presented in figure 29.

Similar to the electronic band structure, only minor changes compared to the stoichiometric cell can be observed, for both the ordinary and extraordinary component of the dielectric function. The main absorption bands at around 5 eV and 8.5 eV in stoichiometric LN (black curve) have been previously reported, e.g. in Ref. [97]. Similarily, their relative difference in intensity in the ordinary and extraordinary optical direction is in good agreement to previous investigations. For decreasing lithium content, the spectra shift to slightly lower energies, seemingly in agreement to the closing of the electronic band gap. Still, according to Eq. (2.80), the overlap of the conduction and valence states plays a major role in the absorption rate, and a one-to-one correspondence between the optical absorption and the electronic band structure is generally not applicable. With addition of the charge-compensating niobium ion, the absorption bands experience an additional red-shift.

To further analyze these absorption shifts, the absorption edge is plotted as a function of the congruent lithium niobate composition. Unfortunately, the concept of an absorption edge is not uniquely defined: Experimentalists typically measure the ab-

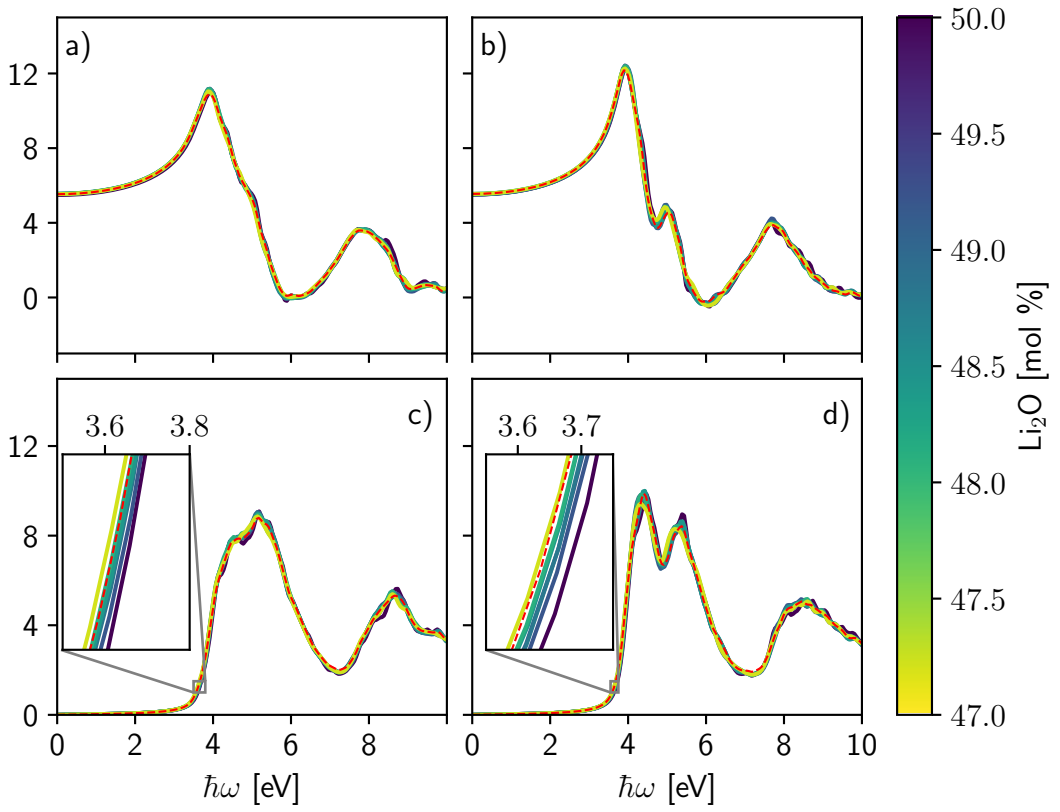

Figure 29: Real (upper row) and imaginary part (lower row) of the dielectric function of congruent LN calculated within DFT in the IPA. The panels at the left and at the right hand side show the ordinary and extraordinary component of the dielectric function, respectively. The red line denotes a concentration of 48.4 mol% Li_2O and 50.4 mol% Nb_2O_5.

sorption coefficient, and perform a Tauc fit near the onset of the absorption (see e.g. Ref. [P5]). This method dependes largely on the chosen fitting region, and can thus not unambiguously define a physical quantity. In other cases, an arbitrarily chosen threshold value is set, and the absorption edge is then chosen as the energy where the absorption coefficient increases beyond this set value (see e.g. Ref. [1]). Within this spirit, the here calculated absorption edge is defined as the energy where the imaginary part of the dielectric function first passes a value of two. Of course, this does not allow for a quantitative comparison of results (which is not only limited by the chosen definition of the absorption edge, but further hindered by the exclusion of excitonic and quasi particle effects), but allows for an in itself consistent analysis. The results are presented in Fig. 30. A clear dependence between the absorption edge and the composition of the congruent crystal can be observed.
Qualitatively, the data points can be fitted by a square root function via

$$E = k\sqrt{50 - c_{Li_2O}} + E_0, \tag{3.10}$$

where c_{Li_2O} is the lithium oxide content of the crystal in units of mol%. The same function has been used in Ref. [1], showing that the relatively simple model of the con-

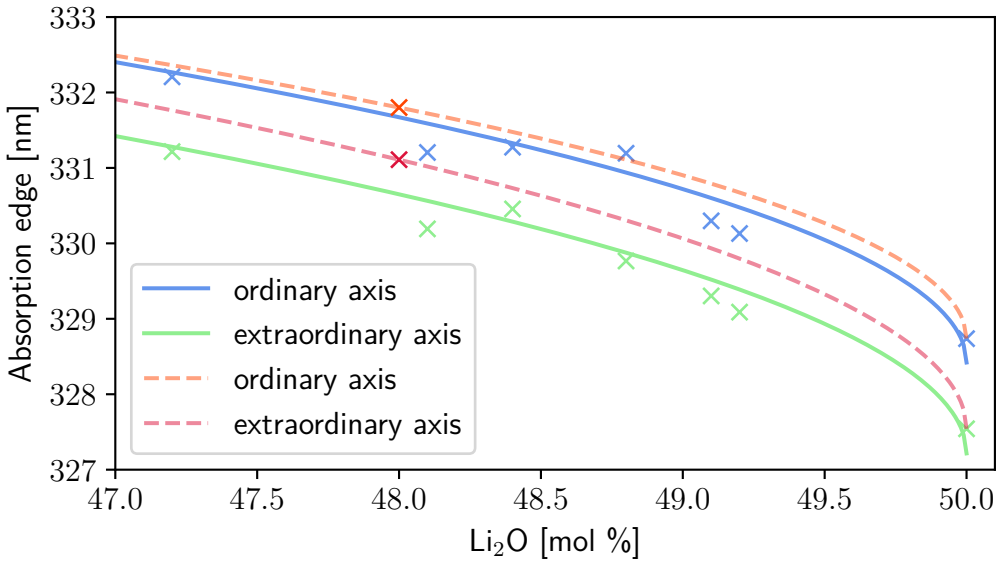

Figure 30: Absorption edge of congruent $LiNbO_3$ calculated within DFT in the IPA as a function of the Li_2O content. The data points are fitted to a square root function according to Ref. [1]. The dashed lines correspond to the Li-vacancy model, and the solid lines to the non charge compensated model.

gruent crystals that are employed here behave similarly to the real congruent crystals. Note, that the quantitative good agreement compared to Ref. [1] can only be interpreted as a coincidence. Further, the measured values exhibit a slightly stronger dependence on the Li_2O content than the simulations. The latter issue might be addressed by compensating the charges of the Li^+ vacancies by using the Li-vacancy model, as tentatively addressd in the present work and shown by the red curves in Fig. 30. However, this fit does not provide a definitive conclusion, since only two datapoints per polarization direction have been calculated.

4 Lithium Niobate-Tantalate Solid Solutions

A solid solution is defined, according to the IUPAC definition, as "a crystal containing a second constituent which fits into and is distributed in the lattice of the host crystal" [W2]. These include interstitial (i.e. the second constituents are accomodated between lattice sites of the host), and substitutional (i.e. the second constituents are replacing atoms within the host lattice) solid solutions. Generally, a solid solution of arbitrary constituent concentration can only be synthesized for the latter case. The physical properties of the parent compounds are interpolated over the compositional range of the solid solution, allowing for their enhancement or fine-tuning for applications. Since both LN and LT crystallize in the same space group R3c, and both Nb and Ta are pentavelant (within this configuration) with similar electronegativity (1.6 and 1.5 in Pauling units for Nb and Ta, respectively [W18]) and ionic radii (0.78 Å for their pentavalent, octahedral coordination [W18]), they can be substituted with each other, allowing for the synthetization of LNT solid solutions over the whole compositional range [18, 19, 98]. To maximize the entropic contributions to the free energy, it is assumed that the Nb and Ta ions are randomly distributed throughout the solid solution [99].

Simulating non-ordered random alloys is a challenging task, since the Bloch theorem does not hold in a strict mathematical sense. However, Bloch's theorem scales the many-body problem of the solid down by many orders of magnitude, and its neglience would be numerically unfeasable. Hence, additional assumptions have to be made in order to model a random ionic distribution, which still have to hold after employing periodic boundary conditions. Many different approaches have been proposed: In the *virtual crystal approximation* [100], the pseudopotentials of atoms at the sites of substituents are weighted according to the concentration within the mixed crystal. This offers the possibility of using primitive unit cells of the end compounds to model an alloy with arbitrary mixing ratio. Its main drawback is the unphysical assumption that the pseudopotentials superimpose at the substituent sites. A similar idea is proposed in the *coherent potential approximation* [101]: Here, instead of the pseudopotentials, the electronic Green's function is modified to include contributions from different atomic species, yielding an effective electronic density in k-space. Thus, this method is only available if the Green's function can be calculated (e.g. in the Green's function Koringa-Kohn-Rostoker formalism [102, 103]). Further, localized effects cannot be taken into account. Another way for simulating a random alloy is given by the *coupled cluster expansion* [104, 105]: Assuming that the material's properties (e.g. the electronic energy) can be expanded as a function of structural motifs (referred to as clusters), an effective Hamiltonian is constructed by the sum of interactions of these clusters. Its clear advantage compared to the previous methods is its explicit inclusion of local effects. However, the computational demand is far higher, and in the frame of the work presented here, this approach is not feasible. A

simplification of the cluster expansion method is given by the employment of special quasi-random structures, which are used throughout this section. Their construction, advantages, and drawbacks compared to the previously mentioned approximations will be discussed in detail in the next chapter.

4.1 Special Quasi-Random Structures

In the SQS approach, no averaging of the electronic properties takes place. Instead, a cell that mimics the localized disorder present in the mixed crystals is utilized. For each composition, only one[26] structure needs to be considered, namely the one that resembles a truly random alloy the most. This resemblance is measured by calculating the correlation function of a given (super)cell with fixed positions for the substituent ions, and comparing it with the analytically known correlation function of the true random alloy. The structure that has the most similar correlation function compared to the true random alloy is referred to as a SQS, and is subsequently used to approximate the true random alloy. Thus, the usage of SQS provides a good trade-off between the accuracy of extracted properties, and the numerical cost put in. However, certain aspects need to be considered to determine whether a in such a way constructed SQS well describes true disorder:
First, the size of the to be determined SQS has to be taken into account: For one, this size depends explicitly on the composition that one wants to analyze. For example, a LNT crystal of 25 % Ta content needs to be modeled using at least two rhombohedral unit cells, since one unit cell only contains two Nb or Ta ions. But more importantly, larger unit cells allow for a better match of the correlation function compared to the true random alloy, resulting in SQS that more closely resemble true randomness compared to SQS of smaller cell sizes. This behavior is especially obvious for concentrations of 2^{-n}% tantalum, with n being a small positive integer: For example, only the primitive unit cell would need to be considered to construct a LNT mixed crystal with 50 % tantalum. However, since periodicity of the solid is assumed, such a structure would still display short-range order, and would not be characterized by a random distribution of the substituent ions. Instead, larger unit cells allow for intrinsically breaking such short-range order. On the other hand, the SQS should be small enough to enable calculations within a reasonable computational cost.
Further, the optimal SQS has to be defined and determined in the first place: Therefore, a set of test structures is set up, consisting of supercells where the substituent sites are occupied by a randomly chosen substituent, but within a fixed composition. Each test structure (configuration) is subdivided into clusters which hold k vertices (here, the niobium and tantalum ions at approximately the centers of the oxygen cages). The correlation function of a cluster f within a configuration σ can thus be

[26] In practice, more than one SQS for each composition should be used to yield a better statistical significance.

calculated as

$$\Pi_f(\sigma) = \frac{1}{N D_f} \sum_l \left(\prod_{i=1}^{k} S_i \right), \tag{4.1}$$

where N is the number of clusters at substituent sites l within the configuration σ, D_f is the multiplicity of cluster f within σ, and $S_i = \pm 1$, depending on the atom type at vertex i. The correlation function of the true random alloy R is given by

$$\Pi_f(R) = (2x - 1)^k, \tag{4.2}$$

where $x \in [0, 1]$ denotes the substituent concentration. The similarity between configuration σ and the true disordered alloy R is measured by the error function ϵ via [106]

$$\epsilon(\sigma) = \sum_f \frac{D_f}{(k d_f)^n} \left| \Pi_f(\sigma) - \Pi_f(R) \right|, \tag{4.3}$$

where n assigns the weight contribution of clusters of different sizes k, and d_f denotes the mean distance between substituent sites within cluster f. Here, $n = 2$ is chosen, since the resulting SQS do not depend on n for $1 < n < 5$ [22]. Using this formalism, larger clusters contribute less to the error function than smaller ones, channeling the focus on local site effects. Finally, the best matching configurations can be extracted as the ones with the lowest error, which denotes them as SQS.
In most cases, it is not numerically feasible to simply examine all possible ionic configurations by computing their correlation function and comparing them to the true random alloy, since the configuration space can easily span $\approx 10^9$ different structures. Instead, the configuration space is randomly sampled for up to 10^5 candidates, and only the best matches from this subset are extracted.
In this work, two sets of SQS are employed: Rhombohedral 2×2×2, and orthorhombic 2×1×1, 1×2×1 and 1×1×2 supercells [22, P5]. The rhombohedral SQS contain 80 atoms, of which up to 16 are either niobium or tantalum. Thus, a total of 16 different concentrations can be examined, resulting in a sampling of the Ta concentration of Δx=0.0625. The orthorhmobic SQS include 120 atoms, and thus allow for a finer sampling of the concentration of Δx=0.041$\overline{6}$. In practice, the SQS are only determined up to x=0.5, since the correlation function is invariant under an exchange of atomic types (x$\rightarrow$1-x and S$\rightarrow$ -S). Hence, all niobium ions are replaced by tantalum ions and vice verse when comparing SQS with concentrations of x$<$0.5 and x$>$0.5. Since the structures with only one substituent compared to the end compounds are all equivalent by translations, only one structure is being used for these concentrations (i.e. for x=0.041$\overline{6}$; 0.0625; 0.9375; 0.958$\overline{3}$). Only the ferroelectric phase is studied throughout this section.

4.2 Structural Properties

Even though LN and LT feature similar lattice constants in the basal plane, they show a difference of about 0.04 Å along the low symmetry axis (see e.g. Sec. 3.5.1). Such

differences have been shown to be especially important in devices consisting of layers of different materials: In the semiconducter industry for example, combinations of silicon and germanium layers help in constructing integrated circuit transistors [107]. Their respective lattice mismatch induces a strain on the lattice that defines the physical characteristics of the device [108–111]. For ferroelectrics, the potential of similar applications for integrated optics is virtually unexplored. Thus, knowledge of the lattice parameters as a function of the alloy composition is a crucial first step for designing and optimizing similar devices, using lithium niobate, lithium tantalate, and their solid solutions as a possible foundation.

To extract the structural properties of LNT, the SQS unit cells have to be optimized: Here, DFT calculations are used to relax the ionic positions and lattice vectors for different, fixed unit cell volumes. The optimization is stopped if the Hellmann-Feynman forces acting on all ions are smaller than 0.005 eV Å^{-1}. The volume is then plotted as a function of the electronic energy and fitted with the Murnaghan equation of state (2.57), which yields the equilibirum volume and the bulk modulus. An exemplary plot for $LiNb_{0.75}Ta_{0.25}O_3$ is shown is Fig. 31. Note, that in contrast to Secs. 3.2 and 3.5.1 no phononic contributions are taken into account here, such that no assumption regarding the thermal behaviour of the lattice volume can be made. A final DFT optimization is performed using the extracted equilibrium volume, which additionally yields the lattice constants and ionic positions for each composition. All the available SQS are considered in the calculations, including the rhombohedral 2×2×2 and orthorhombic 2×1×1, 1×2×1, and 1×1×2 supercells.

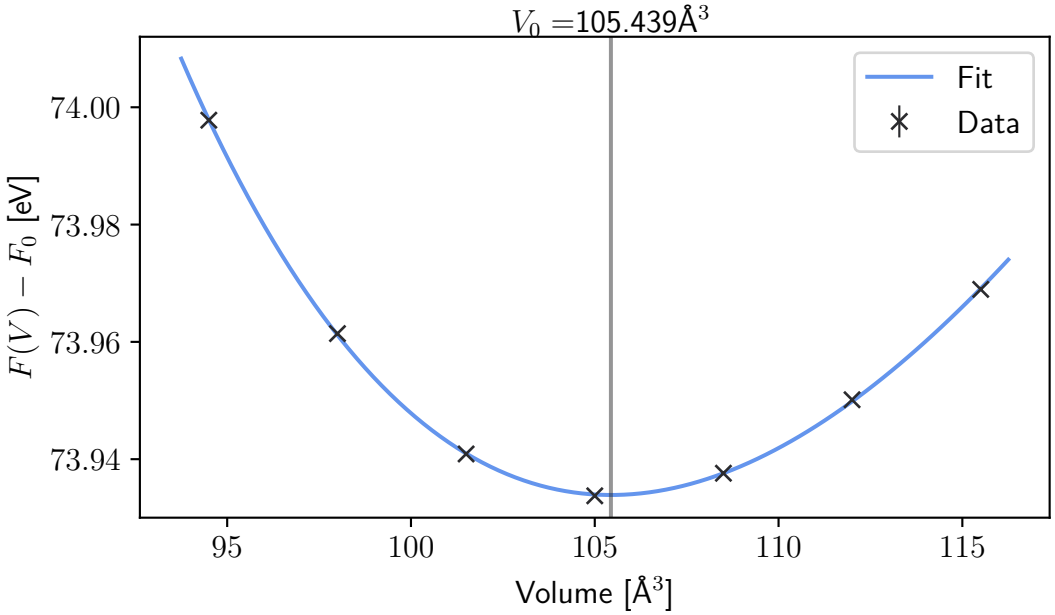

Figure 31: Total electronic energy as a function of the unit cell volume of one SQS for $LiNb_{0.75}Ta_{0.25}O_3$. The data points are fitted using the Murnaghan equation of state. The predicted equilibrium volume is indicated as V_0 with an energy of F_0 (normalized to a primitive unit cell of the end compounds).

The lattice constants as a function of the tantalum content of the solid solution are plotted in Fig. 32, and summarized in Tab. 6 in the appendix. Since slight variations in the calculated values occur, especially due to the usage of different SQS modeling the same composition based on supercells of different symmetry, the average lattice constants are shown. An error bar denotes the maximal deviations from the average.

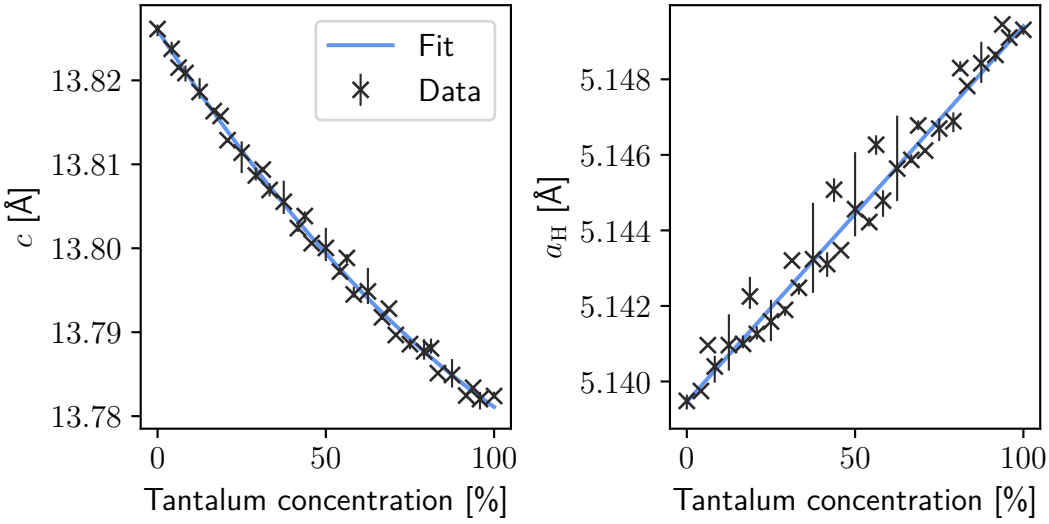

Figure 32: The lattice constants a_H (right panel) and c (left panel) as a function of the tantalum concentration in LNT. Both lattice constants are normalized to a primitive cell of the end compounds.

With an increase in Ta content, an almost linear increase can be extracted for the lattice constant a_H (the basal plane of the hexagonal structure), which emphasizes the empirically derived and often employed Vegard Law:

$$a_H^{LiNb_{1-x}Ta_xO_3} = (1-x) \cdot a_H^{LiNbO_3} + x \cdot a_H^{LiTaO_3}. \tag{4.4}$$

Overall, the dependency of a_H on the tantalum concentration is rather small, with a variation of around 0.2 %. The composition can thus only be exploited to a certain extent in order to tweak the in-plane matching of LNT films on different substrates. The rhombohedral SQS feature a systematically larger lattice constant a_H than the orthorhombic SQS (around 0.004 %), which is, however, still within the numerical accuracy of the calculations. In contrast, the height of the hexagonal unit cell c decreases with an increase in the Ta content of LNT, with a variation of around 0.4 %, which is twice as large as the variation for the in-plane lattice constant a_H. This decrease features a slight sublinear behaviour, which can be indicated as an additional bowing parameter b in Vegard's Law:

$$c^{LiNb_{1-x}Ta_xO_3} = (1-x) \cdot c^{LiNbO_3} + x \cdot c^{LiTaO_3} - b \cdot x(1-x). \tag{4.5}$$

Both lattice constants are remarkably well reproduced throughout the whole compositional range compared to experimental results [19, 112]

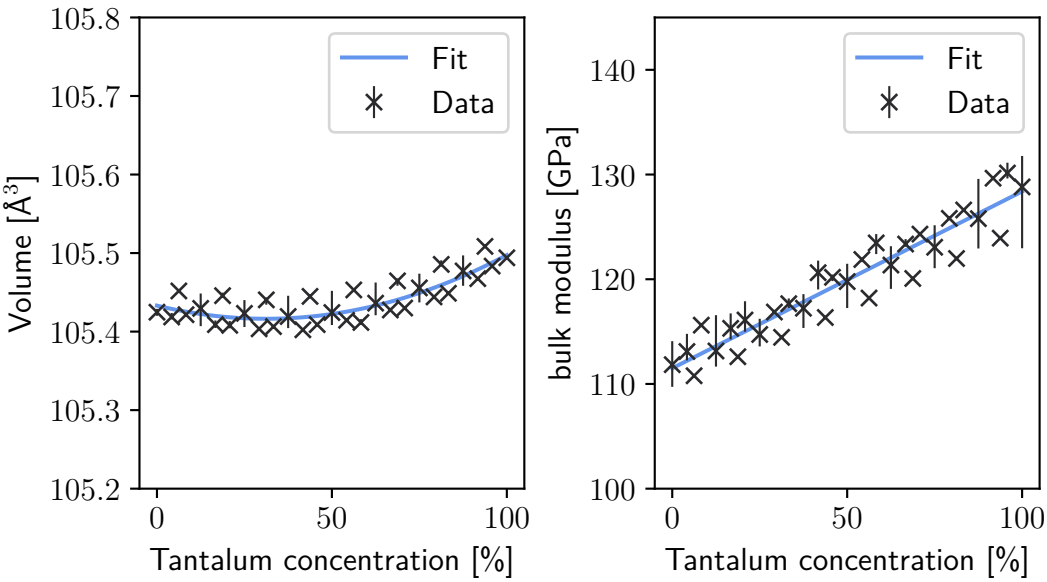

Figure 33: The lattice volume (left panel) and the bulk modulus (right panel) as a function of the tantalum concentration in LNT.

The unit cell volume, given in Fig. 33, shows a strong sublinear behaviour, with a minimal volume at around 40 % Ta-content.

The from the Murnaghan equation of state extracted bulk modulus shows a linear behaviour, as can be seen in Fig. 33. The extracted values for the end compounds (K_{LT}=130.8 GPa, and K_{LN}=112.6 GPa) are in good agreement with available experimental values [113] as well as with other theoretical results ($K_{\mathrm{LT}}^{\mathrm{theo}}$=124 GPa and $K_{\mathrm{LN}}^{\mathrm{theo}}$=102 GPa [114]).

The spontanueos polarization in the LNT crystal family is dependent on the displacement of the Li ions from the O planes, as well as of the off-centering of the Nb or Ta ions from the O cages (see e.g. Fig. 9). The spontaneous polarization decreases from 71 µC cm^{-2} for LN [57] to 60 µC cm^{-2} for LT [17], even though the Nb and Ta ions are formally isovalent. This discrepancy can be partially explained by analyzing the displacement distance of the respective ions from their high-symmetry position: The tantalum ions are located almost 0.08 Å closer to the oxygen cage centers than the niobium ions, which significantly weakens their contribution to the spontaneous polarization. Similarly, the Li ions in LT are located around 0.7 Å nearer to their high-symmetry positions than in LN. This, however, contributes only marginally to the spontaneous polarization, since the Li ions carry a much smaller (effective) charge than the Nb or Ta ions. The usage of SQS to model the LNT solid solutions provides a unique look into that behaviour for the whole compositional range, as local site effects are explicitly present in the cells. In Fig. 34, the magnitude of the displacement of the Li, Nb, and Ta ions from the high-symmetry positions are shown. An almost linear increase in the distance between the Nb and Ta ions from the oxygen planes can be observed for an increasing Ta content. This corresponds to an overall movement towards the oxygen cage centers of both ions with an increase in the tantalum

concentration. The distance between the Li ions and the oxygen planes linearly decreases with an increase in the Ta content, again corresponding to a movement towards the high-symmetry positions. All of these effects result in a decrease of the spontaneous polarization with an increase in tantalum within the mixed crystals. A quantitative analysis using effective charges will be presented in Sec. 4.6. Finally, the distance between different oxygen layers (i.e. the height of the oxygen octahedra) as a function of the LNT composition shows a slight, sublinear decrease of the octahedra height with an increase in the tantalum content.

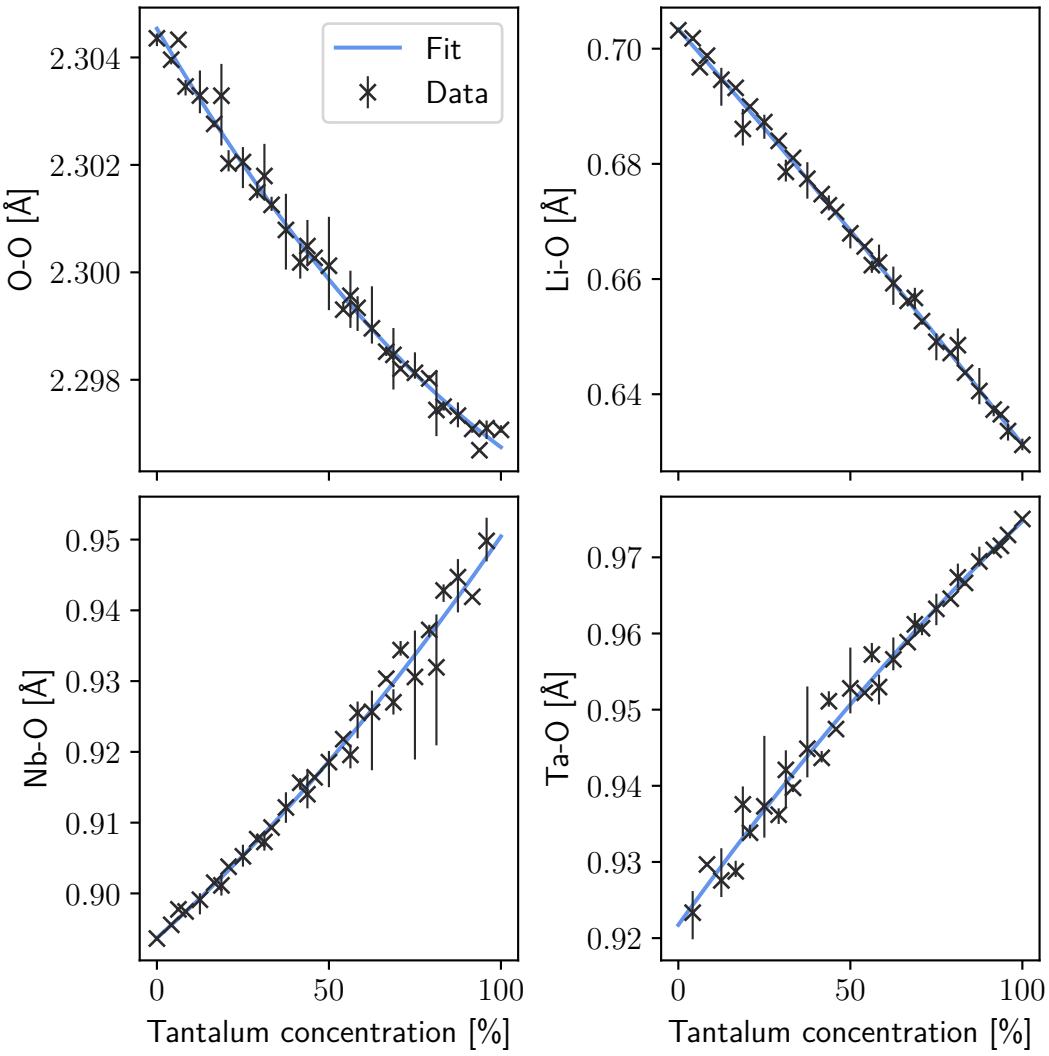

Figure 34: Average distance of all atomic types in the LNT crystal family to the next neighboring oxygen plane in z-direction. The error bars denote the maximal average deviation between different SQS.

4.3 Thermal Properties

Compared to Sec.3.2, the numerical costs for thermal calculations within the SQS approximation is far greater: For one, no symmetry reductions can be used (e.g. regarding atomic displacements in the x- or y-direction). Secondly, the SQS unit cells include more atoms (at least by a factor of eight), which means that altogether more phonon modes (at least 24 times more) need to be explicitly calculated. Further, the whole compositional range of the mixed crystals need to be studied, multiplying all of the aforementioned difficulties. The following discussion is thus limited to harmonic phonons, and no thermal expansion or other anharmonic effects can be presented.
Similar to Sec.3.2, the harmonic phonon DOS is calculated using the finite displacement method. Here, supercells based on the orthorhombic SQS are employed, where the cells are multiplied such that the resulting supercells have similar lattice constants in each direction. This ensures that long-range effects are taken into account up to a comparable accuracy in each direction. The resulting phonon frequencies are then interpolated onto a 20×20×20 k-point grid by using the Parlinski-Li-Kawazoe method, resulting in an error of around 3 % compared to a 50 % denser mesh. Some imaginary frequencies are present near the Γ-point: These arise, because the supercells used are not large enough to capture the full long-range interaction in the material, and are thus not an indicator of instability of the crystal phase as in chapter 3.3 [115]. For the following calculations, these imaginary frequencies are taken as real, positive values.
Using Eq.(A.4), the specific heat capacity at constant volume can be calculated. The results are presented in Fig. 35 (upper panel). For LN, a value of 0.64 J g^{-1} K^{-1} is extracted at room temperature, whereas a 38 % lower value of 0.40 J g^{-1} K^{-1} is identified for LT. Both results are in very good agreement to experimental data (0.70 J g^{-1} K^{-1} for nearly stoichiometrc LN [53], and 0.42 J g^{-1} K^{-1} for LT [W17]), and theoretical results for c_p [51]. By selecting a fixed temperature, it becomes more apparent that c_V behaves sublinearly as a function of the Ta content. In the lower panel of Fig. 35, an exemplary temperature of 300 K has been chosen.
Using the empirical Vegard Law

$$c_V^{\mathrm{LiNb_{1-x}Ta_xO_3}} = (1-x)\cdot c_V^{\mathrm{LiNbO_3}} + x\cdot c_V^{\mathrm{LiTaO_3}} - b\cdot x(1-x). \tag{4.6}$$

the bowing parameter responsible for this sublinearity can be extracted for each temperature. Following a similar trend as the specific heat capacities themselfes, the bowing parameter increases with temperature.

4.4 Electronic Properties

In previous investigations, profound deviations from Vegard's law have been observed for the electronic band gap within the LNT crystal family [116]. Analogously to Eq. (4.5), a bowing parameter b is introduced in order to describe the deviation from a linear behaviour:

$$E_{\mathrm{g}}^{\mathrm{LiNb_{1-x}Ta_xO_3}} = (1-x)\cdot E_{\mathrm{g}}^{\mathrm{LiNbO_3}} + x\cdot E_{\mathrm{g}}^{\mathrm{LiTaO_3}} - b\cdot x(1-x). \tag{4.7}$$

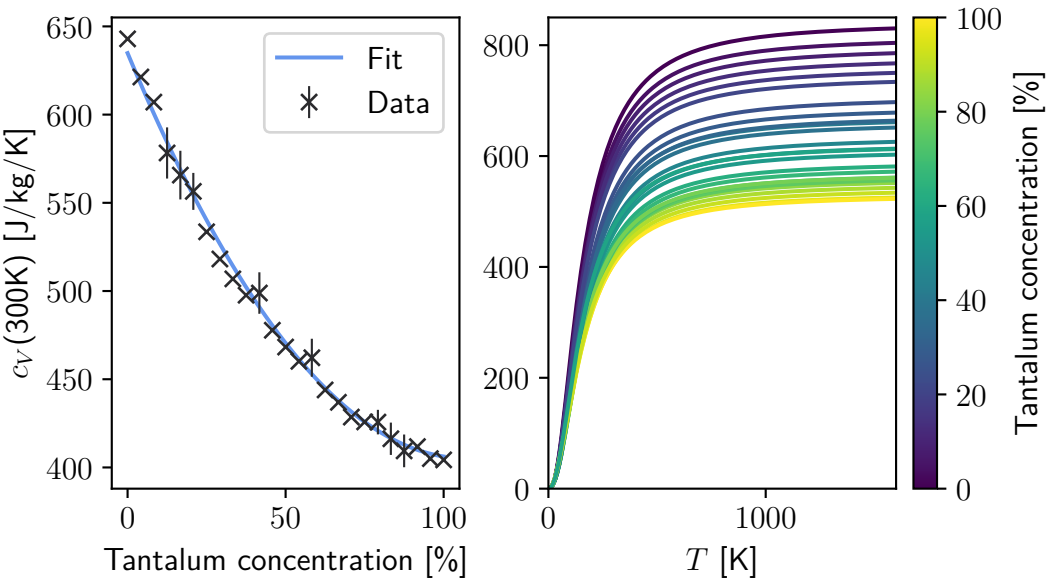

Figure 35: Right panel: specific heat capacity at constant volume as a function of temperature and composition of LNT. Left panel: specific heat capacity at constant volume at 300 K as a function of the Ta concentration.

These bowing parameters have been determined from a few, ordered compositions to 0.6 eV and 0.3 eV for the direct band gap calculated within the IPA and Independent Quasiparticle Approximation, respectively [116]. Again, the application of SQS promises to identify this behaviour more precisely.

Compared to the end compounds LN and LT, the LNT solid solutions feature the same flat dispersion. The direct electronic band gap always occurs at the Γ-point, independent on the mixing ratio. Exemplarily, the within DFT calculated band structure for a concentration of x=50 % is shown in Fig. 36. The band structure is unfolded using the formulation of Eq. (3.9) that has been used in chapter 3.6.

The extracted direct and indirect electronic band gaps are shown in Fig. 37: Here, bowing parameters of 0.38 eV and 0.34 eV are determined for the direct and indirect band gaps, respectively, which are in qualitative agreement to Ref. [116]. The minimal indirect band gap occurs at around 32 %. A closer examination of the DOS reveals that the conduction band minimum shifts linearly with the composition, but the valence band maximum remains constant at high tantalum contents, thus expanding the electronic band gap for higher tantalum contents [P5].

Typically, the within DFT calculated band gaps underestimate experimentally determined values. A quasiparticle correction of the energies can be calculated within the GWA. These calculations are performed as implemented in BerkeleyGW [117, 118], using the generalized plasmon-pole model. The electronic ground state is recomputed within QuantumEspresso [119]. Norm-conserving Vanderbilt potentials [120] (given in the PBEsol formulation with the same electronic configurations as described in Sec. 2.10) with a cutoff energy of 100 Ry are used here, whereas the **k**-point meshes have not been changed compared to the previous calculations within VASP.

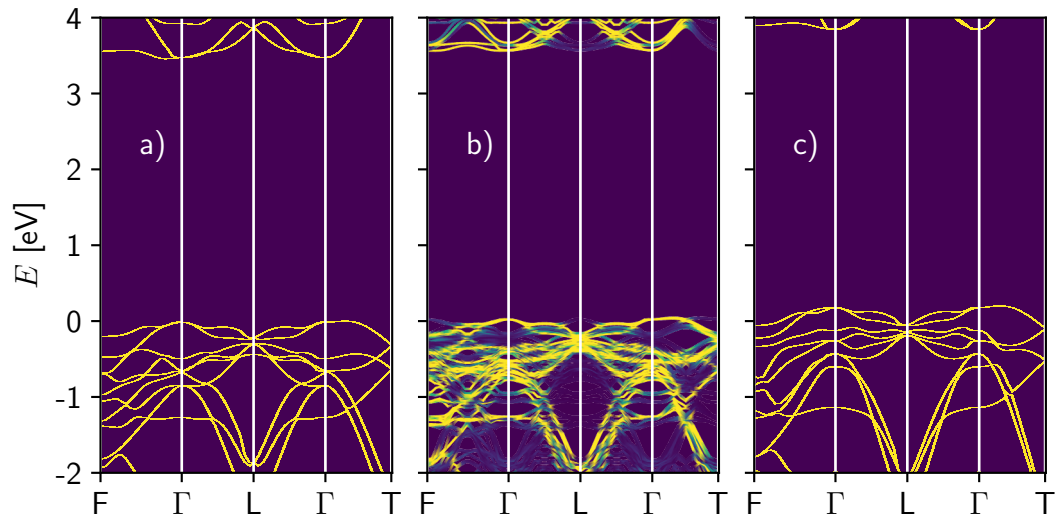

Figure 36: Effective electronic band structure of the LNT crystal family: (a) LN, (b) $LiNb_{0.5}Ta_{0.5}O_3$, and (c) LT. The bands are unfolded to the first Brillouin zone of the primitive unit cell of the end compounds.

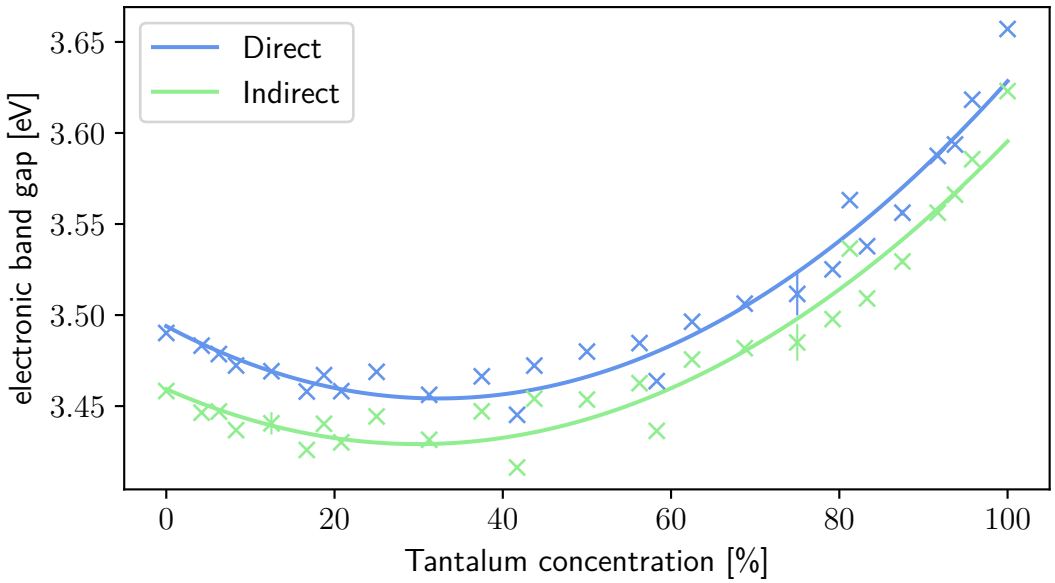

Figure 37: Direct and indirect electronic band gap of the LNT crystal family.

The resulting electronic energies are, within the numerical accuracy of around 5 meV, identical between the two DFT codes. Finally, the quasiparticle corrections are obtained for only 130 bands, which are chosen to be energetically centered around the valence band maximum. The same **k**-point meshes as for the DFT calculations are utilized within the GWA.

The direct band gap in the Independent Quasiparticle Approximation as a function of the composition is shown in Fig. 38. Compared to the DFT calculations, the band gap

broadens, which is the expected behaviour. This broadening is in turn dependent on the tantalum content of the solid solution, which is shown in the lower panel of Fig. 38: Cells containing a higher concentrations of Ta are more affected by the inclusion of quasi-particle effects. The bowing parameter for the direct electronic band gap is, however, only marginally modified to 0.56 eV. The smallest direct band gap is now achieved by a mixed crystal with 21.2 % tantalum content.

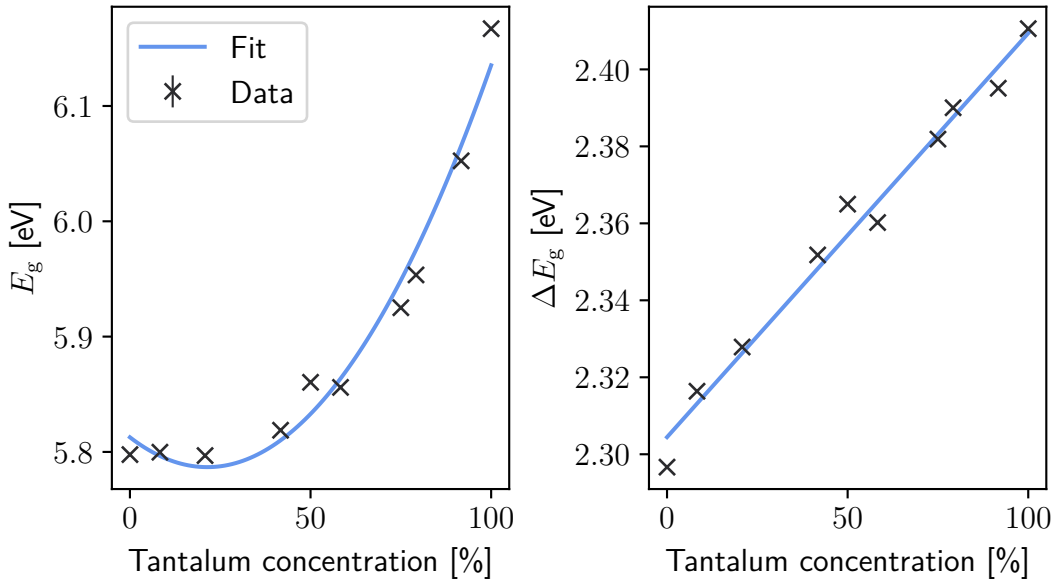

Figure 38: Left panel: Direct electronic bandgap of the $LiNb_{1-x}Ta_xO_3$ solid solutions calculated in the independent quasiparticle approximation (G_0W_0) as a function of the composition. Right panel: Difference of the IPA and IQA bandgap as a function of the composition. Many-body effects affect Ta rich compositions more than Nb rich compositions.

The sublinear behaviour of the electronic band gap is experimentally confirmed by reflectance spectroscopy measurements at low temperatures [P5]. However, since excitonic effects are not taken into account in the simulations, a quantitative comparison is not possible.

4.5 Optical Properties

The optical response of the LNT mixed crystals is calculated using the IPA, as given in Eq. (2.80) and implemented in the QuantumEspresso package [119]. Again, only the fully optimized orthorhombic SQS are considered in this chapter. To ensure a convergence of the sum over empty bands in equation (2.80), a total of 800 bands are included in the calculations. The **k**-point meshes are increased to twice their previously given density for each cell, respectively. The dielectric function is thus converged up to excitation energies of 10 eV, and shown in Fig. 39: Here, the upper row displays the real part (calculated using the Kramers-Kronig relation (2.69)), and the lower row shows the imaginary part. Since the space group R3c has two distinct polarization

axes, each row is further split into the ordinary optical direction (ε_{xx}, or ε_o) on the left side, and the extraordinary direction (ε_{zz}, or ε_e) on the right side.
Again, the main spectral features of LN with two main absorption bands are reproduced (see also for example in Sec. 3.6). LT features a qualitatively similar spectrum compared to LN, however, the spectral signatures are in general shifted to slightly higher energies. This shift corresponds to the larger electronic band gap of LT compared to LN. The spectra of the LNT solid solutions interpolate the spectra of the end compounds, but the overall lowest absorption edge is given by the solid solution of about $40\,\%$ tantalum content, in agreement to the previously observed sublinear behavior of the electronic band gap as a function of the composition. Compared to experimental data, the absorption edge is slightly underestimated for the whole LNT crystal family, in line with the underestimation of the electronic band gap within DFT.

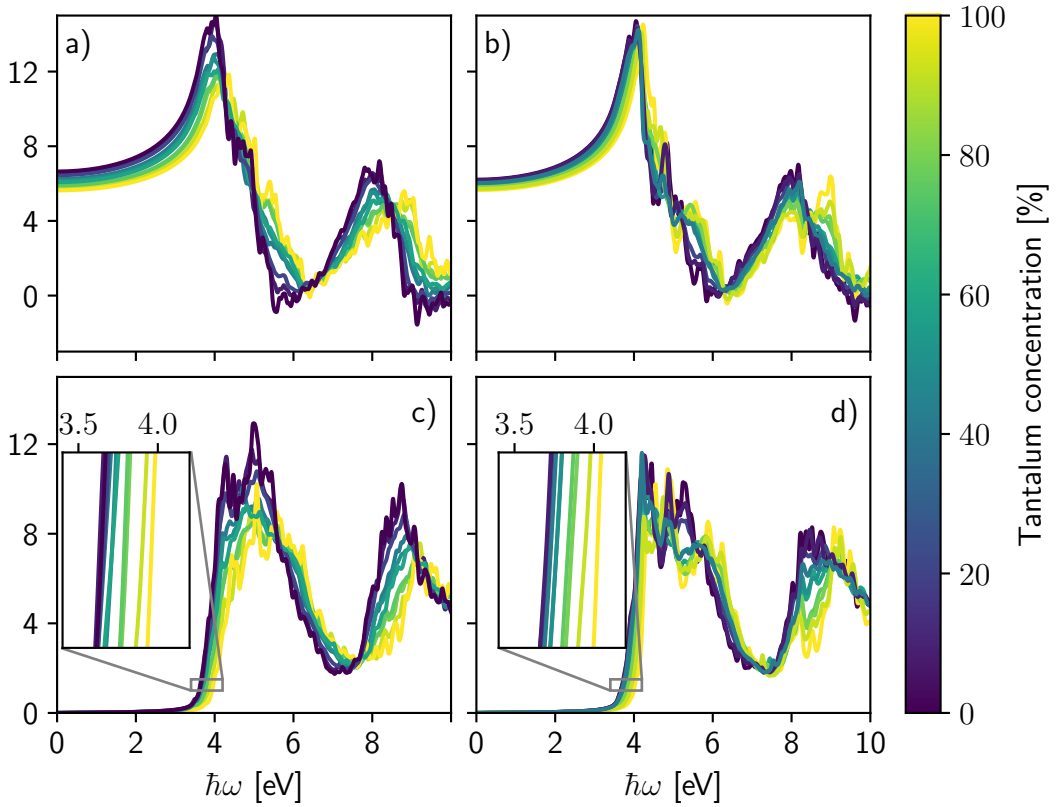

Figure 39: Real (upper row) and imaginary part (lower row) of the dielectric function of ferroelectric $LiNb_{1-x}Ta_xO_3$ solid solutions calculated within DFT in the IPA. The panels at the left and at the right hand side show the ordinary and extraordinary component of the dielectric function, respectively.

To remedy this shortcoming of the DFT, self energy effects can be included e.g. within the GWA. The calculation of the optical spectra for all concentrations is, however, computationally not feasible within the scope of this work. As a first approximation, only the quasiparticle shifts of the electronic energies are calculated in order to estimate the magnitude of the many-body effects, which have already been dis-

cussed in Sec. 4.4. Note, that electron-hole interactions are not considered here. Exemplarily, only the $LiNb_{0.42}Ta_{0.58}O_3$ crystal is discussed, since all other compositions behave very similarly. The quasiparticle energy shifts for each **k**-point with respect to the electronic energy as calculated within DFT is shown in Fig. 40: The energetically higher states are more affected by quasiparticle effects, following a roughly linear trend. Since the upper valence bands show almost no dispersion, their quasiparticle shifts are independent from the **k**-points, resulting in a rigid shift of the valence band edge. On the other hand, the conduction band states show more dispersion, and the quasiparticle shifts thus amplify this dispersion. Moreover, their quasiparticle shifts are stronger compared to the valence band shifts. Still, the conduction bands are quite flat, and, at least in a first approximation, the quasiparticle shift can be considered as almost **k**-point independent. The shift of ca. 2.55 eV of the conduction band edge is in agreement with available literature values [97].
The conduction and valence bands have the same orbital characteristics over the entire Brillouin zone (within a given composition) [P5], providing an explanation for this rigid shift. Thus, instead of explicitly calculating the dielectric function within GWA, a numerically much more convenient scissors shift might prove sufficient to correctly capture many-body effects.

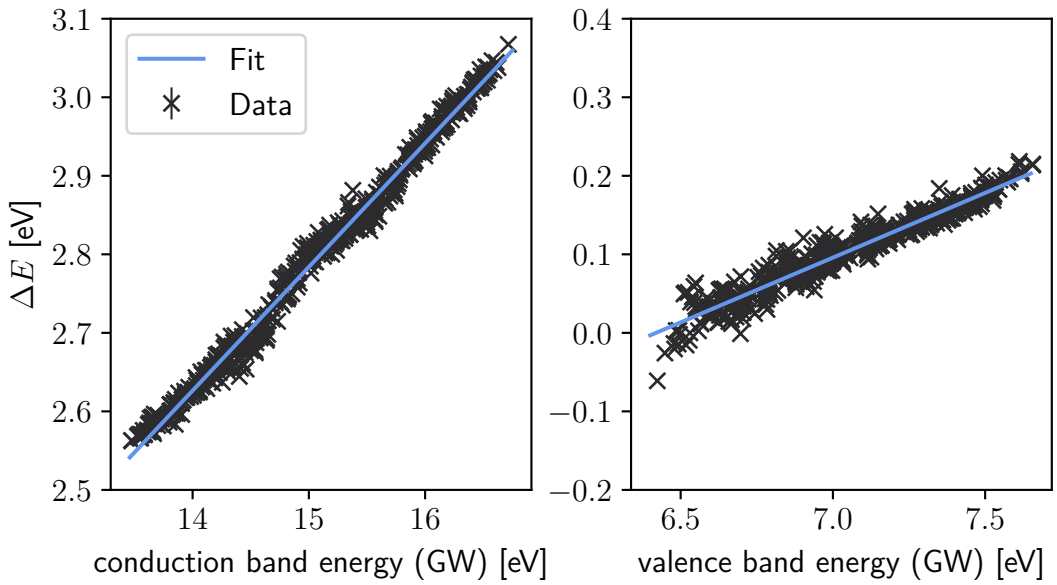

Figure 40: Quasiparticle shifts calculated with respect to the DFT band energies for a ferroelectric $LiNb_{0.42}Ta_{0.58}O_3$ solid solution. The conduction bands (left panel) are more affected by many-body effects than the valence bands (right panel).

4.5.1 Birefringence

Of special interest is the optical birefringence of the LNT solid solutions, defined as the difference between the extraordinary and ordinary refractive indices:

$$\Delta n = (n_e - n_o). \tag{4.8}$$

The birefringence can be exploited in nonlinear optical spectroscopy: Depending on the experimental geometry setup, high signal strengths can be observed for materials with a large birefringence [121]. This allows for a local examination of a crystal sample with high contrasts, concerning for example the imaging of domain walls [P1]. Additionally, if the birefringence of a mixed crystal is known over the whole compositional range, the local composition can be determined [P1]. LN shows a negative birefringence, whereas LT has a positive birefringence. Hence, the birefringence should vanish at a certain tantalum concentration of the solid solution. Since the mixed crystals retain their ferroelectricity for all compositions, the synthetization of a highly unusual ferroelectric that is optically isotropic could be possible [122]. The refractive indizes for the ordinary and extraordinary optical axes can be calculated from the dielectric function using equation (2.73). The birefringence at 633 nm (the wavelength of commonly used helium-neon lasers) as a function of the composition is shown in Fig. 41: A slightly super linear behavior can be observed, which is consistent with experimental [122] and theoretical [97] results. The accidentally-isotropic point is extracted to be x=0.89, which is slightly smaller compared to the value of x=0.94 found by Wood *et al.* [122]. A similar result of x=0.93 has been obtained by measurements on LNT thin films [123].

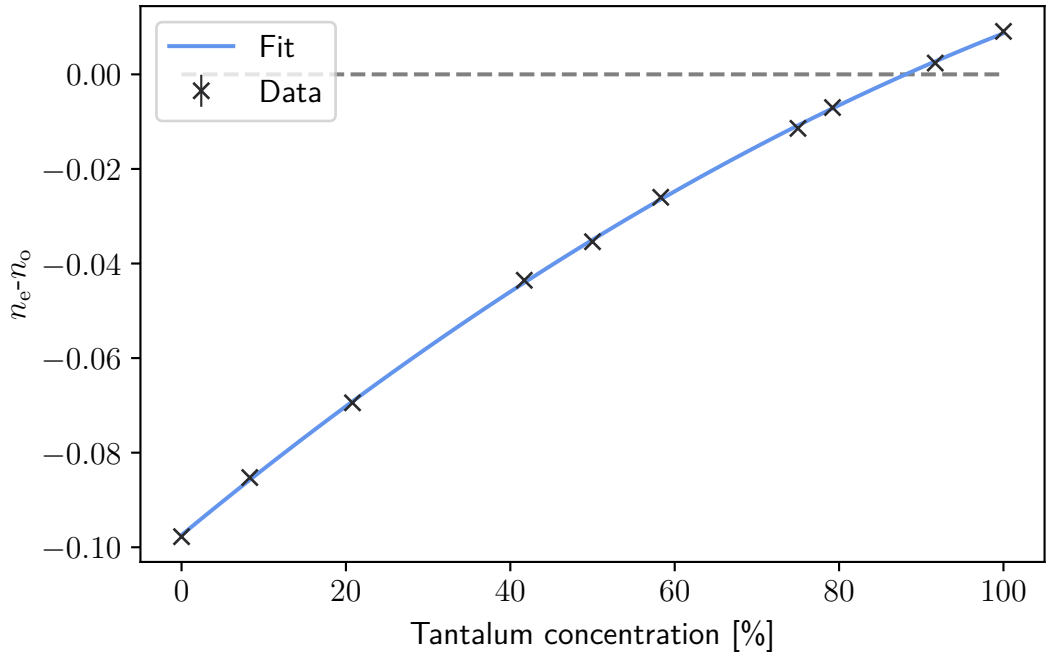

Figure 41: Birefringence of ferroelectric $LiNb_{1-x}Ta_xO_3$ solid solutions as a function of the composition calculated within DFT in the IPA for a laser wavelength of 633 nm.

4.6 Raman & IR spectra

In order to characterize the effects of the tantalum concentration of a LNT solid solution, the knowledge of the dynamical properties of the crystal lattice of the end com-

pounds LN and LT is crucial. Both Raman and IR spectroscopy both yield information regarding the lattice dynamics and thus provide knowledge of many fundamental material properties.
The phonon modes of LN and LT have been extensively studied in the past [50, 51, 93, 124–131], providing a map of spectroscopic signatures to atomic displacement patterns. Despite decades of research, some ambiguities in the assignment of spectral features remain, e.g. regarding the E-TO$_{5,6}$, E-TO$_9$, or E-LO mode frequencies in LN [93, 112, 126, 132]. Additionally, only limited knowledge of the dynamical properties of the LNT solid solutions is available [93, 112, 133]. The usage of SQS for the simulation provides a significant improvement over previous works, since local site deformations are especially important for an accurate simulation of the systems's lattice dynamics.
Since Raman and IR spectroscopy rely on different physical processes, and in turn generally give access to phonon modes of different symmetry, they are often referred to as complementary techniques. In LN and LT, all Raman active modes are also IR active and vise versa, but their scattering efficiencies can be drastically different between the two techniques. Thus, by providing both spectra, a much improved assignment of phonon modes can be achieved.
Both LN and LT crystallize in the point group C_{3v}(3m). According to group theory, their phonon decomposition at Γ can be described by [W15]

$$\Gamma = 4\mathrm{A}_1 + 5\mathrm{A}_2 + 18\mathrm{E},$$

where the E-modes are doubly degenerate. Only the A_1- and E-modes are optically active, whereas the A_2 modes are silent. All A_1- and E-modes further split into LO and TO branches. Overall, 26 spectroscopic signatures[27] are in principle identifiable via Raman and IR spectroscopy. The modes are labeled with respect to their frequencies in ascending order, e.g. E-LO$_6$ refers to the sixth highest frequency E-type symmetry LO phonon.
With knowledge of the Raman tensors, the selection rules (i.e. which modes are observable under a given experimental setup) can be constructed. The Raman tensors of point group C_{3v}(3m) read as [19, 112, 126, 133, W15]

$$\mathrm{A}_1(z) = \begin{pmatrix} a & & \\ & a & \\ & & b \end{pmatrix}, \quad \mathrm{E}(x) = \begin{pmatrix} & c & d \\ c & & \\ d & & \end{pmatrix}, \quad \mathrm{E}(y) = \begin{pmatrix} c & & \\ & -c & d \\ & d & \end{pmatrix}.$$

Consequently, the observable phonons under backscattering geometry can be extracted, which are summarized in Tab. 2.
The scattering configuration is given in Porto's notation: $\mathbf{k}_i(\mathbf{e}_i, \mathbf{e}_s)\mathbf{k}_s$. The vectors $\mathbf{k}_i$ and $\mathbf{k}_s$ denote the direction of the incident and scattered light in crystal coordinates, respectively, and $\mathbf{e}_i$ and $\mathbf{e}_s$ label its electric field orientation, i.e. the polarization, also in crystal coordinates. In backscattering geometry, it holds that $\mathbf{k}_i = -\mathbf{k}_s = \overline{\mathbf{k}_i}$.

[27] These include four A_1-TO and four A_1-LO frequencies, as well as nine E-TO and nine E-LO frequencies

Table 2: Observable phonon modes and Raman tensor elements recorded in back-scattering configuration for point group C_{3v}(3m).

Scattering configuration	Symmetry species	Tensor element TO	LO
$x(y,y)\overline{x}$	A_1-TO, E-TO	a^2+c^2	
$x(y,z)\overline{x}$	E-TO	d^2	
$x(z,y)\overline{x}$	E-TO	d^2	
$x(z,z)\overline{x}$	A_1-TO	b^2	
$y(x,x)\overline{y}$	A_1-TO, E-LO	a^2	c^2
$y(x,z)\overline{y}$	E-TO	d^2	
$y(z,x)\overline{y}$	E-TO	d^2	
$y(z,z)\overline{y}$	A_1-TO	b^2	
$z(x,x)\overline{z}$	A_1-LO, E-TO	c^2	a^2
$z(x,y)\overline{z}$	E-TO	c^2	
$z(y,x)\overline{z}$	E-TO	c^2	
$z(y,y)\overline{z}$	A_1-LO, E-TO	c^2	a^2

For IR spectrocopy, the selection rules are simpler: The dielectric tensor of LN and LT has only two independent components. Thus, only the A_1-type symmetry phonons are excited if the incident and scattered light is polarized parallel to the extraordinary crystal axis (z-axis), i.e. **E** $\parallel$ **z**. In contrast, only the E-type symmetry phonons are observable if **E** $\parallel$ **x** or **E** $\parallel$ **y**. The selection rules for IR spectroscopy are summarized in Tab. 3.

Table 3: Observable phonon modes for light polarization (electric field) with respect to the crystal axes of LN or LT.

Light polarization (E-field)	Symmetry species
E $\parallel$ **z**	A_1
E $\parallel$ **y**	E
E $\parallel$ **x**	E

Strictly speaking, these selection rules only apply to stoichiometric LN and LT. For the mixed crystals (or indeed for congruent crystals) all symmetries are lifted and all optical modes are formally Raman and IR active in all scattering configurations. Further, a larger unit cell is needed in order to describe these solids. In turn, a larger number of phonons will be present at the Γ-point which naturally leads to a broadening of the spectrum. Nevertheless, the spectral features are assigned in the same manner as for LN and LT, labeling the peaks as single modes according to their closest phononic analogue in the end compound. To distinguish this different behaviour, the modes are denoted with a prime, e.g. A_1'-TO_1 denotes the peak that behaves similar in terms of selection rule to the A_1-TO_1 mode in either end compound.
Phonon eigenmodes, eigenfrequencies and effective charges are calculated within density functional perturbation theory (DFPT). The dielectric function is calculated within the IPA using Eq. (2.80). The rhombohedral SQS as introduced in chapter 4.1

are used for the calculations. 54 conduction bands per unit cell are considered to obtain a dielectric function converged up to 10 eV. The Raman and IR-spectra (or rather the ionic contribution to the dielectric function) are finally calculated using Eqs. (2.86) and (2.83), respectively. As SQS unit cells of the same Nb/Ta ratio are not unique, their *de facto* equivalence regarding the resulting spectra needs to be verified first. Three different orthorhombic SQS with an arbitrarily chosen Ta-content of 70.8 % are selected for this test calculation, and their Raman spectra are compared in Fig. 42. Only minimal disparities between the different cells are observed, confirming that all SQS well describe the same material. Therefore, only one SQS of a given Ta-content is used as a reference. Each mode only contributes as a delta peak to the spectrum in the methodology described in chapter 2.8. The experimental data, however, feature a finite linewidth, due to thermal effects, resolution limits, and crystal defects. For a better visual comparison, an artificial gaussian smearing of 5 cm^{-1} width (matching a typically measured line width) is applied to the simulated spectra for both, IR- and Raman.

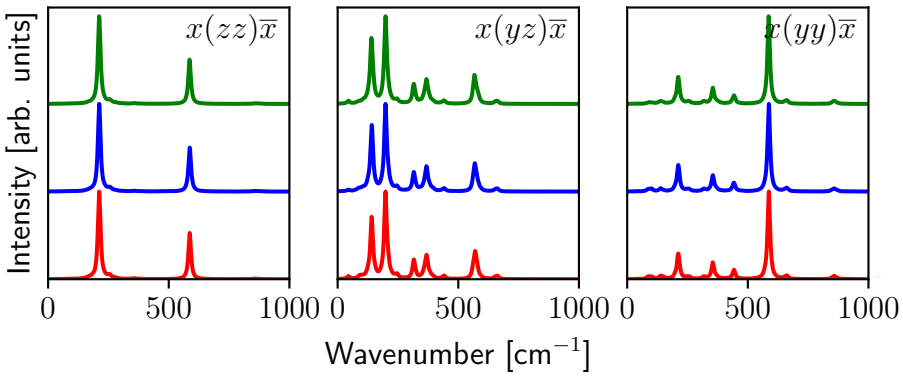

Figure 42: Calculated Raman spectra for three distinct SQS with 70.8 % Ta-content in $x(zz)\overline{x}$, $x(yz)\overline{x}$, and $x(yy)\overline{x}$ configuration (from left to right, using Porto's notation). Each color represents the spectra of a distinct SQS.

The imaginary part of the ionic contribution to the dielectric function can easily be analyzed: Each peak corresponds to a TO-phonon mode that is observable under the given selection rules. This is particularly useful to separate the A_1-TO and E-TO frequencies, by computing (or measuring) both, **E** $\parallel$ **z** and **E** $\parallel$ **y**. For the mixed crystals, each peak corresponds to a multitude of modes that are superimposed by the applied smearing. The real part, however, is more difficult to interpret: According to the Kramers-Kronig relations given in Eq. (2.84), each peak in the imaginary part corresponds to a zero-crossing from positive to negative (downward slope) in the real part. In experiments, the zero-crossing from negative to positive (upward slope) is described by the high frequency end of a phonons Reststrahlenband, which determines a modes LO frequency [P3]. In the simulations, no information regarding the LO frequencies enter for the calculations of the real part of the ionic contribution to the dielectric function, and thus a quantitative comparison to experiment is hindered. Nevertheless, a qualitative visual comparison to experimental data is still possible (see

e.g. Ref. [P3]). The IR spectra for backscattering geometry are given in Fig. 43 for different Ta concentrations.
In **E** ∥ **z** polarization, all A_1-TO modes are in principle observable. However, two peaks at around 202-242 cm^{-1} and 582-609 cm^{-1} dominate the spectra for the whole crystal family. These peaks are assigned to the A_1-TO_1- and A_1-TO_4-like modes, respectively. Additionally, a weak peak at around 334-360 cm^{-1} can be assigned as the A_1-TO_3-like mode. The A_1-TO_2 mode is almost IR silent and not visible in the spectra.
In contrast, only E-TO modes are observable under **E** ∥ **y** polarization. Here, the E-TO_1-, E-TO_3-, E-TO_4-, E-TO_5-, and E-TO_8-like modes dominate the spectra at frequencies in the ranges of 140-149 cm^{-1}, 245-258 cm^{-1}, 313-317 cm^{-1}, 353-363 cm^{-1}, and 569-579 cm^{-1}, respectively. For small tantalum concentrations, the E-TO_2-, E-TO_7-, and E-TO_9-like modes are also visible, however, their intensities decrease with decreasing niobium content of the crystal. The E-TO_6-like modes cannot be observed and are quasi IR-silent.
For both polarization directions, some shoulders can be seen in the spectra of the mixed crystals (e.g. at the left side of the A_1-TO_4-like peaks, highlighted with an asterisk for a concentration of $50\,\%$ Ta content): Such shoulders are not visible in the measured spectra [P3], and might be an artifact of the SQS. This effect could be remedied by employing larger unit cells, which is computationally very challenging. On the other hand, the spectra for the mixed crystals are significantly broader in experiments, such that these shoulders might not be resolved.
The computed Raman spectra can be found in Fig. 44. The simulation is limited to the $x(\cdot,\cdot)\overline{x}$ configurations, since the Raman intensities of LO-modes are not calculated. Similar to the imaginary part of the ionic contribution of the dielectric function, each peak corresponds to a TO phonon mode in the end compounds LN and LT, and to a superposition of modes in the mixed crystals.
In $x(zz)\overline{x}$ configuration, the Raman spectrum looks almost identical to the IR spectrum for **E** ∥ **z** polarization: The two main peaks can be assigned as A_1-TO_1- and A_1-TO_4-like modes. Similarily, the peaks corresponding to the A_1-TO_3-like modes are barely visible. But additionally, the peaks at 256-272 cm^{-1} can be assigned as A_1-TO_2-like. This is especially useful for experiments, where a combination of IR- and Raman spectroscopic measurements for these two polarization combinations yields all A_1-TO-like modes, with redundancies in the A_1-TO_1, A_1-TO_3, and A_1-TO_4-like frequencies.
Analogously to the **E** ∥ **x** polarization direction in IR spectroscopy, only E-TO-like modes are observable for $x(yz)\overline{x}$ configuration. Again, most peaks can be similarly assigned, but with some notable differences: The E-TO_5-like modes are almost completely Raman silent. Instead, the E-TO_6-like modes are observable. This is opposite to the behaviour observed for the IR-spectra, where the E-TO_6-like modes are quasi-silent. Also, the E-TO_9-like modes are only observable for high tantalum concentrations in the crystal. Again, this is opposite to the IR-spectra, where these modes are only observable for low tantalum content.
Formally, the $x(yy)\overline{x}$ configuration does not yield any new information: All A_1-TO- and E-TO-like modes have already been assigned. Nevertheless, showing this configuration allows for a more complete comparison to experiments, where each addi-

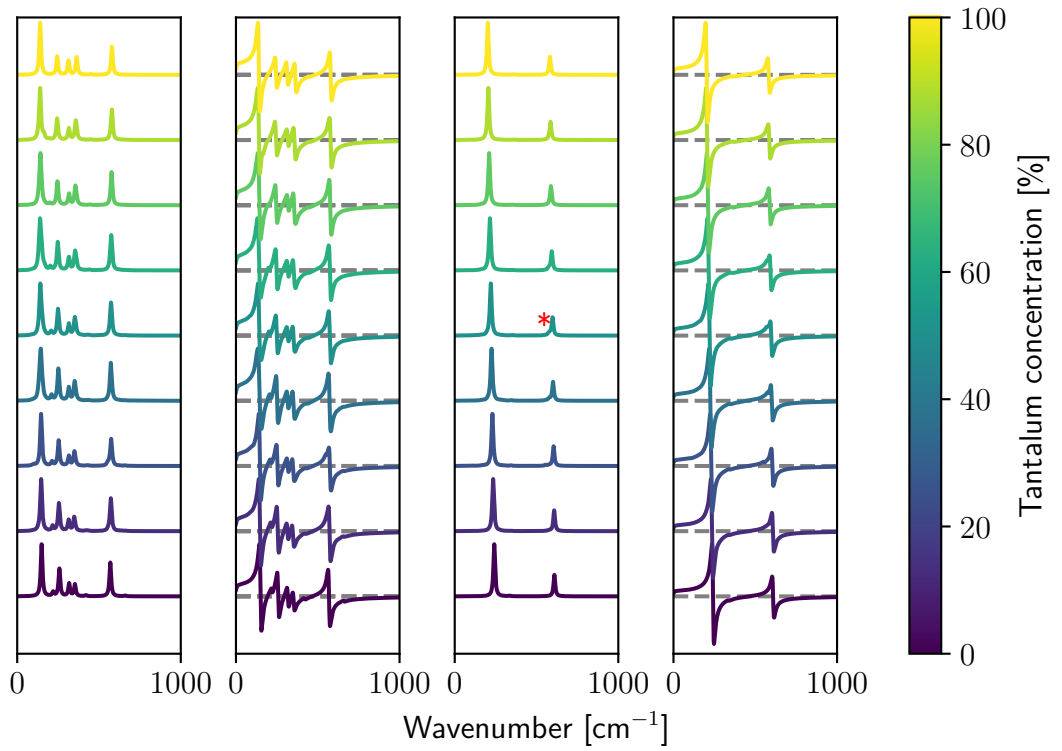

Figure 43: The ionic contribution of the dielectric function for **E** ∥ **x** (left), and **E** ∥ **z** (right) in the LNT crystal family. In both cases, the imaginary part (lhs) and real part (rhs) are plotted.

tional measurement yields more redundancies to the data. Curiously, an additional feature arises for the mixed crystals at around 864-872 cm^{-1}: These peaks correspond to an A_2-TO_5-like mode, which becomes Raman active due to the lifting of symmetries in the SQS. The existence of this peak is confirmed by experiments [P3], however, its interpretation is more complex: The A_2-like modes are only Raman-silent for stoichiometric crystals, i.e. they also appear for congruent LN and LT, and for the mixed crystals, where the symmetries are broken, which has been observed e.g. in Refs. [134, P3]. On the other hand, this peaks position is in close proximity of the A_1-LO_4- and E-LO_9-like frequencies of the LNT crystal family, which might indicate that these modes were not completely suppressed in the measurements. Furthermore, this mode might only be activated by certain SQS, and therefore could be an artifact of the pseudo-random ionic distributions of the simulated cells.
Even though the Raman and IR intensities of the LO modes can not be determined here, their frequencies can be extracted by applying Eq. (2.38). All eigenvectors of the TO and LO modes are then compared in the limit $\mathbf{q} \to 0$:

$$W = \langle e_{\mathrm{TO}}^{\mathbf{q}=0} | e_{\mathrm{LO}}^{\mathbf{q}\to 0} \rangle \,. \tag{4.9}$$

The weights W are calculated for all possible combinations, and a LO mode is assigned to a corresponding TO mode for the maximal value of W (typically W >0.8). Thus, a LO frequency can be related to its TO analogon with high certainty. If no

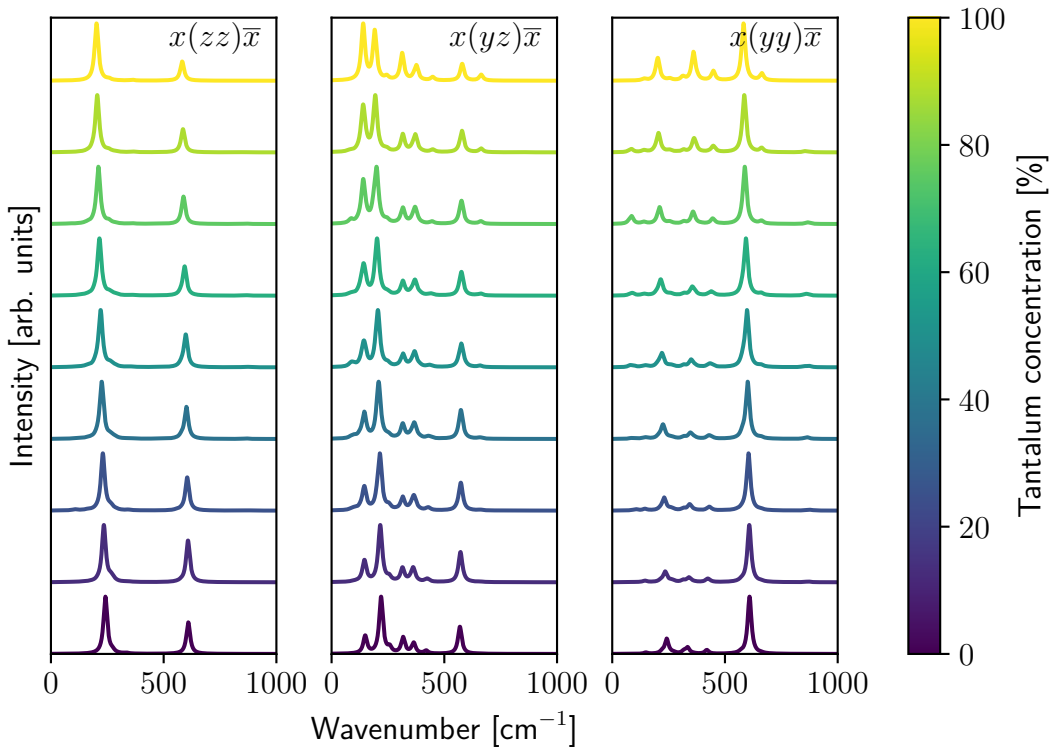

Figure 44: Calculated Raman spectra for the LNT crystal family in $x(zz)\overline{x}$, $x(yz)\overline{x}$, and $x(yy)\overline{x}$ configuration (from left to right, using Porto's notation).

reasonable match is found, the LO frequency is estimated by fitting a low-order polynomial with respect to similar phonon modes for cells of a different tantalum concentration.

Generally, the phonon frequencies in LT are slightly smaller compared to LN, which can be explained by the difference of the atomic masses of Nb (92.906 a.u.) and Ta (180.948 a.u.). For some modes the reverse statement is true: These modes feature an overall movement of the oxygen cage (deformations and rotations, e.g. A_1-TO_3 and high frequency E-modes). Here, the shorter Ta-O bond length compared to Nb-O implies a stronger bond, resulting in higher mode frequencies for such displacements. The phonon frequencies are plotted in Figs. 51, 52, 53 and 54, and summarized in Tabs. 7, 8 and 9 in the Appendix.

Overall, the calculated phonon frequencies are in good agreement with previous available computational and experimental results [93, 126, 132, 135]. Typically, with the PBEsol functional optimized lattice constants tend to slightly overestimate the experimental values, which in general leads to an underestimation of the phononic frequencies. Therefore, the calculations shown here display a slightly worse agreement to experiments than previous simulations that used lattice constants extracted from experimental data [P3].

4.6.1 Lyddane-Sachs-Teller Relation

Throughout this work, the dielectric function has been calculated for incoming photons of different wavelengths. Both, the ionic and electronic contributions have been considered. However, its static limit ε_{st} is much more difficult to compute [136, W11]. Using the generalized Lyddane-Sachs-Teller relation (LST), an estimate of ε_{st} is given by the ratio of the LO- and TO phonon frequencies multiplied by the high frequency dielectric function ε_∞:

$$\varepsilon_{\text{st}} = \varepsilon_\infty \prod_{j=1}^{n} \frac{\omega_{\text{LO}j}^2}{\omega_{\text{TO}j}^2}. \tag{4.10}$$

Again, harmonic phonons are assumed, such that phononic dissipations are neglected in the above formulation. Also, only the A_1- and E-like modes are considered, even though formally all phonon frequencies feature LO-TO splitting in the mixed crystals. Inserting the phonon frequencies from Tabs. 7, 8 and 9 into Eq. (4.10) leads to the values reported in Fig. 45: For LN, values of 40.48 and 28.77 are extracted for the static contribution to the dielectric function for z- and x-cut, respectively. Both values are in good agreement to literature [81, 112, 126, 137, 138]. Similarly, the extracted values for LT are in agreement to experimental data [139], as well as simulations [112]. Note, that DFT tends to overestimate ε_∞, such that the calculated values for ε_{st} are expected to be slightly larger compared to measurements (since the LO-TO splitting ratios are well reproduced).

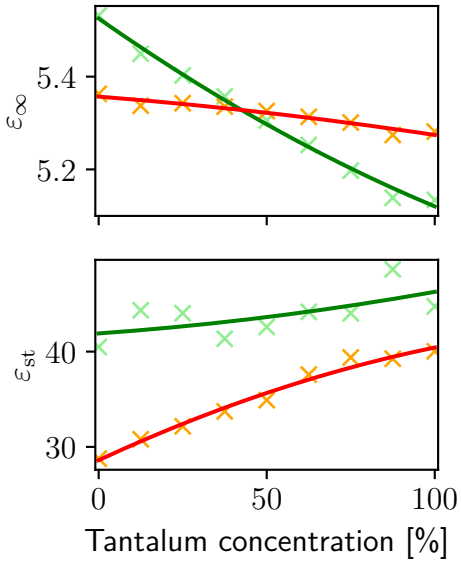

Ta [%]	ε_∞		ε_{st}	
	z-cut	x-cut	z-cut	x-cut
0.0	5.53	5.36	40.48	28.77
12.5	5.45	5.34	44.34	30.81
25.0	5.40	5.34	44.03	32.16
37.5	5.36	5.34	41.35	33.73
50.0	5.31	5.33	42.59	34.91
62.5	5.25	5.32	44.17	37.59
75.0	5.20	5.30	44.02	39.38
87.5	5.14	5.27	48.63	39.25
100.0	5.13	5.28	44.74	40.03

Figure 45: ε_∞ (top) and ε_{st} (bottom) as a function of tantalum content of the LNT crystal family. The values for ε_{st} are obtained using the LST relation [Eq. (4.10)], whereas ε_∞ is obtained by DFPT calculations. Only polarizations $\mathbf{E} \parallel x$ (green) and $\mathbf{E} \parallel z$ (red) are considered.

4.6.2 Spontaneous Polarization

Another physical property that can be derived from the quantities calculated in this chapter is the spontaneous polarization: The polarization axes of the LNT crystal family lies parallel to z, such that only the dipole moment in that particular direction needs to be taken care of. Analogously to Eq. (2.81) the effective charges are summed up, however, in this case the phononic displacements are replaced by the distance u_i of the ions with respect to their paraelectric, high-symmetry positions (compare e.g. with figure 34):

$$P_S = \frac{1}{V} \sum_i Z^*_{i33} u_i. \tag{4.11}$$

Since the oxygen ions have the same equilibrium positions in the ferro- and paraelectric phases, only the displacements of the Li, Nb, and Ta ions are considered. Note, that the displacement distance of these ions is dependent on the tantalum content of the crystal, which has already been shown in Sec.4.2. Furthermore, the local environment of the ions impacts the resulting effective charge. Thus, the magnitude of the effective charges varies by as much as 5 % over the compositional range. The results presented in figure 46 show a linear dependence of the spontaneous polarization as a function of the tantalum content of the crystal. Similarly calculated results, which are only available for the end compounds LN and LT, are in excellent agreement [140, P6]. It is important to mention that the results presented here are only valid for defect free crystals: Considering experimental data, a wide spread of almost 20 % in the measured spontaneous polarization of LN can be observed for stoichiometric crystals (P_S^{sLN} =0.62-0.78 C m^{-2} [57, 141]). These differences are further expanded to over 35 % if congruent crystals are taken into account as well (P_S^{cLN} =0.5-0.8 C m^{-2} [142, 143]). Still, the here calculated value of 0.755 C m^{-2} lies well within those boundaries. A similar behaviour can be observed for lithium tantalate, where the measurements range from P_S^{cLT} =0.5-0.6 C m^{-2} [17, 142, 144, 145]. Again, the in this work predicted value of 0.606 C m^{-2} lies towards the higher end of this spectrum.

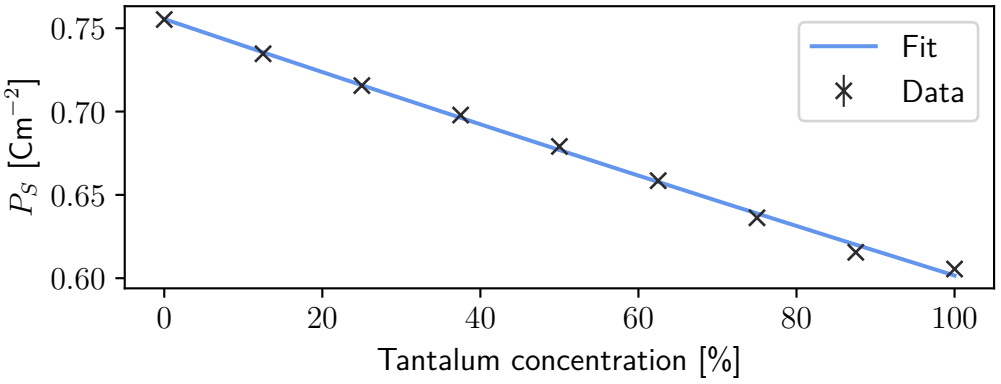

Figure 46: Spontaneous polarization of the LNT crystal family.

5 Conclusions

In this work, the structural, electronic, optical, and thermal properties of lithium niobate ($LiNbO_3$), lithium tantalate ($LiTaO_3$), and lithium niobate tantalate ($LiNb_{1-x}Ta_xO_3$) crystals were investigated using ab initio density functional theory calculations within the PBESol formulation as a baseline. Methodologic extension of the DFT were applied to model the temperature and composition dependence of many material properties. This thesis thus represents a thorough theoretical characterization of the ground and excited state of LNT solid solutions. All results were extensively compared to available experimental and theoretical data.

The main focus of the first chapter was to resolve the role of temperature effects for various material properties of LN and LT. The volumetric thermal expansion was determined by the quasi-harmonic approximation, going beyond the inclusion of only harmonic phonon effects. Even though these results represent an isotropic approximation of the crystal lattice, they served as a crucial step for the following calculations to model the ferroelectric phase transition within the stochastic self-consistent harmonic approximation, where anharmonic phonon corrections are fully included. Here, an exceptionally good agreement between the calculated and measured Curie temperatures of LN and LT was achieved. This agreement could clearly be traced back to the inclusion of anharmonic phonon effects, demonstrating the shortcomings of the harmonic phonon approximation at elevated temperatures, or indeed for at $0\,\mathrm{K}$ metastable phases such as the paraelectric structures of LN and LT. The simulated specific heat capacities at constant volume or pressure yielded further information regarding the phase transition: Here, the specific heat capacity at constant pressure shows a sharp decrease at the transition temperature, which is clearly visible in experiment. A closer look at the temperature dependent thermal transport too shows a distinct jump at the phase transition. This effect was traced back to the different phonon lifetimes between the ferro- and paraelectric phases, whereas the phonon group velocities, as well as the specific heat capacity at constant volume show almost no distinction between the two phases. Unfortunately, this step like increase is not confirmed in the experiment, which only show a delta-like peak at the Curie temperature.
The anisotropic thermal expansion, elastic coefficients, piezoelectric coefficients, and sound velocities as a function of temperature were extracted using machine-learned force fields. These force fields were trained on the structures created during the runtime of the SSCHA calculations, i.e. on DFT level calculations. By fine-tuning the training parameters, a numerical error similarly small as the numerical DFT errors was achieved for the force fields. This enabled to calculate the abovementioned physical properties at almost DFT-level accuracy, but with only a fraction of the numerical costs. By falling back to the harmonic approximation for phonons, only the lower-

temperature regimes of the ferroelectric phases could be correctly reproduced. Still, a remarkable agreement to experiments for the simulated lattice constants as a function of temperature was achieved, clearly depicting the different and non-trivial behavior of the different lattice constants: Whereas the lattice constant a_{H} (perpendicular to the spontaneous polarization) is steadily increasing with an increase in temperature, the lattice constant c (parallel to the spontaneous polarization) features a more complex behavior by increasing at lower temperatures and decreasing thereafter. This latter decrease could be partially traced back to the high-frequency A_1-TO_4 mode, which only activates at higher temperatures and favors a contraction along the polarization axis. The elastic and piezoelectric moduli compare well to measurements at room temperature, but fail to predict the correct behavior near the phase transition, due to the afformentioned neglect of anharmonic phonon effects.
Lastly, the effect of Li deficiencies on the optical absorption edge in LN was discussed: LN is typically grown in a congruent, Li deficient composition, and further Li outdiffusion at elevated temperatures occurs. To correctly capture the electronic d-states of Nb, a Hubbard correction was applied, and the dielectric function was extracted from the resulting Kohn-Sham wavefunctions. Here, it could be shown that a simplified Li-vacancy model already correctly captures the trend of the absorption edge shift as a function of the composition, compared to the more realistic, more complex Li-vacancy model. This trend is traced back to the closing of the electronic band gap with an increase in Li vacancies. The additional localized conduction band present in the more realistic Li-vacancy model is, however, not present in this simplified, non charge compensated model.

In the second chapter, the LNT solid solutions were investigated. Previously created special quasi-random structures were utilized to approximate the random alloys within periodic boundary conditions. These SQS were fully optimized within DFT, yielding the structural dependence of the lattice constants and ionic positions as a function of the composition. The dependence of an alloys properties on its composition can often be described using the empirical Vegard law, which here only holds for the in-plane lattice constant a_{H} and the bulk modulus for LNT. Further, a clear distinction between the ionic positions with respect to the composition could be observed, underlying the importance of local-site effects present within the SQS approach.
The electronic band gap similarly shows a clear deviation from Vegard's law, denoting a minimal band gap for a composition of 32 % tantalum. This value is shifted to 21 % if instead of DFT the GW approximation is used. This shift is almost uniform for all energies and k-points, allowing for the bypass of the numerically challenging GWA calculations by a simple scissors-shift. The sub-linear behavior of the electronic band gap expands to the optical band gap as well, as has been determined from the dielectric function. The latter was used to determine the birefringence, which shows a highly unusual possibility for a ferroelectric, optical isotropic crystal at around 90 % tantalum content.
Lastly, the composition dependent Raman and IR spectra were calculated and extensively discussed with respect to selection rules and observed phonon modes. Here, a linear dependence of almost all phonon modes as a function of the composition

could be observed. Additionally, the Raman spectra for the $x(yy)\overline{x}$ show an additional peak for the solid solutions, which is not visible for the end compounds: This peak's appearance was traced back to the activation of modes due to symmetry breaking within the solid solutions, which does not occur for LN and LT. Using the extracted phonon frequencies, the static limit of the dielectric function was determined using the Lyddane-Sachs-Teller relation. Finally, with knowledge of the ionic effective charges and their displacement from the high-symmetry paraelectric phase, the spontaneous polarization was determined as a function of the composition. Here, a roughly linear dependence on the composition is predicted.

This work thus provides a broad overview on the material properties of LN and LT, with particular emphasize on their temperature-dependent behavior. The LNT crystals were extensively analyzed to characterize their composition-dependent ground-state properties, focusing on deviations and similarities compared to the parent compounds.

5.1 Outlook

The here presented results offer a lot of possibilities for follow-up investigations: With regards to the research on different physical phenomena, the modeling aspects covered in this work serve as a foundation for more complex systems. Further, the theory level on which such modeling is based upon needs to match a certain precision in order to correctly capture real phenomena. In some cases, models can be significantly simplified by neglecting higher-order interactions, while in other cases a low-order approach does not provide sufficient accuracy. Both such possibilities can be referenced from the results presented here. Lastly, the verification by experimental measurements is essential for scientific knowledge gain.

Modeling

Here, only stoichiometric or defect free systems have been investigated. Particularly for the LNT crystal family however, intrinsic defects are always present in real crystals. Further, LN and LT are commonly doped to enhance favorable material properties. Thus, the results presented in this work represent the most simplistic structures, and can only serve as a starting point for further analysis.

An important step to simulating the behavior of defect structures in LNT lies in the determination of formation energies within the mixed crystals, to identify possible atomistic defect configurations.

Of particular interest at elevated temperatures are lithium and hydrogen diffusion effects, and significant strides have already been made for LN [146, 147, P7], but similar simulations for the LNT solid solutions have not been performed yet.

Ferroelectric domain walls attract attention, since they are especially suited for novel applications due to their electronic conductivity and optical properties. Within the FOR5044, only domain walls of end compounds LN and LT have been studied by numerical simulations so far [148, 149].

Many more fascinating possibilities to exploit the properties of LNT for novel devices exist, ranging from thin film heterojunctions [150], to acoustic devices [P8], or integrated wave guides [151], just to name a few. Further prospects include strain-tunable devices which combine and expand the afformentioned concepts [152, 153]. Again, mostly the end compounds have been studied as of yet, and investigations on the LNT mixed crystals, especially with regards to numerical modeling, are virtually non-existent.

Methodology

Most numerical simulations suffer from oversimplifications in the underlying models in order for results to be computable at all. Keeping the computational limits in mind, significant strides could be achieved by exploring the machine-learned force field ansatz further, for example by expanding their applicability to the LNT solid solutions. The machine learned force field ansatz is particularly promising for tackling such large systems, but could even enable to compute more refined SQS (i.e. larger supercells), but also defect structures, domain walls, surfaces, etc., since their accuracy is (almost) on par with state of the art DFT calculations.

The here presented approach mostly relies on harmonic phonons in order to calculate thermal properties or spectroscopic signatures, while also showcasing the shortcomings of this simplification. The inclusion of anharmonic phononic effects is currently not feasible within DFT, especially for extended systems. Here, the abovementioned force fields could bridge the gap between numerical and theoretical accuracy versus computational cost.

With regards to the electronic system, in particular the optical calculations could be significantly improved by more sophisticated methods, such as time-dependent DFT, full GWA, or the Bethe-Salpeter ansatz, where only the latter explicitly inlcudes important electron-hole interactions. Moreover, the non-linear optical properties of the LNT mixed crystals remain unexplored, whereas especially LN has been focused by many recent investigations [154, 155].

Comparison to Experiment

The growth of high-quality LNT crystals remains a challenge due to the vastly different melting points of LN (1500 K) and LT (1900 K) [156], and sufficiently large crystals have only been reported by a few scientific groups [122, 157–159]. Further, high-temperature measurements are notoriously difficult to perform, due to the limited thermal operating ranges of required instruments, and chemical degradation of the samples. Accurate measurements on high-quality LNT crystals at elevated temperatures are therefore a top priority within the FOR5044 research unit.

A Appendix A: Methodology

A.1 State Variables from Harmonic Phonons

Using the partition function for harmonic phonons as introduced in Sec. 2.5.4, one can derive a multitude of state variables:

$$\begin{aligned} F &= -k_\mathrm{B}T \ln \mathcal{Z} \\ &= \sum_{\mathbf{q},\nu} \left[\frac{1}{2}\hbar\omega(\mathbf{q},\nu) + k_\mathrm{B}T \ln\left(1 - e^{-\frac{\hbar\omega(\mathbf{q},\nu)}{k_\mathrm{B}T}}\right)\right] \end{aligned} \tag{A.1}$$

$$\begin{aligned} S &= -\frac{\partial F}{\partial T} \\ &= -\sum_{\mathbf{q},\nu} k_\mathrm{B} \ln(1 - e^{-\hbar\omega(\mathbf{q},\nu)/k_\mathrm{B}T}) - \frac{1}{T}\frac{\hbar\omega(\mathbf{q},\nu)}{e^{\hbar\omega(\mathbf{q},\nu)/k_\mathrm{B}T} - 1} \end{aligned} \tag{A.2}$$

$$\begin{aligned} U &= -\frac{\partial \ln \mathcal{Z}}{\partial \ln T} \\ &= \sum_{\mathbf{q},\nu} \frac{1}{2}\hbar\omega(\mathbf{q},\nu) + \frac{\hbar\omega(\mathbf{q},\nu)}{e^{\hbar\omega(\mathbf{q},\nu)/k_\mathrm{B}T} - 1} \end{aligned} \tag{A.3}$$

$$\begin{aligned} c_V &= \left.\frac{\partial U}{\partial T}\right|_V \\ &= \sum_{\mathbf{q},\nu} k_\mathrm{B} \left(\frac{\hbar\omega(\mathbf{q},\nu)}{k_\mathrm{B}T}\right)^2 \frac{e^{\hbar\omega(\mathbf{q},\nu)/k_\mathrm{B}T}}{(e^{\hbar\omega(\mathbf{q},\nu)/k_\mathrm{B}T} - 1)^2} \end{aligned} \tag{A.4}$$

$$p = -\frac{\partial F}{\partial V} = T\frac{\partial S}{\partial V} \tag{A.5}$$

$$\begin{aligned} c_p &= \left.\frac{\partial H}{\partial T}\right|_p = p\frac{\partial V}{\partial T} + \frac{\partial U}{\partial T} \\ &= T\frac{\partial S}{\partial V}\frac{\partial V}{\partial T} + c_V \end{aligned} \tag{A.6}$$

$$\begin{aligned} f_0 &= k_\mathrm{B}T\frac{1}{\mathcal{Z}}\left.\frac{\partial \mathcal{Z}}{\partial \mu}\right|_{\mu=0,V,T} \\ &= \frac{1}{e^{\hbar\omega(\mathbf{q},\nu)/k_\mathrm{B}T} - 1} \end{aligned} \tag{A.7}$$

B Appendix B: LN & LT

B.1 Unit Cell Conversion

The lattice parameters of the primitive rhombohedral unit cell can be transformed to the conventional hexagonal unit cell, as well to the orthorhombic unit cell, by simple geometric considerations:

$$
\begin{aligned}
a_{\mathrm{H}} &= 2a_{\mathrm{R}}\sin(\alpha/2),\\
b_{\mathrm{O}} &= 2\sqrt{3}a_{\mathrm{R}}\sin(\alpha/2) = \sqrt{3}a_{\mathrm{H}},\\
c &= a_{\mathrm{R}}\sqrt{4\sqrt{\frac{\cos(2\alpha)+1}{\cos(\alpha)+1}}\cos(\alpha/2)+2\cos(\alpha)+3},\\
\alpha &= 4\arctan\left(\sqrt{\frac{(c/a_{\mathrm{R}})^2-4\sqrt{3}\sqrt{(c/a_{\mathrm{R}})^2+3}+15}{9-(c/a_{\mathrm{R}})^2}}\right),\\
a_{\mathrm{R}} &= \frac{1}{3}\sqrt{3a_{\mathrm{H}}^2+c^2},\\
\alpha &= 2\arcsin\left(\frac{3}{2}\sqrt{3+\left(\frac{c}{a_{\mathrm{H}}}\right)^2}\right),\\
V_{\mathrm{H}} &= \frac{\sqrt{3}}{2}a_{\mathrm{H}}^2 c,\\
V_{\mathrm{R}} &= a_{\mathrm{R}}^3\sqrt{1-3\cos^2(\alpha)+2\cos^3(\alpha)},
\end{aligned}
$$

where V denotes the unit cell volume of either the rhombohedral (R), hexagonal (H), or orthorhmobic (O) unit cells, and α denotes the angle between the rhombohedral lattice constants a_{R}. All variables given follow the convention outlined in Fig. 8

B.2 Application of Machine-Learned Force Fields

B.2.1 Free Energy Surface

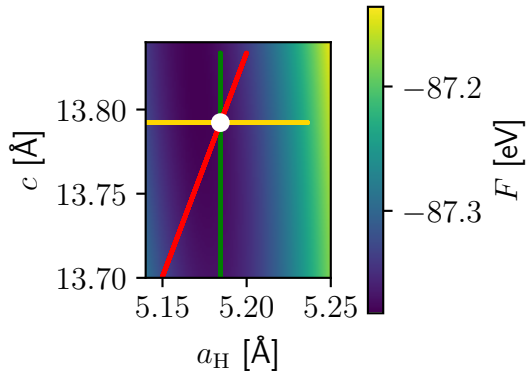

Figure 47: Free energy surface at 300 K of LT. The white point denotes the energetic minimum and defines the equilibrium lattice constants at this temperature. The colored lines denote a straining of the cell according to the strain tensors η_1 (yellow), η_2 (green) and η_3 (red), using the definition from Sec. 3.5.2.

B.2.2 Strain Tensors in Cartesian Coordinates

The in Voigt notation given strain tensors used in Sec. 3.5.2 are represented in cartesian coordinates:

$$\eta_1 = \begin{pmatrix} \eta & 0 & 0 \\ 0 & \eta & 0 \\ 0 & 0 & 0 \end{pmatrix} = \begin{pmatrix} \eta \\ \eta \\ 0 \\ 0 \\ 0 \\ 0 \end{pmatrix}, \eta_4 = \begin{pmatrix} 0 & 0 & 0 \\ 0 & \eta & 0 \\ 0 & 0 & 0 \end{pmatrix} = \begin{pmatrix} 0 \\ \eta \\ 0 \\ 0 \\ 0 \\ 0 \end{pmatrix},$$

$$\eta_2 = \begin{pmatrix} 0 & 0 & 0 \\ 0 & 0 & 0 \\ 0 & 0 & \eta \end{pmatrix} = \begin{pmatrix} 0 \\ 0 \\ \eta \\ 0 \\ 0 \\ 0 \end{pmatrix}, \eta_5 = \begin{pmatrix} \eta & 1/2\eta & -1/2\eta \\ 1/2\eta & \eta & 0 \\ -1/2\eta & 0 & 0 \end{pmatrix} = \begin{pmatrix} \eta \\ \eta \\ 0 \\ 0 \\ -\eta \\ \eta \end{pmatrix},$$

$$\eta_3 = \begin{pmatrix} \eta & 0 & 0 \\ 0 & \eta & 0 \\ 0 & 0 & \eta \end{pmatrix} = \begin{pmatrix} \eta \\ \eta \\ \eta \\ 0 \\ 0 \\ 0 \end{pmatrix}, \eta_6 = \begin{pmatrix} \eta & 0 & -1/2\eta \\ 0 & \eta & -1/2\eta \\ -1/2\eta & -1/2\eta & 0 \end{pmatrix} = \begin{pmatrix} \eta \\ \eta \\ 0 \\ -\eta \\ -\eta \\ 0 \end{pmatrix}.$$

B.2.3 Convergency Tests

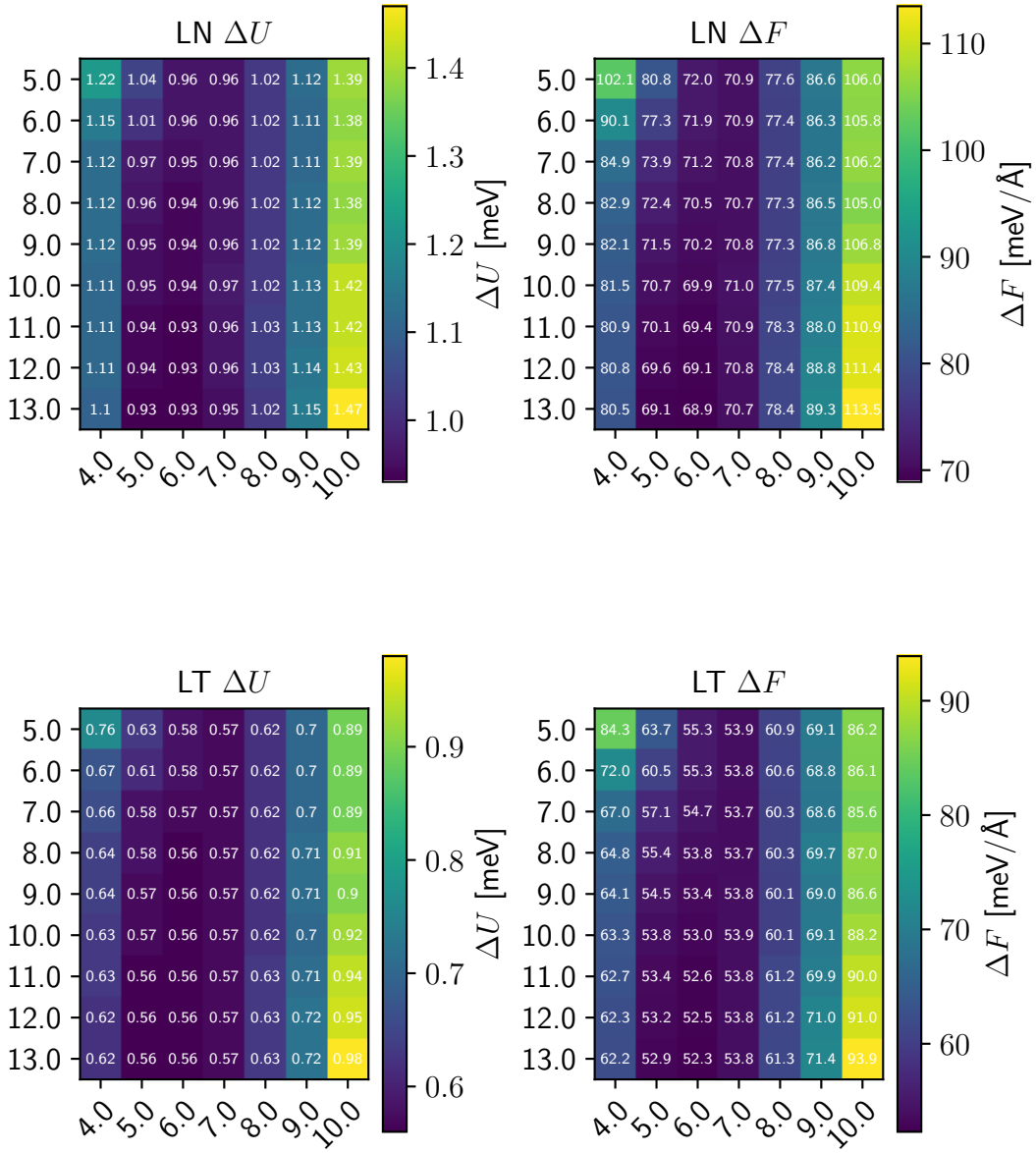

Figure 48: Predicted training set errors as a function of the cutoff radii: The cutoff radius for the pair correlation function and angular correlation function are plotted in units of Å on the y- and x-axis, respectively. The errors for the electronic energy (left), and the root mean square error of the forces (right) are shown for both LN (upper row) and LT (lower row). The chosen cutoff values are 9 Å for the pair correlation function and 6 Å for the angular correlation function for both systems.

B.2.4 Acoustic Group Velocities

propagation direction	polarization direction	group velocity 0K	300K	500K	700K	Exp. [78] [300K]
100	100	6.597	6.139	6.001	5.745	6.560
001	001	6.718	6.626	6.506	6.356	7.351
010	010	6.528	6.136	5.979	5.721	6.832
011	011	6.534	6.186	6.111	6.050	7.366
001	010	3.724	3.299	3.394	3.464	3.598
010	100	3.852	3.387	3.542	3.608	3.951
011	100	3.982	3.490	3.621	3.690	3.998

Table 4: Acoustic sound velocities for different polarization- and propagation directions and temperatures for LN. The group velocities are given in km/s.

propagation direction	polarization direction	group velocity 0K	300K	500K	700K	Exp. [76] [300K]
100	100	5.524	5.323	5.272	5.206	5.552
001	001	6.015	5.845	5.780	5.812	6.161
010	010	5.698	5.495	5.462	5.407	5.692
011	011	6.168	5.949	6.012	6.106	6.239
001	010	3.706	3.566	3.709	3.871	3.604
010	100	3.246	3.145	3.317	3.475	3.530
011	100	3.199	3.138	3.284	3.424	3.409

Table 5: Acoustic sound velocities for different polarization- and propagation directions and temperatures for LT. The group velocities are given in km/s.

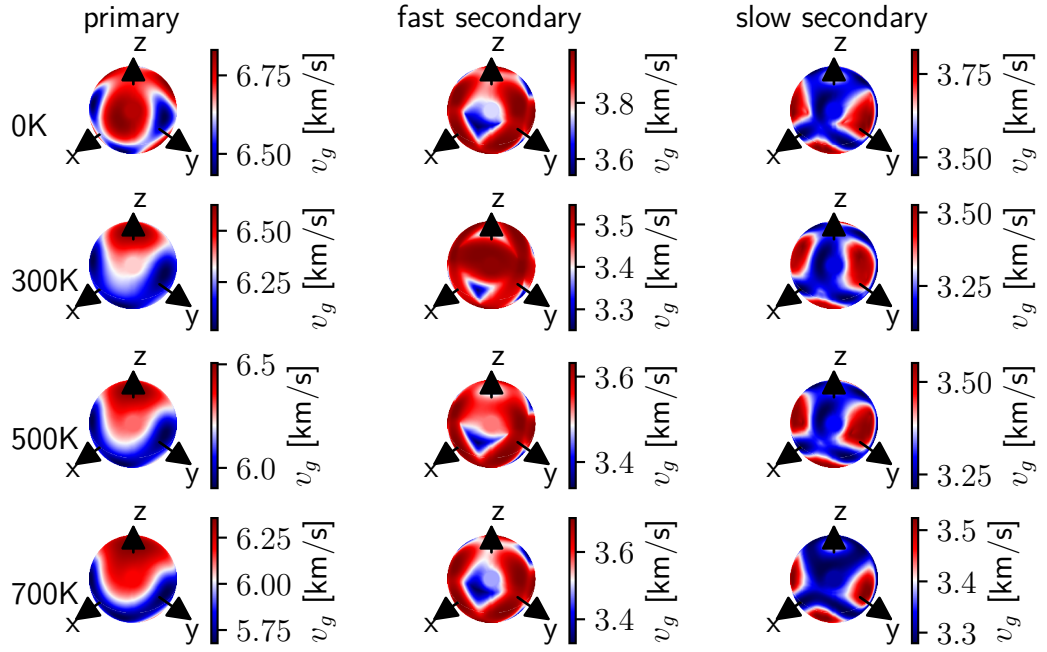

Figure 49: Group velocities of LN at different temperatures projected onto a sphere. The primary (longitudinal, left), and the secondary (transversal, fast and slow) velocities are shown. The corresponding temperature is denoted at the beginning of each line.

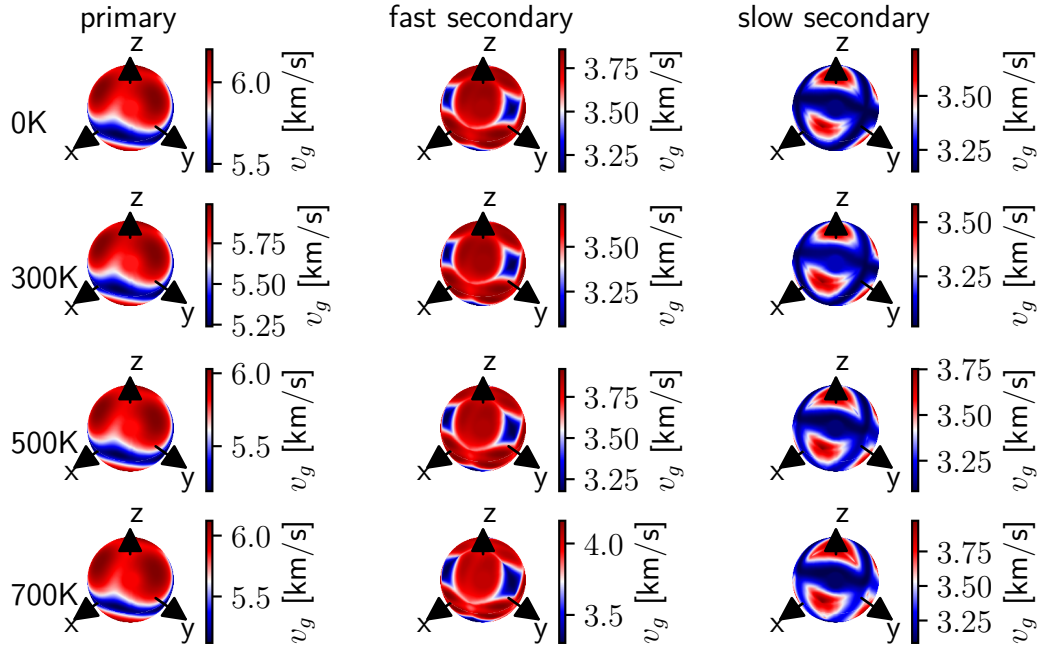

Figure 50: Group velocities of LT at different temperatures projected onto a sphere. The primary (longitudinal, left), and the secondary (transversal, fast and slow) velocities are shown. The corresponding temperature is denoted at the beginning of each line.

C Appendix C: LNT Solid Solutions

C.1 Strucutral Properties of LNT

Ta [%]	a_H [Å]	c [Å]	V [Å^3]	K [GPa]
0.0	5.139	13.826±0.001	105.425±0.005	111.843±2.241
4.2	5.14	13.824±0.001	105.419±0.005	113.099±1.684
6.25	5.141	13.822	105.452	110.783
8.3	5.14	13.821±0.001	105.422	115.615±0.156
12.5	5.141±0.001	13.819±0.002	105.43±0.023	113.148±3.42
16.7	5.141	13.816	105.409±0.005	115.312±1.427
20.8	5.141	13.813	105.408±0.006	116.106±1.792
25.0	5.142±0.001	13.811±0.002	105.423±0.017	114.725±1.499
29.2	5.142	13.809±0.001	105.404	116.869±0.207
31.25	5.143	13.809	105.44±0.006	114.453±0.012
33.3	5.142	13.807±0.001	105.406±0.001	117.664±0.501
37.5	5.143±0.001	13.806±0.003	105.419±0.026	117.233±1.885
41.7	5.143	13.802	105.402±0.002	120.626±1.603
43.75	5.145	13.804±0.001	105.445±0.003	116.348±0.016
45.8	5.143	13.801	105.409±0.002	120.185±0.36
50.0	5.145±0.002	13.8±0.002	105.424±0.028	119.776±2.525
54.2	5.144	13.797±0.001	105.414±0.002	121.886±0.245
56.25	5.146	13.799±0.001	105.453±0.002	118.205±0.019
58.3	5.145	13.795±0.001	105.412±0.004	123.468±1.066
62.5	5.146±0.001	13.795±0.003	105.436±0.026	121.355±2.276
66.7	5.146	13.792	105.428±0.003	123.36±0.472
68.75	5.147	13.793	105.465±0.006	120.074±0.024
70.8	5.146	13.79	105.43	124.311±0.181
75.0	5.147	13.789±0.001	105.456±0.018	123.057±2.1
79.2	5.147	13.788±0.001	105.444±0.001	125.817±0.056
81.25	5.148	13.788±0.001	105.486±0.005	121.98±0.013
83.3	5.148	13.785	105.449±0.001	126.614±0.158
87.5	5.148±0.001	13.785±0.002	105.477±0.02	125.786±3.797
91.7	5.149	13.782	105.467±0.001	129.65±0.195
93.75	5.149	13.783	105.509	123.924
95.8	5.149	13.782±0.001	105.483±0.001	130.143±0.985
100.0	5.149	13.782±0.001	105.494±0.001	128.816±5.857

Table 6: Hexagonal lattice constants a_H and c, rhombohedral unit cell volume V, and bulk modulus K of the LNT solid solutions, averaged over all SQS.

C.2 Phonon Frequencies of LNT

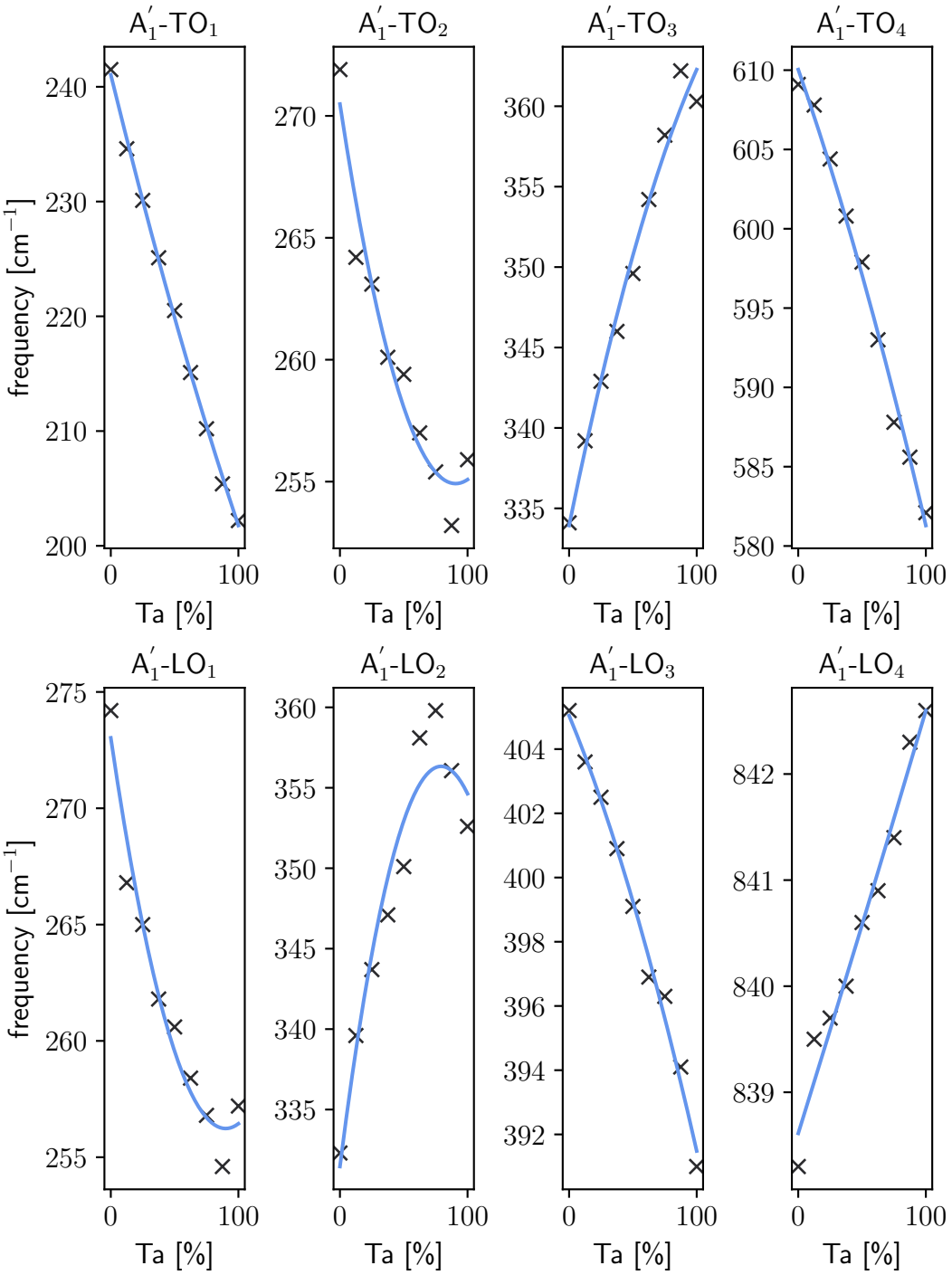

Figure 51: A_1-TO- (top) and A_1-LO-like (bottom) frequencies of the $LiNb_{1-x}Ta_xO_3$ solid solutions as a function of the composition.

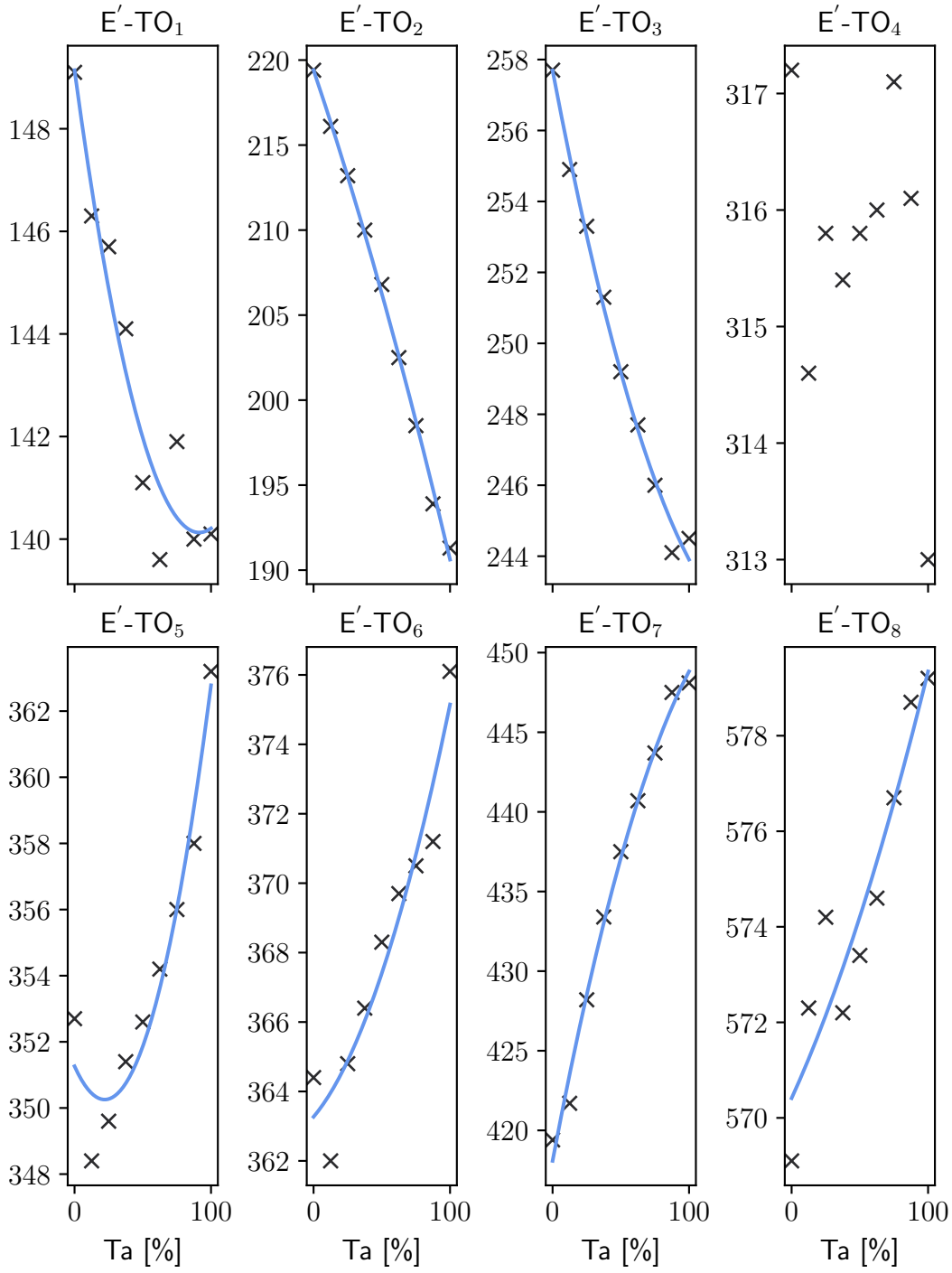

Figure 52: E-TO-like frequencies of the $LiNb_{1-x}Ta_xO_3$ solid solutions as a function of the composition.

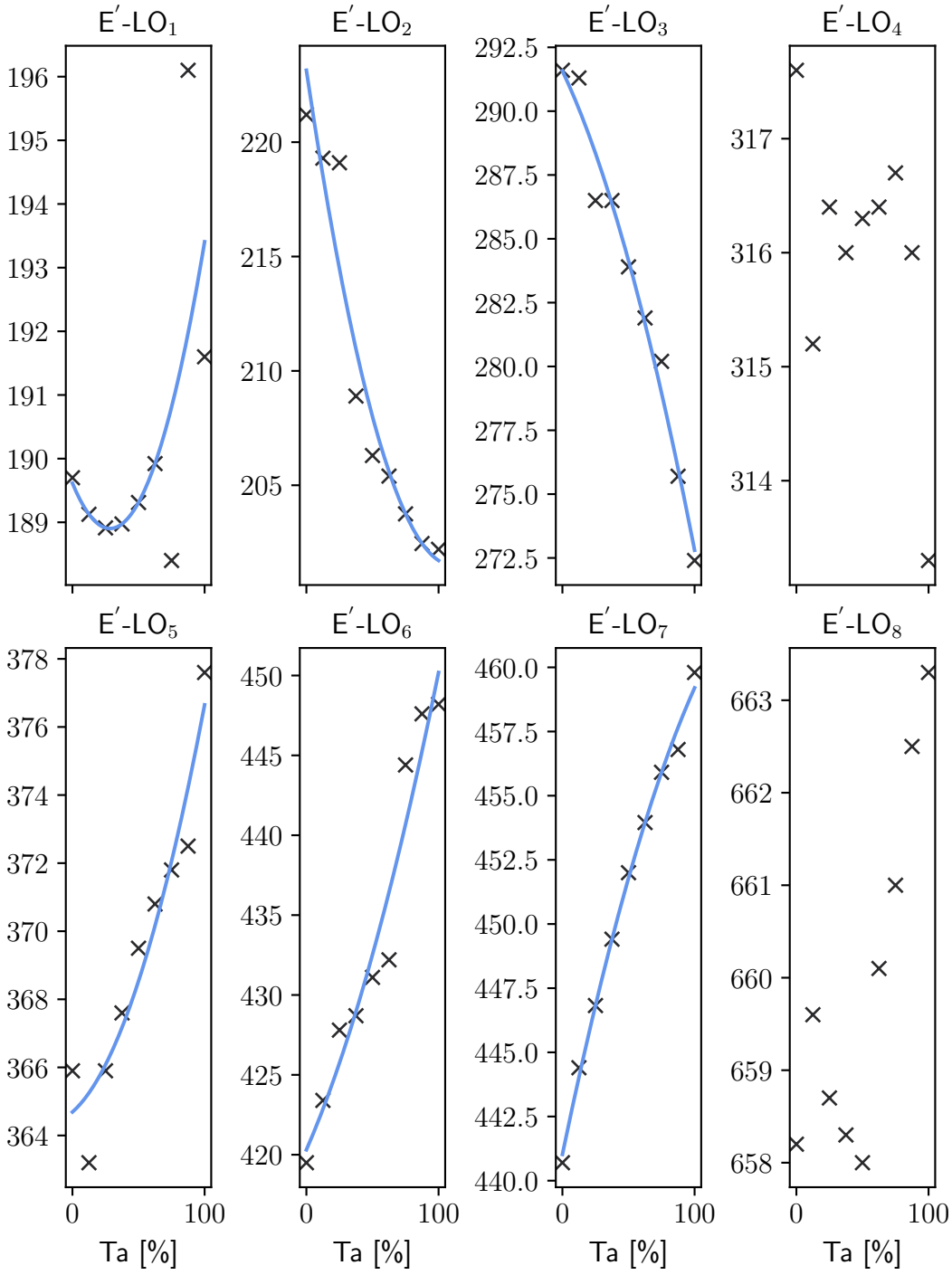

Figure 53: E-LO-like frequencies of the $LiNb_{1-x}Ta_xO_3$ solid solutions as a function of the composition.

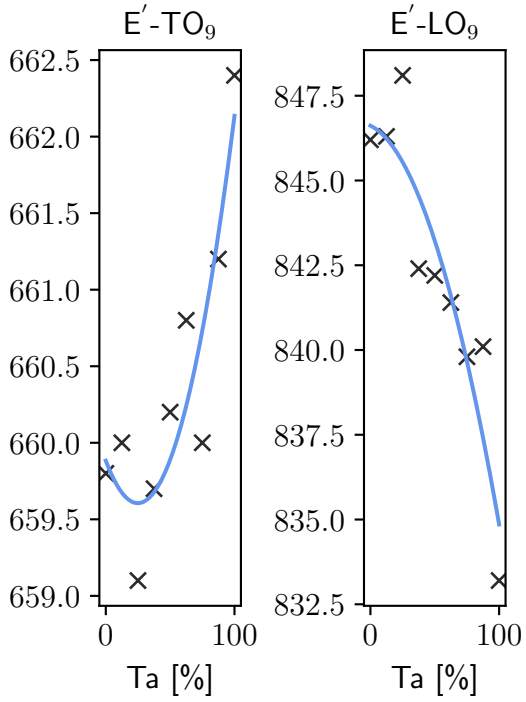

Figure 54: E-TO_9- and E-LO_9-like frequencies of the $LiNb_{1-x}Ta_xO_3$ solid solutions as a function of the composition.

Ta [%]	A_1'-TO [cm^{-1}]				A_1'-LO [cm^{-1}]			
0.0	242	272	334	609	274	332	405	838
12.5	235	264	339	608	267	340	404	840
25.0	230	263	343	604	265	344	403	840
37.5	225	260	346	601	262	347	401	840
50.0	221	259	350	598	261	350	399	841
62.5	215	257	354	593	258	358	397	841
75.0	210	255	358	588	257	360	396	841
87.5	206	253	362	586	255	356*	394	842
100.0	202	256	360	582	257	353	391	843*

Table 7: A_1-TO- and A_1-LO-like frequencies of the $LiNb_{1-x}Ta_xO_3$ solid solutions as a function of the composition. Values determined by fitting are denoted with an asterisk.

Ta [%]	E′-TO [cm^{-1}]								
0.0	149	219	258	317	353	364	419	569	660
12.5	146	216	255	315	348	362	422	572	660
25.0	146	213	253	316	350	365	428	574	659
37.5	144	210	251	315	351	366	433	572	660
50.0	141	207	249	316	353	368	438	573	660
62.5	140	203	248	316	354	370	441	575	661
75.0	142	199	246	317	356	371	444	577	660
87.5	140	194	244	316	358	371	448	579	661
100.0	140	191	245	313	363	376	448	579	662

Table 8: E-TO-like frequencies of the $LiNb_{1-x}Ta_xO_3$ solid solutions as a function of the composition.

Ta [%]	E′-LO [cm^{-1}]								
0.0	190	221	292	318	366	420	441	658	846
12.5	189*	219	291	315	363	423	444	660	846
25.0	189*	219	291	316	366	428	447*	659	848
37.5	189*	209	287	316	368	429	449*	658	842
50.0	189*	206	287	316	370	431	452	658	842
62.5	190*	205	284	316	371	432	454*	660	841
75.0	188	204*	282	317	372	444	456*	661	840
87.5	196	202*	276	316	373	448	457	663	840
100.0	192	202	272	313	378	448	460	663	833

Table 9: E-LO-like frequencies of the $LiNb_{1-x}Ta_xO_3$ solid solutions as a function of the composition. Values determined by fitting are denoted with an asterisk.

References

[1] L. Kovács, G. Ruschhaupt, K. Polgár, G. Corradi, and M. Wöhlecke. Composition dependence of the ultraviolet absorption edge in lithium niobate. *Applied Physics Letters*, 70(21):2801–2803, 05 1997. https://doi.org/10.1063/1.119056.

[2] J. Valasek. *Piezo-Electric and Allied Phenomena in Rochelle Salt*. PhD thesis, University of Minnesota, 1920. https://hdl.handle.net/11299/179514.

[3] D. A. Buck. Ferroelectrics for Digital Information Storage and Switching. Technical Report, 1952. http://hdl.handle.net/1721.3/40244.

[4] Izhar, M. M. A. Fiagbenu, S. Yao, X. Du, P. Musavigharavi, Y. Deng, J. Leathersich, C. Moe, A. Kochhar, E. A. Stach, R. Vetury, and R. H. Olsson. Periodically poled aluminum scandium nitride bulk acoustic wave resonators and filters for communications in the 6G era. *Microsystems & Nanoengineering*, 11(1):19, 2025. https://doi.org/10.1038/s41378-024-00857-4.

[5] F. Li, B. Wang, X. Gao, D. Damjanovic, L.-Q. Chen, and S. Zhang. Ferroelectric materials toward next-generation electromechanical technologies. *Science*, 389(6755):eadn4926, 2025. https://doi.org/10.1126/science.adn4926.

[6] A. Singh, S. Monga, N. Sharma, K. Sreenivas, and R. S. Katiyar. Ferroelectric, Piezoelectric Mechanism and Applications. *Journal of Asian Ceramic Societies*, 10(2):275–291, 2022. https://doi.org/10.1080/21870764.2022.2075618.

[7] R. S. Weis and T. K. Gaylord. Lithium niobate: Summary of physical properties and crystal structure. *Applied Physics A*, 37(4):191–203, 1985. https://doi.org/10.1007/BF00614817.

[8] H. Xu, S. Fu, R. Su, P. Liu, S. Zhang, Z. Lu, B. Xiao, R. Wang, C. Song, F. Zeng, W. Wang, and F. Pan. Saw filters on linbo3/sic heterostructure for 5g n77 and n78 band applications. *IEEE Transactions on Ultrasonics, Ferroelectrics, and Frequency Control*, 70(9):1157–1169, Sep. 2023. https:doi.org/10.1109/TUFFC.2023.3299635.

[9] K. Yang, J. Chen, J. Wang, F. Lin, J. Fang, M. Li, J. Zheng, Z. Ren, F. Qian, H. Sun, Y. Yang, and C. Zuo. SV-SAW RF filters based on low-cost 128°Y LiNbO3/SiO2/poly-Si/Si substrate for 6G cmWave wireless communications. *Microsystems & Nanoengineering*, 11(1):79, 2025. https://doi.org/10.1038/s41378-025-00949-9.

[10] Z. Lin, B. J. Shastri, S. Yu, J. Song, Y. Zhu, A. Safarnejadian, W. Cai, Y. Lin, W. Ke, M. Hammood, T. Wang, M. Xu, Z. Zheng, M. Al-Qadasi, O. Esmaeeli, M. Rahim, G. Pakulski, J. Schmid, P. Barrios, W. Jiang, H. Morison, M. Mitchell, X. Guan, N. A. F. Jaeger, L. A. Rusch, S. Shekhar, W. Shi, S. Yu, X. Cai, and L. Chrostowski. 120 GOPS Photonic tensor core in thin-film lithium niobate for inference and in situ training. *Nature Communications*, 15(1):9081, 2024. https://doi.org/10.1038/s41467-024-53261-x.

[11] M. Manzo, F. Laurell, V. Pasiskevicius, and K. Gallo. Lithium Niobate: The Silicon of Photonics! In Baldassare Di Bartolo and John Collins, editors, *Nano-Optics for Enhancing Light-Matter Interactions on a Molecular Scale*, pages 421–422, Dordrecht, 2013. Springer Netherlands. https://doi.org/10.1007/978-94-007-5313-6_42.

[12] M. Zhang, C. Wang, P. Kharel, D. Zhu, and M. Lonc ar. Integrated lithium niobate electro-optic modulators: when performance meets scalability. *Optica*, 8(5):652–667, may 2021. https://doi.org/10.1364/OPTICA.415762.

[13] A. Boes, L. Chang, C. Langrock, M. Yu, M. Zhang, Q. Lin, M. Lonc ar, M. Fejer, J. Bowers, and A. Mitchell. Lithium niobate photonics: Unlocking the electromagnetic spectrum. *Science*, 379(6627):eabj4396, 2023. https://doi.org/10.1126/science.abj4396.

[14] Y. S. Kim and R. T. Smith. Thermal expansion of lithium tantalate and lithium niobate single crystals. *Journal of Applied Physics*, 40(11):4637–4641, 1969. https://doi.org/10.1063/1.1657244.

[15] Y. Xu. *Ferroelectric Materials and Their Applications*. North Holland, 2013. https://doi.org/10.1016/C2009-0-12800-3.

[16] S. Zhang and F. Yu. Piezoelectric Materials for High Temperature Sensors. *Journal of the American Ceramic Society*, 94(10):3153–3170, 2011. https://doi.org/10.1111/j.1551-2916.2011.04792.x.

[17] K. Kitamura, Y. Furukawa, K. Niwa, V. Gopalan, and T. E. Mitchell. Crystal growth and low coercive field 180° domain switching characteristics of stoichiometric litao3. *Applied Physics Letters*, 73(21):3073–3075, 11 1998. https://doi.org/10.1063/1.122676.

[18] K. Sugii, H. Koizumi, S. Miyazawa, and S. Kondo. Temperature variations of lattice parameters of LiNbO3, LiTaO3 and Li (Nb 1-y Tay) O3 solid-solutions. *Journal of Crystal Growth*, 33(1):199–202, 1976. https://doi.org/10.1016/0022-0248(76)90105-6.

[19] A. Bartasyte, A. M. Glazer, F. Wondre, D. Prabhakaran, P. A. Thomas, S. Huband, D. S. Keeble, and S. Margueron. Growth of lithium niobate tantalate solid solution ion crystals. *Materials Chemistry and Physics*, 134(2):728–735, 2012. https://doi.org/10.1016/j.matchemphys.2012.03.060.

[20] W. Kohn and L. J. Sham. Self-consistent equations including exchange and correlation effects. *Phys. Rev.*, 140:A1133–A1138, Nov 1965. https://doi.org/10.1103/PhysRev.140.A1133.

[21] W. Kohn. Nobel lecture: Electronic structure of matter—wave functions and density functionals. *Rev. Mod. Phys.*, 71:1253–1266, Oct 1999. https://doi.org/10.1103/RevModPhys.71.1253.

[22] F. A. Pfeiffer. Generation and performance of special quasirandom structures for studying the structural properties of random alloys: Application to linbxta1–xo3. Bachelor's thesis, Justus-Liebig-Universität Giessen, 2020.

[23] J. Waack, N. Schäfer, M. Czerner, and C. Heiliger. Structural, elastic, and electronic properties of cubic zinc-blende in x ga 1 - x n alloys. *Physical Review B*, 110, 11 2024. https://doi.org/10.1103/PhysRevB.110.195201.

[24] J. Waack, M. Kremer, M. Czerner, and C. Heiliger. Structural and electronic properties of cubic rocksalt al x sc 1 - x n random alloys from ab initio calculations. *Physical Review B*, 109, 02 2024. https://doi.org/10.1103/PhysRevB.109.075142.

[25] W. Capelle. *Die Vorsokratiker, Fragmente und Quellenberichte*. Leipzig: Kröner, 1935. https://doi.org/10.1515/9783112763919.

[26] E. Rutherford. The scattering of α and β particles by matter and the structure of the atom. *The London, Edinburgh, and Dublin Philosophical Magazine and Journal of Science*, 21(125):669–688, 1911. https://doi.org/10.1080/14786440508637080.

[27] N. Bohr. I. on the constitution of atoms and molecules. *The London, Edinburgh, and Dublin Philosophical Magazine and Journal of Science*, 26(151):1–25, 1913. https://doi.org/10.1080/14786441308634955.

[28] J. P. Perdew, K. Burke, and M. Ernzerhof. Generalized gradient approximation made simple. *Physical Review Letters*, 77(18):3865–3868, 1996. https://doi.org/10.1103/PhysRevLett.77.3865.

[29] J. P. Perdew, A. Ruzsinszky, G. I. Csonka, O. A. Vydrov, G. E. Scuseria, L. A. Constantin, X. Zhou, and K. Burke. Restoring the density-gradient expansion for exchange in solids and surfaces. *Physical Review Letters*, 100(13):1–4, 2008. https://doi.org/10.1103/PhysRevLett.100.136406.

[30] S. L. Dudarev, G. A. Botton, S. Y. Savrasov, C. J. Humphreys, and A. P. Sutton. Electron-energy-loss spectra and the structural stability of nickel oxide: An lsda+u study. *Phys. Rev. B*, 57:1505–1509, Jan 1998. https://doi.org/10.1103/PhysRevB.57.1505.

[31] M. Cococcioni and S. de Gironcoli. Linear response approach to the calculation of the effective interaction parameters in the LDA + U method. *Phys. Rev. B*, 71:035105, Jan 2005. https://doi.org/10.1103/PhysRevB.71.035105.

[32] R. Jinnouchi, J. Lahnsteiner, F. Karsai, G. Kresse, and M. Bokdam. Phase transitions of hybrid perovskites simulated by machine-learning force fields trained on the fly with bayesian inference. *Phys. Rev. Lett.*, 122:225701, Jun 2019. http://doi.org/10.1103/PhysRevLett.122.225701.

[33] R. Jinnouchi, F. Karsai, and G. Kresse. On-the-fly machine learning force field generation: Application to melting points. *Phys. Rev. B*, 100:014105, Jul 2019. https://doi.org/10.1103/PhysRevB.100.014105.

[34] R. Jinnouchi, F. Karsai, C. Verdi, R. Asahi, and G. Kresse. Descriptors representing two- and three-body atomic distributions and their effects on the accuracy of machine-learned inter-atomic potentials. *The Journal of Chemical Physics*, 152(23):234102, 06 2020. https://doi.org/10.1063/5.0009491.

[35] R. D. King-Smith and D. Vanderbilt. Theory of polarization of crystalline solids. *Phys. Rev. B*, 47:1651–1654, Jan 1993. https://doi.org/10.1103/PhysRevB.47.1651.

[36] R. W. Nunes and X. Gonze. Berry-phase treatment of the homogeneous electric field perturbation in insulators. *Phys. Rev. B*, 63:155107, Mar 2001. https://doi.org/10.1103/PhysRevB.63.155107.

[37] X. Gonze, J.-C. Charlier, D.C. Allan, and M.P. Teter. Interatomic force constants from first principles: The case of α-quartz. *Physical Review B*, 50:13035–13038, Nov 1994. https://doi.org/10.1103/PhysRevB.50.13035.

[38] X. Gonze and C. Lee. Dynamical matrices, Born effective charges, dielectric permittivity tensors, and interatomic force constants from density-functional perturbation theory. *Physical Review B - Condensed Matter and Materials Physics*, 55(16):10355–10368, 1997. https://doi.org/10.1103/PhysRevB.55.10355.

[39] R. Bianco, I. Errea, L. Paulatto, M. Calandra, and F. Mauri. Second-order structural phase transitions, free energy curvature, and temperature-dependent anharmonic phonons in the self-consistent harmonic approximation: Theory and stochastic implementation. *Physical Review B*, 96(1):1–29, 2017. https://doi.org/10.1103/PhysRevB.96.014111.

[40] Z. Wu and R. E. Cohen. Pressure-induced anomalous phase transitions and colossal enhancement of piezoelectricity in pbtio$_3$. *Phys. Rev. Lett.*, 95:037601, Jul 2005. https://doi.org/10.1103/PhysRevLett.95.037601.

[41] R. Gross and A. Marx. *Festkörperphysik*. De Gruyter Oldenbourg, München, 2014. https://doi.org/10.1524/9783110358704.

[42] M. Gajdoš, K. Hummer, G. Kresse, J. Furthmüller, and F. Bechstedt. Linear optical properties in the projector-augmented wave methodology. *Physical Review B - Condensed Matter and Materials Physics*, 73(4):1–9, 2006. https://doi.org/10.1103/PhysRevB.73.045112.

[43] W. D. Johnston. Nonlinear optical coefficients and the raman scattering efficiency of lo and to phonons in acentric insulating crystals. *Phys. Rev. B*, 1:3494–3503, Apr 1970. https://doi.org/10.1103/PhysRevB.1.3494.

[44] E. Ising. Beitrag zur Theorie des Ferromagnetismus. *Zeitschrift für Physik*, 31(1):253–258, 1925. https://doi.org/10.1007/BF02980577.

[45] G. P. Francis and M. C. Payne. Finite basis set corrections to total energy pseudopotential calculations. *Journal of Physics: Condensed Matter*, 2(19):4395, 1990. https://dx.doi.org/10.1088/0953-8984/2/19/007.

[46] A. Togo, L. Chaput, I. Tanaka, and G. Hug. First-principles phonon calculations of thermal expansion in Ti3SiC2, Ti3AlC2, and Ti3GeC2. *Physical Review B*, 81(174301):1–6, 2010. https://doi.org/10.1103/PhysRevB.81.174301.

[47] A. Togo. First-principles Phonon Calculations with Phonopy and Phono3py. *Journal of the Physical Society of Japan*, 92(1), 2023. https://doi.org/10.7566/JPSJ.92.012001.

[48] A. Togo and I. Tanaka. First principles phonon calculations in materials science. *Scripta Materialia*, 108:1–5, 2015. https://doi.org/10.1016/j.scriptamat.2015.07.021.

[49] K. Parlinski, Z. Q. Li, and Y. Kawazoe. First-principles determination of the soft mode in cubic ZrO2. *Physical Review Letters*, 78(21):4063–4066, 1997. https://doi.org/10.1103/PhysRevLett.78.4063.

[50] M. Friedrich, A. Schindlmayr, W. G. Schmidt, and S. Sanna. $LiTaO_3$ phonon dispersion and ferroelectric transition calculated from first principles. *Physica Status Solidi (B) Basic Research*, 253(4):683–689, 2016. https://doi.org/10.1002/pssb.201552576.

[51] M. Friedrich, A. Riefer, S. Sanna, W. G. Schmidt, and A. Schindlmayr. Phonon dispersion and zero-point renormalization of $LiNbO_3$ from density-functional perturbation theory. *Journal of Physics: Condensed Matter*, 27(38):385402, sep 2015. https://dx.doi.org/10.1088/0953-8984/27/38/385402.

[52] A. M. Glass. Dielectric, thermal, and pyroelectric properties of ferroelectric litao$_3$. *Phys. Rev.*, 172:564–571, Aug 1968. https://doi.org/10.1103/PhysRev.172.564.

[53] S. Yao, J. Wang, H. Liu, X. Hu, H. Zhang, X. Cheng, and Z. Ling. Growth, optical and thermal properties of near-stoichiometric $LiNbO_3$ single crystal. *Journal of Alloys and Compounds*, 455(1):501–505, 2008. https://doi.org/10.1016/j.jallcom.2007.02.001.

[54] S. Wang, C. Ji, P. Dai, L. Shen, and N. Bao. The growth and characterization of six inch lithium niobate crystals with high homogeneity. *CrystEngComm*, 22(4):794–801, 2020. http://dx.doi.org/10.1039/C9CE01761E.

[55] N. Miyazaki, A. Hattori, and H. Uchida. Thermal shock cracking of lithium niobate single crystal. *Journal of Materials Science: Materials in Electronics*, 8(3):133–138, 1997. https://doi.org/10.1023/A:1018581710568.

[56] A. Oleaga, V. Shvalya, A. S. Sefat, and A. Salazar. Transport thermal properties of litao$_3$ pyroelectric sensor from 15 k to 400 k and its application to the study of critical behavior in euco$_2$as$_2$. *International Journal of Thermophysics*, 37(1):4, 2016. https://doi.org/10.1007/s10765-015-2013-1.

[57] Y.-L. Chen, J.-J. Xu, X.-J. Chen, Y.-F. Kong, and G.-Y. Zhang. Domain reversion process in near-stoichiometric LiNbO3 crystals. *Optics Communications*, 188(5):359–364, 2001. https://doi.org/10.1016/S0030-4018(00)01137-8.

[58] M. Nakamura, S. Takekawa, S. Kumaragurubaran, and K. Kitamura. Curie temperature and [Li]/([Li] + [Nb]) ratio of near-stoichiometric $LiNbO_3$ crystal grown from different Li-rich solutions. *Japanese Journal of Applied Physics*, 47(5R):3476, may 2008. https://dx.doi.org/10.1143/JJAP.47.3476.

[59] L. Monacelli, R. Bianco, M. Cherubini, M. Calandra, I. Errea, and F. Mauri. The stochastic self-consistent harmonic approximation: Calculating vibrational properties of materials with full quantum and anharmonic effects. *Journal of Physics Condensed Matter*, 33(36), 2021. https://doi.org/10.1088/1361-648X/ac066b.

[60] I. Errea, M. Calandra, and F. Mauri. First-principles theory of anharmonicity and the inverse isotope effect in superconducting palladium-hydride compounds. *Physical Review Letters*, 111(17):1–5, 2013. https://doi.org/10.1103/PhysRevLett.111.177002.

[61] I. Errea, M. Calandra, and F. Mauri. Anharmonic free energies and phonon dispersions from the stochastic self-consistent harmonic approximation: Application to platinum and palladium hydrides. *Physical Review B - Condensed Matter and Materials Physics*, 89(6):1–16, 2014. https://doi.org/10.1103/PhysRevB.89.064302.

[62] L. Monacelli, I. Errea, M. Calandra, and F. Mauri. Pressure and stress tensor of complex anharmonic crystals within the stochastic self-consistent harmonic approximation. *Physical Review B*, 98(2):24106, 2018. https://doi.org/10.1103/PhysRevB.98.024106.

[63] H. Lin, G. Tan, J.-N. Shen, S. Hao, L.-M. Wu, N. Calta, C. Malliakas, S. Wang, C. Uher, C. Wolverton, and M. G. Kanatzidis. Concerted Rattling in CsAg5Te3 Leading to Ultralow Thermal Conductivity and High Thermoelectric Performance. *Angewandte Chemie International Edition*, 55(38):11431–11436, 2016. https://doi.org/10.1002/anie.201605015.

[64] Y. Fu, H. Wei, L. Wei, H. Zhang, X. Wang, B. Liu, Y. Zhang, X. Lv, J. Zhou, and H. Yu. Origin of the difference in thermal conductivity and anharmonic phonon scattering between linbo3 and litao3. *CrystEngComm*, 23:8572–8578, 2021. https://dx.doi.org/10.1039/D1CE01323H.

[65] U. Bashir, M. Rüsing, D. Klimm, R. Blukis, B. Koppitz, L. M. Eng, M. Bickermann, and S. Ganschow. Thermal conductivity in solid solutions of lithium niobate tantalate single crystals from 300k up to 1300k. *Journal of Alloys and Compounds*, 1008:176549, 2024. https://doi.org/10.1016/j.jallcom.2024.176549.

[66] A. M. Hofmeister. Thermal diffusivity of garnets at high temperature. *Physics and Chemistry of Minerals*, 33(1):45–62, 2006. https://doi.org/10.1007/s00269-005-0056-8.

[67] E. Singh, M. N. Pionteck, S. Reitzig, M. Lange, M. Rüsing, L. M. Eng, and S. Sanna. Vibrational properties of $linbo_3$ and $litao_3$ under uniaxial stress. *Phys. Rev. Mater.*, 7:024420, Feb 2023. https://doi.org/10.1103/PhysRevMaterials.7.024420.

[68] M. T. Dove, Z. Wei, A. E. Phillips, D. A. Keen, and K. Refson. Which phonons contribute most to negative thermal expansion in scf3? *APL Materials*, 11(4):041130, 04 2023. https://doi.org/10.1063/5.0147610.

[69] D. Cuffari and A. Bongiorno. Calculation of mode grüneisen parameters made simple. *Phys. Rev. Lett.*, 124:215501, May 2020. https://doi.org/10.1103/PhysRevLett.124.215501.

[70] W. L. Bond. The mathematics of the physical properties of crystals. *The Bell System Technical Journal*, 22(1):1–72, 1943. https://doi.org/10.1002/j.1538-7305.1943.tb01304.x.

[71] S. Bouchy, R. J. Zednik, and P. Bélanger. Characterization of the Elastic, Piezoelectric, and Dielectric Properties of Lithium Niobate from 25 °C to 900 °C Using Electrochemical Impedance Spectroscopy Resonance Method. *Materials*, 15(13), 2022. https://doi.org/10.3390/ma15134716.

[72] F. Chen, L. Kong, W. Song, C. Jiang, S. Tian, F. Yu, L. Qin, C. Wang, and X. Zhao. The electromechanical features of LiNbO3 crystal for potential high temperature piezoelectric applications. *Journal of Materiomics*, 5(1):73–80, 2019. https://doi.org/10.1016/j.jmat.2018.10.001.

[73] M. Murota and Y. Shimizu. Elastic Constants and Temperature Coefficients of LiTaO3 for SAW Application. *Japanese Journal of Applied Physics*, 30(S1):156, jan 1991. https://dx.doi.org/10.7567/JJAPS.30S1.156.

[74] T. Yamada, H. Iwasaki, and N. Niizeki. Piezoelectric and Elastic Properties of LiTaO3: Temperature Characteristics. *Japanese Journal of Applied Physics*, 8(9):1127, sep 1969. https://dx.doi.org/10.1143/JJAP.8.1127.

[75] I. Takanaga and J.-I. Kushibiki. Elastic constants of multidomain litao3 crystal. *Journal of Applied Physics*, 86(6):3342–3346, 09 1999. https://doi.org/10.1063/1.371211.

[76] R. T. Smith and F. S. Welsh. Temperature dependence of the elastic, piezoelectric, and dielectric constants of lithium tantalate and lithium niobate. *Journal of Applied Physics*, 42(6):2219–2230, 1971. https://doi.org/10.1063/1.1660528.

[77] J. W. Jaeken and S. Cottenier. Solving the Christoffel equation: Phase and group velocities. *Computer Physics Communications*, 207:445–451, 2016. https://doi.org/10.1016/j.cpc.2016.06.014.

[78] A. S. Andrushchak, B. G. Mytsyk, H. P. Laba, O. V. Yurkevych, I. M. Solskii, A. V. Kityk, and B. Sahraoui. Complete sets of elastic constants and photoelastic coefficients of pure and mgo-doped lithium niobate crystals at room temperature. *Journal of Applied Physics*, 106(7):073510, 10 2009. https://doi.org/10.1063/1.3238507.

[79] C. Thierfelder, S. Sanna, A. Schindlmayr, and W. G. Schmidt. Do we know the band gap of lithium niobate? *physica status solidi c*, 7(2):362–365, 2010. https://doi.org/10.1002/pssc.200982473.

[80] A. Dhar and A. Mansingh. Optical properties of reduced lithium niobate single crystals. *Journal of Applied Physics*, 68(11):5804–5809, 12 1990. https://doi.org/10.1063/1.346951.

[81] M. Veithen and P. Ghosez. First-principles study of the dielectric and dynamical properties of lithium niobate. *Physical Review B*, 65:214302, May 2002. https://doi.org/10.1103/PhysRevB.65.214302.

[82] U. Schlarb and K. Betzler. Refractive indices of lithium niobate as a function of temperature, wavelength, and composition: A generalized fit. *Phys. Rev. B*, 48:15613–15620, Dec 1993. https://doi.org/10.1103/PhysRevB.48.15613.

[83] D. M. Smyth. The role of impurities in insultating transition metal oxides. *Progress in Solid State Chemistry*, 15(3):145–171, 1984. https://doi.org/10.1016/0079-6786(84)90001-3.

[84] S. C. Abrahams and P. Marsh. Defect structure dependence on composition in lithium niobate. *Acta Crystallographica Section B*, 42(1):61–68, feb 1986. https://doi.org/10.1107/S0108768186098567.

[85] H. Donnerberg, S. M. Tomlinson, C. R. A. Catlow, and O. F. Schirmer. Computer-simulation studies of intrinsic defects in linbo$_3$ crystals. *Phys. Rev. B*, 40:11909–11916, Dec 1989. https://doi.org/10.1103/PhysRevB.40.11909.

[86] N. Iyi, K. Kitamura, F. Izumi, J. K. Yamamoto, T. Hayashi, H. Asano, and S. Kimura. Comparative study of defect structures in lithium niobate with different compositions. *Journal of Solid State Chemistry*, 101(2):340–352, 1992. https://doi.org/10.1016/0022-4596(92)90189-3.

[87] H. Xu, D. Lee, J. He, S. B. Sinnott, V. Gopalan, V. Dierolf, and S. R. Phillpot. Stability of intrinsic defects and defect clusters in LiNbo$_3$ from density functional theory calculations. *Phys. Rev. B*, 78:174103, Nov 2008. https://doi.org/10.1103/PhysRevB.78.174103.

[88] Y. Li, W. G. Schmidt, and S. Sanna. Intrinsic LiNbo$_3$ point defects from hybrid density functional calculations. *Phys. Rev. B*, 89:094111, Mar 2014. https://doi.org/10.1103/PhysRevB.89.094111.

[89] Q. Li, B. Wang, C. H. Woo, H. Wang, and R. Wang. First-principles study on the formation energies of intrinsic defects in LiNbO3. *Journal of Physics and Chemistry of Solids*, 68(7):1336–1340, 2007. https://doi.org/10.1016/j.jpcs.2007.02.035.

[90] O. F. Schirmer, O. Thiemann, and M. Wöhlecke. Defects in linbo3—i. experimental aspects. *Journal of Physics and Chemistry of Solids*, 52(1):185–200, 1991. https://doi.org/10.1016/0022-3697(91)90064-7.

[91] F. Schmidt, A. L. Kozub, T. Biktagirov, C. Eigner, C. Silberhorn, A. Schindlmayr, W. G. Schmidt, and U. Gerstmann. Free and defect-bound (bi)polarons in linbo$_3$: Atomic structure and spectroscopic signatures from ab initio calculations. *Phys. Rev. Res.*, 2:043002, Oct 2020. https://doi.org/10.1103/PhysRevResearch.2.043002.

[92] E. Hüger, J. Rahn, J. Stahn, T. Geue, P. Heitjans, and H. Schmidt. Lithium diffusion in congruent linbo3 single crystals at low temperatures probed by neutron reflectometry. *Phys. Chem. Chem. Phys.*, 16:3670–3674, 2014. https://dx.doi.org/10.1039/C3CP54939A.

[93] S. Sanna, S. Neufeld, M. Rüsing, G. Berth, A. Zrenner, and W. G. Schmidt. Raman scattering efficiency in litao$_3$ and linbo$_3$ crystals. *Physical Review B*, 91:224302, Jun 2015. https://doi.org/10.1103/PhysRevB.91.224302.

[94] A. Sanson, A. Zaltron, N. Argiolas, C. Sada, M. Bazzan, W. G. Schmidt, and S. Sanna. Polaronic deformation at the fe$^{2+/3+}$ impurity site in fe:linbo$_3$ crystals. *Phys. Rev. B*, 91:094109, Mar 2015. https://doi.org/10.1103/PhysRevB.91.094109.

[95] V. Wang, N. Xu, J.-C. Liu, G. Tang, and W.-T. Geng. Vaspkit: A user-friendly interface facilitating high-throughput computing and analysis using vasp code. *Computer Physics Communications*, 267:108033, 2021. https://doi.org/10.1016/j.cpc.2021.108033.

[96] A. Krampf, M. Imlau, Y. Suhak, H. Fritze, and S. Sanna. Evaluation of similarities and differences of LiTaO3 and LiNbO3 based on high-T-conductivity, nonlinear optical fs-spectroscopy and ab initio modeling of polaronic structures. *New Journal of Physics*, 23(3):33016, mar 2021. https://dx.doi.org/10.1088/1367-2630/abe3ac.

[97] A. Riefer, S. Sanna, A. Schindlmayr, and W. G. Schmidt. Optical response of stoichiometric and congruent lithium niobate from first-principles calculations. *Phys. Rev. B*, 87:195208, May 2013. https://doi.org/10.1103/PhysRevB.87.195208.

[98] F. Shimura and Y. Fujino. Crystal growth and fundamental properties of LiNb1-yTayyO3. *Journal of Crystal Growth*, 38(3):293–302, 1977. https://doi.org/10.1016/0022-0248(77)90349-9.

[99] A. Manzoor, S. Pandey, D. Chakraborty, S. R. Phillpot, and D. S. Aidhy. Entropy contributions to phase stability in binary random solid solutions. *npj Computational Materials*, 4(1):47, 2018. https://doi.org/10.1038/s41524-018-0102-y.

[100] L. Bellaiche and D. Vanderbilt. Virtual crystal approximation revisited: Application to dielectric and piezoelectric properties of perovskites. *Phys. Rev. B*, 61:7877–7882, Mar 2000. https://doi.org/10.1103/PhysRevB.61.7877.

[101] P. Soven. Coherent-potential model of substitutional disordered alloys. *Phys. Rev.*, 156:809–813, Apr 1967. https://doi.org/10.1103/PhysRev.156.809.

[102] J. Korringa. Early history of multiple scattering theory for ordered systems. *Physics Reports*, 238(6):341–360, 1994. https://doi.org/10.1016/0370-1573(94)90122-8.

[103] H. Ebert, D. Ködderitzsch, and J. Minár. Calculating condensed matter properties using the KKR-Green's function method—recent developments and applications. *Reports on Progress in Physics*, 74(9):96501, aug 2011. https://dx.doi.org/10.1088/0034-4885/74/9/096501.

[104] J. M. Sanchez, F. Ducastelle, and D. Gratias. Generalized cluster description of multicomponent systems. *Physica A: Statistical Mechanics and its Applications*, 128(1):334–350, 1984. https://doi.org/10.1016/0378-4371(84)90096-7.

[105] D. B. Laks, L. G. Ferreira, S. Froyen, and A. Zunger. Efficient cluster expansion for substitutional systems. *Phys. Rev. B*, 46:12587–12605, Nov 1992. https://doi.org/10.1103/PhysRevB.46.12587.

[106] S.-H. Wei, L. G. Ferreira, J. E. Bernard, and A. Zunger. Electronic properties of random alloys: Special quasirandom structures. *Phys. Rev. B*, 42:9622–9649, Nov 1990. https://doi.org/10.1103/PhysRevB.42.9622.

[107] Y. Cai and C. Xie. Lattice mismatch, mechanical properties and lattice-compensation effect in Si1-xGex alloys by using first-principles calculations combined with virtual crystal approximation. *Physics Letters A*, 411:127528, 2021. https://doi.org/10.1016/j.physleta.2021.127528.

[108] X.-Z. Lu and J. M. Rondinelli. Epitaxial-strain-induced polar-to-nonpolar transitions in layered oxides. *Nature Materials*, 15(9):951–955, 2016. https://doi.org/10.1038/nmat4664.

[109] J. Falta, D. Bahr, A. Hille, G. Materlik, and H. J. Osten. Strain induced interface roughness of si1-xcx δ layers on si(001). *Applied Physics Letters*, 71(24):3525–3527, 12 1997. https://doi.org/10.1063/1.120380.

[110] A. Anam, S. Anand, and S. I. Amin. Design and performance analysis of tunnel field effect transistor with buried strained si1-xgex source structure based biosensor for sensitivity enhancement. *IEEE Sensors Journal*, 20(22):13178–13185, 2020. https://doi.org/10.1109/JSEN.2020.3004050.

[111] M. Mamor, K. Bouziane, and M. Maaza. On the alloying and strain effects of divacancy energy level in n-type si1-xgex. *Journal of Applied Physics*, 126(23):235707, 12 2019. https://doi.org/10.1063/1.5126111.

[112] M. Rüsing, S. Sanna, S. Neufeld, G. Berth, W. G. Schmidt, A. Zrenner, H. Yu, Y. Wang, and H. Zhang. Vibrational properties of lithium niobate tantalate mixed crystals. *Physical Review B*, 93:184305, May 2016. https://doi.org/10.1103/PhysRevB.93.184305.

[113] R. Gaillac, P. Pullumbi, and F.-X. Coudert. Elate: an open-source online application for analysis and visualization of elastic tensors. *Journal of Physics: Condensed Matter*, 28(27):275201, may 2016. https://dx.doi.org/10.1088/0953-8984/28/27/275201.

[114] A. Jain, S. P. Ong, G. Hautier, W. Chen, W. D. Richards, S. Dacek, S. Cholia, D. Gunter, D. Skinner, G. Ceder, and K. A. Persson. Commentary: The Materials Project: A materials genome approach to accelerating materials innovation. *APL Materials*, 1(1):011002, 2013. https://doi.org/10.1063/1.4812323.

[115] I. Pallikara, P. Kayastha, J. M. Skelton, and L. D. Whalley. The physical significance of imaginary phonon modes in crystals. *Electronic Structure*, 4(3):33002, july 2022. https://dx.doi.org/10.1088/2516-1075/ac78b3.

[116] A. Riefer, S. Sanna, and W. G. Schmidt. $LiNb_{1-x}Ta_xO_3$ Electronic Structure and Optical Response from First-Principles Calculations. *Ferroelectrics*, 447(1):78–85, 2013. https://doi.org/10.1080/00150193.2013.821904.

[117] J. Deslippe, G. Samsonidze, D. A. Strubbe, M. Jain, M. L. Cohen, and S. G. Louie. BerkeleyGW: A massively parallel computer package for the calculation of the quasiparticle and optical properties of materials and nanostructures. *Computer Physics Communications*, 183(6):1269–1289, 2012. https://doi.org/10.1016/j.cpc.2011.12.006.

[118] M. S. Hybertsen and S. G. Louie. Electron correlation in semiconductors and insulators: Band gaps and quasiparticle energies. *Phys. Rev. B*, 34:5390–5413, Oct 1986. https://doi.org/10.1103/PhysRevB.34.5390.

[119] P. Giannozzi, O. Andreussi, T. Brumme, O. Bunau, M. Buongiorno Nardelli, M. Calandra, R. Car, C. Cavazzoni, D. Ceresoli, M. Cococcioni, N. Colonna, I. Carnimeo, A. Dal Corso, S. de Gironcoli, P. Delugas, R. A. DiStasio Jr, A. Ferretti, A. Floris, G. Fratesi, G. Fugallo, R. Gebauer, U. Gerstmann, F. Giustino, T. Gorni, J. Jia, M. Kawamura, H.-Y. Ko, A. Kokalj, E. Küçükbenli, M. Lazzeri, M. Marsili, N. Marzari, F. Mauri, N. L. Nguyen, H.-V. Nguyen, A. Otero de-la Roza, L. Paulatto, S. Poncé, D. Rocca, R. Sabatini, B. Santra, M. Schlipf, A. P. Seitsonen, A. Smogunov, I. Timrov, T. Thonhauser, P. Umari, N. Vast, X. Wu, and S. Baroni. Advanced capabilities for materials modelling with quantum espresso. *Journal of Physics: Condensed Matter*, 29(46):465901, 2017. https://doi.org/10.1088/1361-648X/aa8f79.

[120] D. R. Hamann. Optimized norm-conserving vanderbilt pseudopotentials. *Phys. Rev. B*, 88:085117, Aug 2013. https://doi.org/10.1103/PhysRevB.88.085117.

[121] Z. H. Amber, B. Kirbus, L. M. Eng, and M. Rüsing. Quantifying the coherent interaction length of second-harmonic microscopy in lithium niobate confined nanostructures. *Journal of Applied Physics*, 130(13):133102, 10 2021. https://doi.org/10.1063/5.0058996.

[122] I. G. Wood, P. Daniels, R. H. Brown, and A. M. Glazer. Optical birefringence study of the ferroelectric phase transition in lithium niobate tantalate mixed crystals: $LiNb_{1-x}Ta_xO_3$. *Journal of Physics: Condensed Matter*, 20(23):235237, may 2008. https://dx.doi.org/10.1088/0953-8984/20/23/235237.

[123] S. Kondo, K. Sugii, S. Miyazawa, and S. Uehara. LPE growth of $Li(Nb,Ta)O_3$ solid-solution thin film waveguides on $LiTaO_3$ substrates. *Journal of Crystal Growth*, 46(3):314–322, 1979. https://doi.org/10.1016/0022-0248(79)90079-4.

[124] V. Caciuc and A. V. Postnikov. Ab initio zone-center phonons in $LiTaO_3$: Comparison to $LiNbO_3$. *Physical Review B*, 64:224303, Nov 2001. https://doi.org/10.1103/PhysRevB.64.224303.

[125] C. Raptis. Assignment and temperature dependence of the raman modes of $LiTaO_3$ studied over the ferroelectric and paraelectric phases. *Physical Review B*, 38:10007–10019, Nov 1988. https://doi.org/10.1103/PhysRevB.38.10007.

[126] S. Margueron, A. Bartasyte, A. M. Glazer, E. Simon, J. Hlinka, I. Gregora, and J. Gleize. Resolved E-symmetry zone-centre phonons in LiTaO3 and LiNbO3. *Journal of Applied Physics*, 111(10):104105, 05 2012. https://doi.org/10.1063/1.4716001.

[127] A. Ridah, P. Bourson, M. D. Fontana, and G. Malovichko. The composition dependence of the raman spectrum and new assignment of the phonons in $LiNbO_3$. *Journal of Physics: Condensed Matter*, 9(44):9687, nov 1997. https://dx.doi.org/10.1088/0953-8984/9/44/022.

[128] X. Yang, G. Lan, B. Li, and H. Wang. Raman Spectra and Directional Dispersion in LiNbO3 and LiTaO3. *physica status solidi (b)*, 142(1):287–300, 1987. https://doi.org/10.1002/pssb.2221420130.

[129] K. Parlinski, Z. Q. Li, and Y. Kawazoe. Ab initio calculations of phonons in $linbo_3$. *Phys. Rev. B*, 61:272–278, Jan 2000. https://doi.org/10.1103/PhysRevB.61.272.

[130] C. A. Gautier, M. Mérian, and J. Etchepare. Low frequency e-symmetry phonon modes in litao3: a non-linear temporal domain approach. *Journal of Physics: Condensed Matter*, 12(32):7175, aug 2000. https://dx.doi.org/10.1088/0953-8984/12/32/302.

[131] R. Claus, G. Borstel, E. Wiesendanger, and L. Steffan. Assignments of optical phonon modes in $linbo_3$. *Phys. Rev. B*, 6:4878–4879, Dec 1972. https://doi.org/10.1103/PhysRevB.6.4878.

[132] P. Hermet, M. Veithen, and P. Ghosez. First-principles calculations of the nonlinear optical susceptibilities and raman scattering spectra of lithium niobate. *Journal of Physics: Condensed Matter*, 19(45):456202, oct 2007. https://dx.doi.org/10.1088/0953-8984/19/45/456202.

[133] A. Bartasyte, S. Margueron, A. M. Glazer, E. Simon, I. Gregora, S. Huband, and P. A. Thomas. Vibrational modes and overlap matrix of $LiNb_{1-x}Ta_xo_3$ mixed crystals. *Physical Review B*, 99:094306, Mar 2019. https://doi.org/10.1103/PhysRevB.99.094306.

[134] V. S. Gorelik, N. V. Sidorov, and A. I. Vodchits. Optical properties of lithium niobate and lithium tantalate crystals with impurities and defects. *Physics of Wave Phenomena*, 25(1):10–19, 2017. https://doi.org/10.3103/S1541308X17010022.

[135] Y. Repelin, E. Husson, F. Bennani, and C. Proust. Raman spectroscopy of lithium niobate and lithium tantalate. force field calculations. *Journal of Physics and Chemistry of Solids*, 60(6):819–825, 1999. https://doi.org/10.1016/S0022-3697(98)00333-3.

[136] I. Souza, J. Íñiguez, and D. Vanderbilt. First-principles approach to insulators in finite electric fields. *Phys. Rev. Lett.*, 89:117602, Aug 2002. https://doi.org/10.1103/PhysRevLett.89.117602.

[137] A. S. Barker and R. Loudon. Dielectric properties and optical phonons in $LiNbO_3$. *Physical Review*, 158:433–445, Jun 1967. https://doi.org/10.1103/PhysRev.158.433.

[138] T. Fujii, A. Ando, and Y. Sakabe. Characterization of dielectric properties of oxide materials in frequency range from GHz to THz. *Journal of the European Ceramic Society*, 26(10):1857–1860, 2006. https://doi.org/10.1016/j.jeurceramsoc.2005.09.094.

[139] A. S. Barker, A. A. Ballman, and J. A. Ditzenberger. Infrared study of the lattice vibrations in $litao_3$. *Phys. Rev. B*, 2:4233–4239, Nov 1970. https://doi.org/10.1103/PhysRevB.2.4233.

[140] T. Weigel, C. Ludt, T. Leisegang, E. Mehner, S. Jachalke, H. Stöcker, T. Doert, D. C. Meyer, and M. Zschornak. Spontaneous polarization and pyroelectric coefficient of lithium niobate and lithium tantalate determined from crystal structure data. *Phys. Rev. B*, 108:054105, Aug 2023. https://doi.org/10.1103/PhysRevB.108.054105.

[141] V. Gopalan, T. E. Mitchell, Y. Furukawa, and K. Kitamura. The role of nonstoichiometry in 180° domain switching of linbo3 crystals. *Applied Physics Letters*, 72(16):1981–1983, 04 1998. https://doi.org/10.1063/1.121491.

[142] S. H. Wemple, M. Jr DiDomenico, and I. Camlibel. Relationship between linear and quadratic electro-optic coefficients in linbo3, litao3, and other oxygen-octahedra ferroelectrics based on direct measurement of spontaneous polarization. *Applied Physics Letters*, 12(6):209–211, 03 1968. https://doi.org/10.1063/1.1651955.

[143] A. Savage. Pyroelectricity and spontaneous polarization in linbo3. *Journal of Applied Physics*, 37(8):3071–3072, 07 1966. https://doi.org/10.1063/1.1703164.

[144] M. Kovár , L. Dvořák, and S. Černý. Application of pyroelectric properties of LiTaO3 single crystal to microcalorimetric measurement of the heat of adsorption. *Applied Surface Science*, 74(1):51–59, 1994. https://doi.org/10.1016/0169-4332(94)90099-X.

[145] M.-C. Kao, M.-S. Lee, C.-M. Wang, H.-Z. Chen, and Y.-C. Chen. Properties of LiTaO3 Thin Films Derived by a Diol-Based Sol-Gel Process. *Japanese Journal of Applied Physics*, 41(5R):2982, may 2002. https://dx.doi.org/10.1143/JJAP.41.2982.

[146] C. Kofahl, L. Dörrer, B. A. Muscutt, S. Sanna, S. Hurskyy, U. Yakhnevych, Y. Suhak, H. Fritze, S. Ganschow, and H. Schmidt. Li self-diffusion and ion conductivity in congruent $linbo_3$ and $litao_3$ single crystals. *Phys. Rev. Mater.*, 7:033403, Mar 2023. https://doi.org/10.1103/PhysRevMaterials.7.033403.

[147] C. Kofahl, J. Uhlendorf, B. A. Muscutt, M. N. Pionteck, S. Sanna, H. Fritze, S. Ganschow, and H. Schmidt. Oxygen diffusion in li(nb,ta)o3 single crystals. *physica status solidi (a)*, 222(1):2300959, 2025. https://doi.org/10.1002/pssa.202300959.

[148] L. M. Verhoff, M. N. Pionteck, M. Rüsing, H. Fritze, L. M. Eng, and S. Sanna. Two-dimensional electronic conductivity in insulating ferroelectrics: Peculiar properties of domain walls. *Phys. Rev. Res.*, 6:L042015, Oct 2024. https://doi.org/10.1103/PhysRevResearch.6.L042015.

[149] H. Wulfmeier, U. Yakhnevych, C. Boekhoff, A. Diima, M. Kunzner, L. M. Verhoff, J. Paul, J. Ratzenberger, E. Beyreuther, J. Gössel, I. Kiseleva, M. Rüsing, S. Sanna, L. M. Eng, and H. Fritze. Demonstration of domain wall current in mgo-doped lithium niobate single crystals up to 400°c. *Solid State Ionics*, 429:116949, 2025. https://doi.org/10.1016/j.ssi.2025.116949.

[150] A. Rogers, R. Lynch, K. Holsgrove, C. McCluskey, A. Kumar, R. McQuaid, and M. Gregg. Twisted charged interfaces in ferroelectrics, 2025. https://www.mrs.org/meetings-events/annual-meetings/archive/meeting/presentations/view/2025-mrs-spring-meeting/2025-mrs-spring-meeting-4201952.

[151] J. Zhao, C. Ma, M. Rüsing, and S. Mookherjea. High quality entangled photon pair generation in periodically poled thin-film lithium niobate waveguides. *Phys. Rev. Lett.*, 124:163603, Apr 2020. https://doi.org/10.1103/PhysRevLett.124.163603.

[152] T. Descamps, T. Schetelat, J. Gao, P. J. Poole, D. Dalacu, A. W. Elshaari, and V. Zwiller. Dynamic Strain Modulation of a Nanowire Quantum Dot Compatible with a Thin-Film Lithium Niobate Photonic Platform. *ACS Photonics*, 10(10):3691–3699, oct 2023. https://doi.org/10.1021/acsphotonics.3c00821.

[153] E. Singh, H. Beccard, Z. H. Amber, J. Ratzenberger, C. W. Hicks, M. Rüsing, and L. M. Eng. Tuning domain wall conductivity in bulk lithium niobate by uniaxial stress. *Phys. Rev. B*, 106:144103, Oct 2022. https://doi.org/10.1103/PhysRevB.106.144103.

[154] M. N. Pionteck, M. Roeper, B. Koppitz, S. D. Seddon, M. Rüsing, L. Padberg, C. Eigner, C. Silberhorn, S. Sanna, and L. M. Eng. Second-order nonlinear piezo-optic properties of single crystal lithium niobate thin films. *Phys. Rev. B*, 111:064109, Feb 2025. https://doi.org/10.1103/PhysRevB.111.064109.

[155] A. Di Francescantonio, A. Sabatti, He. Weigand, E. Bailly-Rioufreyt, M. Antonietta Vincenti, Luca C., J. Kellner, A. Zilli, M. Finazzi, M. Celebrano, and R. Grange. Efficient GHz electro-optical modulation with a nonlocal lithium niobate metasurface in the linear and nonlinear regime. *Nature Communications*, 16(1):7000, 2025. https://doi.org/10.1038/s41467-025-62072-7.

[156] É Tichy-Rács, S. Hurskyy, U. Yakhnevych, P. Gaczyński, S. Ganschow, H. Fritze, and Y. Suhak. Influence of li-stoichiometry on electrical and acoustic properties and temperature stability of li(nb,ta)o3 solid solutions up to 900°c. *physica status solidi (a)*, 222(1):2300962, 2025. https://doi.org/10.1002/pssa.202300962.

[157] D. Xue, K. Betzler, and H. Hesse. Dielectric properties of lithium niobate–tantalate crystals. *Solid State Communications*, 115(11):581–585, 2000. https://doi.org/10.1016/S0038-1098(00)00243-X.

[158] A. M. Glazer, N. Zhang, A. Bartasyte, D. S. Keeble, S. Huband, and P. A. Thomas. Observation of unusual temperature-dependent stripes in litao3 and lita x nb1-x o3 crystals with near-zero birefringence. *Journal of Applied Crystallography*, 43(6):1305–1313, DEC 2010. https://doi.org/10.1107/S0021889810033868.

[159] D. Roshchupkin, E. Emelin, O. Plotitcyna, F. Rashid, D. Irzhak, V. Karandashev, T. Orlova, N. Targonskaya, S. Sakharov, A. Mololkin, B. Redkin, H. Fritze, Y. Suhak, D. Kovalev, S. Vadilonga, L. Ortega, and W. Leitenberger. Single crystals of ferroelectric lithium niobate-tantalate linb1-xtaxo3 solid solutions for high-temperature sensor and actuator applications. *Acta Crystallographica Section B-Structural Science Crystal Engineering and Materials*, 76(6):1071–1076, DEC 2020. https://doi.org/10.1107/S2052520620014390.

[160] G. Kresse and J. Hafner. Ab initio molecular dynamics for liquid metals. *Physical Review B*, 47(1):558–561, 1993. https://doi.org/10.1103/PhysRevB.47.558.

[161] G. Kresse and J. Furthmüller. Efficient iterative schemes for ab initio total-energy calculations using a plane-wave basis set. *Physical Review B - Condensed Matter and Materials Physics*, 54(16):11169–11186, 1996. https://doi.org/10.1103/PhysRevB.54.11169.

[162] D. Joubert. From ultrasoft pseudopotentials to the projector augmented-wave method. *Physical Review B - Condensed Matter and Materials Physics*, 59(3):1758–1775, 1999. https://doi.org/10.1103/PhysRevB.59.1758.

[163] G. Kresse and J. Furthmüller. Efficiency of ab-initio total energy calculations for metals and semiconductors using a plane-wave basis set. *Computational Materials Science*, 6(1):15–50, 1996. https://doi.org/10.1016/0927-0256(96)00008-0.

[164] J. D. Pack and H. J. Monkhorst. "special points for Brillouin-zone integrations"-a reply. *Physical Review B*, 16(4):1748–1749, 1977. https://doi.org/10.1103/PhysRevB.16.1748.

[165] A. V. Shapeev. Moment tensor potentials: A class of systematically improvable interatomic potentials. *Multiscale Modeling & Simulation*, 14(3):1153–1173, 2016. https://doi.org/10.1137/15M1054183.

[166] A. Togo, L. Chaput, and I. Tanaka. Distributions of phonon lifetimes in brillouin zones. *Phys. Rev. B*, 91:094306, Mar 2015. https://doi.org/10.1103/PhysRevB.91.094306.

[167] Atsushi T., Laurent C., Terumasa T., and Isao T. Implementation strategies in phonopy and phono3py. *Journal of Physics: Condensed Matter*, 35(35):353001, jun 2023. https://dx.doi.org/10.1088/1361-648X/acd831.

[168] K. Holtgrewe. *Theoretical modelling of nano-scaled systems with heavy ions*. PhD thesis, Justus-Liebig-Universität Giessen, 2022. https://doi.org/10.22029/jlupub-7899.

[169] L. M. Verhoff. Theoretical modelling of domains and domain walls in ferroelectric oxides. Master's thesis, Justus-Liebig-Universität Giessen, 2023.

[170] H. de Castilla, P. Bélanger, and R. J. Zednik. High temperature characterization of piezoelectric lithium niobate using electrochemical impedance spectroscopy resonance method. *Journal of Applied Physics*, 122(24):244103, 12 2017. https://doi.org/10.1063/1.4996202.

[171] E. Butaud, S. Ballandras, M. Bousquet, A. Drouin, B. Tavel, I. Huyet, A. Clairet, I. Bertrand, A. Ghorbel, and A. Reinhardt. Innovative smart cut™ piezo on insulator (poi) substrates for 5g acoustic filters. In *2020 IEEE International Electron Devices Meeting (IEDM)*, pages 34.6.1–34.6.4, Dec 2020. https://doi.org/10.1109/IEDM13553.2020.9372020.

[172] R. P. Feynman. Forces in molecules. *Phys. Rev.*, 56:340–343, Aug 1939. https://doi.org/10.1103/PhysRev.56.340.

[173] V. G. Tyuterev and N. Vast. Murnaghan's equation of state for the electronic ground state energy. *Computational Materials Science*, 38(2):350–353, 2006. https://doi.org/10.1016/j.commatsci.2005.08.012.

[174] P. Y. Yu and M. Cardona. Fundamentals of semiconductors. physics and materials properties. 4. ed., Jul 2010. https://doi.org/10.1007/978-3-642-00710-1.

[175] D. C. Wallace. *Thermoelastic Theory of Stressed Crystals and Higher-Order Elastic Constants*, volume 25 of *Solid State Physics*. Academic Press, 1970. https://doi.org/10.1016/S0081-1947(08)60010-7.

[176] S. Sanna. Bound electron polarons in lithium niobate. In *2015 Symposium on Piezoelectricity, Acoustic Waves, and Device Applications (SPAWDA)*, pages 523–527, 2015. https://doi.org/10.1109/SPAWDA.2015.7364545.

[177] J. Hayden, M. D. Hossain, Y. Xiong, K. Ferri, W. Zhu, M. V. Imperatore, N. Giebink, S. Trolier-McKinstry, I. Dabo, and J.-P. Maria. Ferroelectricity in boron-substituted aluminum nitride thin films. *Phys. Rev. Mater.*, 5:044412, Apr 2021. https://doi.org/10.1103/PhysRevMaterials.5.044412.

[178] D. Wang, S. Mondal, J. Liu, M. Hu, P. Wang, S. Yang, D. Wang, Y. Xiao, Yu. Wu, T. Ma, and Z. Mi. Ferroelectric yaln grown by molecular beam epitaxy. *Applied Physics Letters*, 123(3):033504, 07 2023. https://doi.org/10.1063/5.0159562.

[179] G. Ghosh, A. van de Walle, and M. Asta. First-principles calculations of the structural and thermodynamic properties of bcc, fcc and hcp solid solutions in the al–tm (tm=ti, zr and hf) systems: A comparison of cluster expansion and supercell methods. *Acta Materialia*, 56(13):3202–3221, 2008. https://doi.org/10.1016/j.actamat.2008.03.006.

[180] J. von Pezold, A. Dick, M. Friák, and J. Neugebauer. Generation and performance of special quasirandom structures for studying the elastic properties of random alloys: Application to Al-Ti. *Phys. Rev. B*, 81:094203, Mar 2010. https://doi.org/10.1103/PhysRevB.81.094203.

[181] M. Montanari, C. Ciano, L. Persichetti, C. Corley, L. Baldassarre, M. Ortolani, L. Di Gaspare, G. Capellini, D. Stark, G. Scalari, M. Virgilio, and M. De Seta. Thz intersubband absorption in n-type si1-xgex parabolic quantum wells. *Applied Physics Letters*, 118(16):163106, 04 2021. https://doi.org/10.1063/5.0048344.

[182] R. H. Lyddane, R. G. Sachs, and E. Teller. On the polar vibrations of alkali halides. *Physical Review*, 59:673–676, Apr 1941. https://doi.org/10.1103/PhysRev.59.673.

[183] S. Sanna, A. Riefer, S. Neufeld, W. G. Schmidt, G. Berth, M. Rüsing, Widhalm A., and A. Zrenner. Vibrational fingerprints of $LiNbO_3$-$LiTaO_3$ mixed crystals. *Ferroelectrics*, 447(1):63–68, 2013. https://doi.org/10.1080/00150193.2013.821893.

[184] A. S. Chaves and S. P. S. Porto. Generalized lyddane-sachs-teller relation. *Solid State Communications*, 13(7):865–868, 1973. https://doi.org/10.1016/0038-1098(73)90386-4.

[185] S. Hurskyy, U. Yakhnevych, C. Kofahl, É. Tichy-Rács, H. Schmidt, S. Ganschow, H. Fritze, and Y. Suhak. Electrical properties and temperature stability of li-deficient and near stoichiometric li(nb,ta)o3 solid solutions up to 900 °c. *Solid State Ionics*, 399, OCT 15 2023. https://doi.org/10.1016/j.ssi.2023.116285.

Webpages

[W1] J. Dalton. *A new system of chemical philosophy*. London, 1808. https://archive.org/details/newsystemofchemi01daltuoft/mode/2up.

[W2] H. Freiser and G. H. Nancollas. *Compendium of Analytical Nomenclature, 2nd ed.* IUPAC Chemical Data. Wiley, 1991. https://books.google.de/books?id=kD1jQgAACAAJ.

[W3] Infineon bringt neue Ferroelectric-RAM-Chips auf den Markt. https://tinyurl.com/2yjcubm8, 2022. Accessed: 16.07.2025.

[W4] Electro-Optic Modulators. https://www.thorlabs.com/navigation.cfm?guide_id=2090, 2025. Accessed: 26.08.2025.

[W5] Vibrating Piezoelectric Actuator. https://www.thorlabs.com/newgrouppage9.cfm?objectgroup_id=14882, 2025. Accessed: 27.08.2025.

[W6] piezosystem jena: Solutions for a wide range of optical applications. https://www.piezosystem.com/applications/microscopy/, 2025. Accessed: 27.08.2025.

[W7] Lithium niobate electro-optic modulators. https://www.exail.com/product-range/linbo3-electro-optic-modulators, 2025. Accessed: 26.08.2025.

[W8] On-the-fly machine learning force fields with the Vienna Ab-initio Simulation Package (VASP). https://mats.net.technion.ac.il/files/2022/07/VASP_ML_intro.pdf. Accessed: 16.12.2024.

[W9] The NIST Reference on Constants, Units, and Uncertainty. https://physics.nist.gov/cuu/Constants/. Accessed: 28.07.2025.

[W10] Yambo wiki. https://www.yambo-code.eu/wiki/index.php/Main_Page. Accessed: 20.10.2023.

[W11] The VASP site. https://www.vasp.at/wiki/index.php/The_VASP_Manual. Accessed: 01.06.2025.

[W12] Folding Phonons. https://dannyvanpoucke.be/folding-phonons. Accessed: 13.07.2024.

[W13] Phonopy. https://phonopy.github.io/phonopy. Accessed: 22.07.2025.

[W14] Statistical Thermodynamics. https://chem.libretexts.org/Bookshelves/Physical_and_Theoretical_Chemistry_Textbook_Maps/Statistical_Thermodynamics_(Jeschke). Accessed: 24.10.2023.

[W15] Bilbao crystallographic server. https://www.cryst.ehu.es/cgi-bin/cryst/programs/nph-polarizationselrules. Accessed: 13.03.2024.

[W16] Online Dictionary of Crystallography. https://dictionary.iucr.org/. Accessed: 05.11.2024.

[W17] Korth Kristalle GmbH. https://www.korth.de/en/materials/detail/Lithium%20Tantalate, 2024. Accessed: 02.05.2024.

[W18] The University of Sheffield. WebElements. https://www.webelements.com, 2023. Accessed: 06.05.2025.

[W19] Website der FOR5044. https://www.for5044.de/, 2020. Accessed: 02.07.2025.

Own Publications

[P1] B. Koppitz, T. Saxena, F. Bernhardt, S. Ganschow, S. Sanna, M. Rüsing, and L. M. Eng. Second harmonic generation contrasts of ferroelectric domain structures and composition in lithium niobate-tantalate mixed crystals. *Journal of Applied Physics*, 138(3):034101, 07 2025. https://doi.org/10.1063/5.0276183.

[P2] F. Bernhardt and S. Sanna. Modeling wo3 beyond the harmonic approximation: Theoretical characterization and thermal expansion. *The Journal of Physical Chemistry C*, 129(1):580–590, 2025. https://doi.org/10.1021/acs.jpcc.4c05225.

[P3] F. Bernhardt, S. Gharat, A. Kapp, F. Pfeiffer, R. Buschbeck, F. Hempel, O. Pashkin, S. C. Kehr, M. Rüsing, S. Sanna, and L. M. Eng. Lattice dynamics of linb$_{1-x}$ta$_x$o$_3$ solid solutions: Theory and experiment. *physica status solidi (a)*, 222(1):2300968, 2025. https://doi.org/10.1002/pssa.202300968.

[P4] U. Yakhnevych, V. Sargsyan, F. El Azzouzi, A. Kapp, F. Bernhardt, Y. Suhak, S. Ganschow, H. Schmidt, S. Sanna, and H. Fritze. Acoustic loss in linb1-tao3 at temperatures up to 900 °c. *physica status solidi (a)*, 222(1):2400106, 2025. https://doi.org/10.1002/pssa.202400106.

[P5] F. Bernhardt, F. A. Pfeiffer, F. Schug, S. Sanna, A. Pfannstiel, T. Hehemann, M. Imlau, and S. Ganschow. Ground- and excited-state properties of linb$_{1-x}$ta$_x$o$_3$ solid solutions. *Phys. Rev. Mater.*, 8:054403, May 2024. https://doi.org/10.1103/PhysRevMaterials.8.054403.

[P6] F. Bernhardt, L. M. Verhoff, N. A. Schäfer, A. Kapp, C. Fink, W. Al Nachwati, U. Bashir, D. Klimm, F. El Azzouzi, U. Yakhnevych, Y. Suhak, H. Schmidt, K.-D. Becker, S. Ganschow, H. Fritze, and S. Sanna. Ferroelectric to paraelectric structural transition in litao$_3$ and linbo$_3$. *Phys. Rev. Mater.*, 8:054406, May 2024. https://doi.org/10.1103/PhysRevMaterials.8.054406.

[P7] C. Kofahl, S. Ganschow, F. Bernhardt, F. El Azzouzi, S. Sanna, H. Fritze, and H. Schmidt. Li-diffusion in lithium niobate - tantalate solid solutions. *Solid State Ionics*, 409:116514, 2024. https://doi.org/10.1016/j.ssi.2024.116514.

[P8] U. Yakhnevych, F. El Azzouzi, F. Bernhardt, C. Kofahl, Y. Suhak, S. Sanna, K.-D. Becker, H. Schmidt, S. Ganschow, and H. Fritze. Oxygen partial pressure and temperature dependent electrical conductivity of lithium-niobate-tantalate solid solutions. *Solid State Ionics*, 407:116487, 2024. https://doi.org/10.1016/j.ssi.2024.116487.

[P9] U. Bashir, K. Böttcher, D. Klimm, S. Ganschow, F. Bernhardt, S. Sanna, M. Rüsing, L. M. Eng, and M. Bickermann. Solid solutions of lithium niobate and lithium tantalate: crystal growth and the ferroelectric transition. *Ferroelectrics*, 613(1):250–262, 2023. https://doi.org/10.1080/00150193.2023.2189842.

[P10] N. W. Rosemann, R. C. Döring, E. Dornsiepen, J. Belz, J. Haust, F. Bernhardt, F. Ziese, C. Attaccalite, S. Winnerl, H. Schneider, M. Helm, S. Dehnen, K. Volz, S. Sanna, and S. Chatterjee. Ultra-broadband visible and infrared light generation driven by far infrared light in the broad region from 8μm to 240μm, 2022. https://doi.org/10.48550/arXiv.2204.14043.

[P11] M. N. Pionteck, F. Bernhardt, J. Bilk, C. Dues, K. Eberheim, C. Fink, K. Holtgrewe, N. Jöckel, B. A. Muscutt, F. A. Pfeiffer, F. Ziese, and S. Sanna. Dynamical properties of the Si(553)-Au nanowire system. In W. E. Nagel, D. H. Kröner, and M. M. Resch, editors, *High Performance Computing in Science and Engineering '21*, pages 97–111, Cham, 2023. Springer International Publishing. https://link.springer.com/chapter/10.1007/978-3-031-17937-2_6.

[P12] M. N. Pionteck, F. Bernhardt, C. Dues, K. Eberheim, C. Fink, K. Holtgrewe, F. A. Pfeiffer, N. A. Schäfer, L. M. Verhoff, F. Ziese, and S. Sanna. Hyperpolarizabilities of $LiNbO_3$, $LiTaO_3$ and $KNbO_3$ calculated from First Principles. In W. E. Nagel, D. H. Kröner, and M. M. Resch, editors, *High Performance Computing in Science and Engineering '22*, pages 129–143, Cham, 2024. Springer Nature Switzerland. https://link.springer.com/chapter/10.1007/978-3-031-46870-4_10.

[P13] M. N. Pionteck, F. Bernhardt, K. Eberheim, C. Fink, F. A. Pfeiffer, N. A. Schäfer, L. M. Verhoff, F. Ziese, and S. Sanna. First principles investigation of the LiNbO3 and LiTaO3 lattice dynamics under uniaxial stress. In M. M. Resch T. Ludwig, P. Bastian, editor, *High Performance Computing in Science and Engineering '23*, Cham, 2024. Springer Cham.

[P14] M. N. Pionteck, F. Bernhardt, K. Eberheim, C. Fink, A. Kapp, F. A. Pfeiffer, N. A. Schäfer, L. M. Verhoff, F. Ziese, and S. Sanna. Effect of Mg doping on the LiNbO3 ferroelectric phase transition. In *High Performance Computing in Science and Engineering '24*, Cham, 2025. Springer International Publishing.

[P15] M.N. Pionteck, F. Bernhardt, K. Eberheim, C. Fink-Bauer, A. Kapp, M. Krenz, F. A. Pfeiffer, N. A. Schäfer, F. Ziese, and S. Sanna. Second-order nonlinear piezo-optic properties of LiNbO3 ferroelectric phase transition. In *High Performance Computing in Science and Engineering '25*, Cham, 2026. Springer International Publishing.

Danksagung

An dieser Stelle möchte ich einigen Personen, ohne deren Mithilfe und Unterstützung ich diese Arbeit nicht hätte erstellen können, meinen Dank aussprechen:
Zuerst gilt ein ganz besonderer Dank meinem Betreuer Prof. Simone Sanna: Schon während meines Bachelor- und Masterstudiums konnte ich innerhalb seiner AG die Grundlagen der Festkörpertheorie kennenlernen und mich seitdem immer weiterbilden. Dabei stand er immer aufgeschloßen und geduldig für Fragen und Rücksprachen zur Verfügung. Durch seine Offenheit und Hilfsbereitschaft wurde diese Arbeit erst ermöglicht.
Mein Dank gilt auch der gesamten Arbeitsgruppe, insbesondere Mike, Ferdinand, Kevin, Kris, Nils und Johannes, die mir mit ihren Ratschlägen und Hilfestellungen immer zur Seite standen, und auch durch viele private Unternehmungen für ein hervorragendes Arbeitsklima gesorgt haben. In diesem Zusammenhang bedanke ich mich auch bei den AGs Heiliger und Brinkmann, die immer wieder mit (außer)fachlichen Veranstaltungen den Arbeitsalltag auflockerten.
Ein großer Dank gilt auch der gesamten FOR5044 Forschungsgruppe, für die Finanzierung dieser Arbeit, für die vielen Kollaborationen, und für den wissenschaftlichen Austausch. Hier sind insbesondere Michael, Holger, Yuriy, Èva, und Umar für ihre Unterstützung beim formulieren von Papern und für Einblicke in die experimentellen Techniken zu nennen.
Diese Arbeit wäre ohne die Rechenresourcen des Hochschulrechenzentrums der JLU Gießen, des Hochschulrechenzentrums der TU Darmstadt, und des Höchstleistungsrechenzentrums Stuttgarts nicht möglich gewesen. Ein weiterer Dank geht hier an Marcel und Philipp für den vielseitigen IT-Support.
Zu guter Letzt möchte ich mich bei meinem privaten Umfeld, Freunden, Familienangehörigen und meinen Eltern dafür bedanken, dass sie mir jederzeit während meiner Promotion Unterstützung und Rückhalt gegeben haben.